School of Engineering

Optical Micro-spectroscopy Characterisation of Individual Colloidal Nanoparticles for Biomedical Applications

Furqan Alabdullah

Thesis
School of Engineering
Cardiff University

19-11-2024

Abstract

Colloidal nanoparticles are widely used in many applications, from optoelectronics devices to bioimaging, biosensing, drug delivery, sensing, and diagnostics. All these applications necessitate an understanding of the nanoparticle size and shape. However, current methods for particle characterization are either time-consuming, expensive, or not very accurate. Borri's group at Cardiff University has developed a method to overcome these limitations. The method measures the optical extinction cross-section σ_{ext} (the sum of absorption and scattering) of individual nanoparticles using wide-field transmission microscopy. It allows the simultaneous acquisition of hundreds of nanoparticles for statistical analysis. The method is straightforward, rapid, and quantitative. The precise quantification of individual particle sizes and morphologies is derived from the measurement of σ_{ext} and its relationship to the wavelength and polarisation of light.
In this thesis, we applied and further developed the method on two types of sliver nanoparticles. These are commercially available nanoparticles of nominal nanoplate shape, coated with either PVP or with a silica shell. Plates with nominal 40 nm or 70nm edge length and 10 nm thickness were investigated. Spectrally-resolved measurements were carried out in the wavelength range from 500 nm to 750 nm. A rotatable linear polariser was used to manipulate the polarisation direction of the illumination in the sample plane. This allowed us to investigate the shape of individual nanoparticles. Additionally, we utilised a high numerical aperture annular ring illumination along with a radial polariser to create a powerful polarisation component in the vertical direction. This enabled us to differentiate between thin nanoplates and thicker particles. Measurements were carried out on hundreds of individual nanoparticles, allowing for a statistically relevant analysis. In particular, we developed and applied a cluster analysis, to categorize silver nanoparticles into different groups, based on the optical cross-section and its wavelength and polarisation dependence, as predictors. For silica-coated nanoplates, we found that the substantial silica shell surrounding these particles prevents them from lying flat on a glass surface. Hence, the cluster analysis had to be modified, by introducing new predictors, effectively averaging over the particle orientation. As well as using a polarisation-averaging approach, post-acquisition, with particles deposited on a surface, Brownian rotational diffusion of sliver nanoparticles in a viscous medium was investigated, as a physical way to measure an orientation-averaged cross-section.

To validate the thickness accuracy of the technique, we collected a set of data using both optical extinction and AFM techniques. For these measurements, we used silver nanoplates coated with PVP, with a nominal edge size of 40 nm or 70 nm and a thickness of 10 nm. Finally, beyond linear optical microscopy, the application of nonlinear transient pump-probe micro-spectroscopy was explored, to investigate the thermal and mechanical interaction between individual silver nanoparticles and their surrounding environment. For these experiments, PVP-coated silver nanoplates with a nominal size of 70 nm were studied. The results indicated that there was a significant particle reshaping upon pulsed laser exposure during the pump-probe experiments, albeit a detailed interpretation of this behaviour was beyond the scope of this thesis. Overall, this work has helped advancing optical extinction micro-spectroscopy as a

powerful way to determine individual nanoparticle sizes and shapes, further boosting the utility of the method as an alternative to expensive and time-consuming electron microscopy analysis.

Acknowledgements

First and foremost, I would like to thank Allah for guidance and blessings throughout my PhD journey.

I am profoundly grateful to my supervisors for their invaluable support and advice. I extend my heartfelt thanks to Professor Paola Borri for her insightful guidance and unwavering support, which were instrumental in the completion of this work. Special thanks also go to Professor Wolfgang Langbein for his substantial contributions and valuable insights, which greatly enhanced the quality of this research. Additionally, I appreciate the general support and advice from Dr. Victoria Garcia Rocha and Professor Gao Min.

I would like to express my sincere gratitude to several individuals whose support was crucial to the success of this research. My deepest thanks go to David Regan for his dedicated training on the microscope, essential for my experimental work, and to Francesco Masia for his invaluable assistance with cluster analysis, which formed a core part of this research. Special thanks to Dr. Iestyn Pope for his support in collecting FWM data, and to Sam Hamilton for teaching me the meticulous process of sample preparation. I am also grateful to Lukas Payne for his diligent efforts in data analysis and to Vikramdeep Singh for providing comprehensive AFM training.

I am deeply thankful for the unwavering emotional support from my family. My father, my first hero, has been a constant source of strength and inspiration, while my mother's love and understanding have provided a solid foundation for my academic pursuits. My heartfelt thanks go to my sisters Yosra, Zahraa, Noor, and Anfal for their emotional support and encouragement they have provided me with.

I would also like to express my gratitude to my Fitzalan family in Cardiff Hira, Joe, Uncle Sayed, Sara, Romail, and Florence. Your constant support has been a source of strength and motivation. Additionally, I extend my heartfelt thanks to Fahad Alharbi for his exceptional support and encouragement during my PhD journey .

My sincere gratitude goes to Dr. Assad Alsahlani for his invaluable help and support.

I also thank my colleagues from the Borri group Sam, Freya, Rode, Martina,and Nicole for making this journey an incredibly memorable experience.

Lastly, I extend my deepest gratitude to my beloved fiancé Harith Your patience, continuous support, and unwavering encouragement have been my rock throughout this journey. Thank you for being my dependable shoulder and an amazing partner.

Contents

List of Figures

List of Tables

Publications

The publications that have been produced in conjunction with the work presented here are as follows:

- Alabdullah, F., Singh, V., Payne, L., Regan, D., Masia, F., Rocha, V.G., Langbein, W. and Borri, P., 2024. Radially polarized light in single particle optical extinction microscopy identifies silver nanoplates. Applied Physics Letters, 124(18).
- F. Alabdullah, D. Regan, L. Payne, V. G. Rocha, W. Langbein, and P. Borri, 'Quantitative size and shape analysis of individual silver nanoplates by high throughput widefield extinction microscopy', Oral Presentation, Photon, Nottingham University, UK, 2022.

Work is in progress on preparing the following papers:

- Orientation-Independent Classification of Silver Nanoparticles via Rotational Averaging and Optical Extinction Microscopy.
- Morphometric analysis of gold nanospheres by optical extinction micro-spectroscopy using linear and radially polarised illumination.
- Correlative Analysis of Nanoparticle Mechanical Properties Using Transient Resonant Four-Wave Mixing Microscopy and Optical Extinction Measurements.

Chapter 1

Introduction

Nanoparticles are a growing area of research, boosted by the demand of developing innovative tools and technologies in many fields, from engineering, chemistry and physics to biology and medicine. Continuous effort is devoted to improving and optimising nanoparticle performances, by tailoring their size, shape, chemical/material composition, and surface properties. Nanoparticles have several advantages over bulk structures. They have a large surface-to-volume ratio, exhibit tuneable size-dependent optical properties [1][2][3], can be engineered to be bio-compatible, and in turn hold huge potential for targeted therapeutics as gene and drug delivery vehicles [2][3][4]. Notably, the application of nanoparticles in biomedicine requires the development of imaging technologies able to locate these nanoparticles inside cells and tissues. Fluorescence-based approaches are often used in optical bioimaging. The specificity of fluorescence labelling facilitates the imaging and assessment of cellular and molecular functions. Notably, some advanced fluorescence methods have shown the capability to resolve nanoscale features by surpassing the diffraction limit of light, hence achieving super-resolution below this limit (typically restricted to around 200 nm). However, fluorescent labels can undergo photobleaching, limiting the observation time window, and resulting in undesirable chemical effects that can lead to cytotoxicity. Therefore, it is crucial to develop imaging techniques that can identify individual non-fluorescent nanoparticles, not limited by photobleaching, with high spatial resolution under conditions of live-cell imaging [5]. Therefore, it is crucial to develop imaging techniques that can identify individual non-fluorescent nanoparticles, not limited by photobleaching, with high spatial resolution under conditions of live-cell imaging. Several optical methods for imaging individual non-fluorescent nanoparticles exist, however suffer from limited specificity and sensitivity. For example, Differential Interference Contrast (DIC) microscopy is capable of generating high-quality images for transparent specimens, hence rendering it highly advantageous for the observation of living cells and subcellular structures. However, DIC lacks chemical specificity [6][7]. Beyond, simple linear optical microscopy methods, multi-photon microscopy has also attracted increasing interest. In that context, four-wave mixing (FWM) imaging of metallic nanoparticles has recently emerged as a powerful photostable background-free technique compatible with live cell imaging [8]. Beside bioimaging, it is important to develop methods that can accurately quantify the size and shape of nanoparticles. Optical extinction microscopy is a reliable, precise and fast technique to characterise the size and shape of individual nanoparticles by measuring their optical cross-section at several wavelengths, implementing polarisation-resolved measurements [9][10]. Other state-of-the-art methods employed for the investigation of nanoparticle morphologies include Analytical Ultracentrifugation (AUC) and Differential Centrifugal Sedimentation (DCS). They use centrifugation to separate particles, offering data on sizes, shapes, and molecular weight [11]. Dynamic Light Scattering (DLS) is a technique which measures the scattering of light in a solution containing particles as a function of time. The variation of the

scattering signal due to the Brownian motion of the particles is analysed to derive particle sizes (also called hydrodynamic radii) the sub-micrometre scale [12]. Nanoparticle Tracking Analysis (NTA) is a similar technique that implements light scattering and Brownian motion in order to quantify and examine the size distribution of individual particles in a liquid suspension. The main advantage of NTA is its sensitivity to individual particles, as opposed to ensemble measurements in DLS [13]. Tunable Resistive Pulse Sensing (TRPS) involves sensing the change in the electrical resistance caused by the motion of suspended particles in an electrolyte solution. Particles are directed through a single pore of a membrane which will induce a change in the electrical resistance of that pore, detected and quantified. TRPS is capable of determining the size, charge and concentration of particles by analysing the variations in resistance. This approach is flexible, where the pore size can be modified to conciliate different particle sizes [14]. The implementation of Transmission Electron Microscopy (TEM) and Scanning Electron Microscopy (SEM), complementary to optical microscopy, has played an essential role in the visualization of nanoparticles since the mid-20th century. High-resolution imaging of nanoparticles is enabled by the wavelength of electron beams, much shorter than the wavelength of light. This technology has made it possible to show detailed images in both two- and three-dimensional formats, and to study the shape, size, and surface morphologies of nanoparticles. TEM and SEM have been applied to many materials for a wide range of applications [15][16][17]. In depth discussion of those techniques will be presented in sections 1.5.1.2 and 1.5.3. Differing from optical and electron microscopy, Atomic Force Microscopy (AFM) is a technique that offers vertical/topographic nanoscale resolution. In turn, AFM can produce detailed topographical maps of sample surfaces that reveal useful information about particle size, surface roughness, and structural features [18]. In the following sections, I will discuss specifically the role of silver nanoparticles for biomedical applications. I will also review the state of the art regarding nanoparticle size/shape characterisation analysis, leading to the motivation of the work carried out in this thesis.

1.1 Optical and Plasmonic Properties of Metal Nanoparticles

The interaction of light with a nanoparticle depends on the size, shape, and composition of the nanoparticle, as well as the composition of the surrounding medium. Two main linear optical properties are defined: absorption (conversion of the incident exciting light into another energy form, e.g., heat) and scattering (radiation generated by electrons set in motion by the impinging light field). The coupling strength of light with the nanoparticle for each optical process is quantitatively described by an optical cross-section (σ), defined as the power P removed from an incident plane wave through a given optical process, normalized to the incident intensity I_i, i.e., $\sigma = \frac{P}{I_i}$. The cross-section has the unit of an area. The absorption cross-section σ_{abs} and scattering cross-section σ_{sca} define a resulting total extinction cross-section $\sigma_{\text{ext}} = \sigma_{\text{abs}} + \sigma_{\text{sca}}$ [19]. Exact mathematical formula of these cross-sections exist for a nanoparticle of spherical shape in a homogeneous medium (Mie theory). The case of metal nanoparticles, such as gold and silver, results in absorption and scattering spectra as a function of the wavelength (or frequency) of the incident light which exhibit a maximum at the so-called localised surface plasmon resonance (LSPR). The physical origin of this resonance is related to the coherent oscillation of the free electrons in the metal, in response to the incident light wave, with a restoring force due to the electric field created by the corresponding charge displacement. This electric field depends on the particle morphology, hence the LSPR frequency is a function of the shape and size of the nanoparticle [20]. For example, spherical silver nanoparticles with diameters much smaller than the incident light wavelength (Rayleigh limit) have a LSPR at around 420nm in water, which red-shifts with increasing refractive index of the surrounding medium. Going from spherical to ellipsoidal rod-like shape further results in a red-shift of

the LSPR, depending on the rod aspect ratio [21]. Many nanoparticles practically utilised are fabricated via colloidal chemistry [22]. An important aspect in this fabrication method is the choice of capping molecules to ensure colloidal stability. Capping molecules adsorb to the nanoparticle surface, preventing aggregation by providing electrostatic or steric stabilization. For instance, citrate ions are commonly used to cap silver nanoparticles, ensuring stability through a combination of electrostatic and steric repulsion [23]. Electrostatic stabilization creates a charged layer that repels other particles [24], while steric stabilization involves the formation of a physical barrier by organic molecules or polymers. These capping agents not only stabilize the nanoparticles but also facilitate functionalization, allowing for targeted applications in e.g. drug delivery or enhanced biocompatibility for tissue engineering additional examples for silver nano particles capping are explained in Chapter 2. Overall, the combination of size and shape control, along with appropriate surface capping, enables colloidal metal nanoparticles to be highly adaptable for a variety of biomedical uses.

1.2 Silver nanoparticles (AgNPs) and their biomedical application

Silver nanoparticles (AgNPs) have gained significant attention from the industrial sector and the scientific community due to their numerous applications, ranging from energy storage to biomedical devices and consumer goods like paints. In biomedicine, AgNPs have been recognised due to their efficiency against microorganisms such as bacteria and *fungi*, their anti-inflammatory properties, and their capability to improve wound healing. In fact, AgNPs can inhibit microbial growth and prevent illness caused by these microorganisms [25]. A number of novel methodologies have been designed to fabricate AgNPs with control over their dimensions and structural properties [26]. AgNPs show noticeable characteristics like high thermal and electrical conductivity, catalytic activity, surface-enhanced Raman scattering, and nonlinear optical behaviour [27]. Extensive utilization of AgNPs is seen in many commercial goods as a result of their established antibacterial capabilities. Examples of those products include plastics, soaps food packaging, pastes, textiles and food items. Indeed, the market value of AgNPs has grown significantly [28]. AgNPs are applied in multiple forms, including colloidal/liquid forms (e.g. coatings, enamel and paints, shampoos) and solid forms (e.g., mixing AgNPs with polymer scaffolds). They are also found in materials such as nonwoven fabrics [28]. The significance of AgNPs in the textile sector should not be overlooked, since they are employed in the fabrication of water filtration membranes. The incorporation of AgNPs into water filtration membranes is motivated by their antibacterial characteristics and the controlled release kinetics of AgNPs from the membrane [28][29]. Notably, in recent years, there has been a significant focus on the investigation of AgNPs, for a wide range of biological/biomedical applications [30]. Despite the scarcity of available data on their toxicity and in vivo biological behaviour, these nanostructures have been extensively employed as antibacterial agents in healthcare. For example, AgNPs provide significant benefits for cancer therapies, since they have been shown to enhance the effectiveness of chemotherapy while minimising systemic toxicity [31]. AgNPs have been effectively implemented as drug-delivery systems for the purpose of combating tumours [32]. They can perform as either active [33] or passive [34] nanocarriers to deliver anticancer medications. Recent studies have shown the possible utilisation of AgNPs as carriers for drugs and vaccines with the ability of targeting specific cells and tissues [35]. The unique optical characteristics of AgNPs [36][37][38], together with the recent progress in their biocompatibility and stability by surface modification, , further support the application of silver nanoparticles as promising systems for drug delivery applications [39].

1.2.1 Antimicrobial agents using silver nanoparticles

During the past few years, research related to the manufacture of silver nanoparticles by using microorganisms and plant extracts has drawn significant attention. This is due to the accessibility, adaptability, non-toxic nature, and most importantly, biodegradability, sustainability, and cost-effectiveness associated with this approach. Metal nanoparticles are now being synthesised using a diverse range of plant species with notable efficacy. A diverse range of botanical components, such as leaves, fruit peels, flowers, barks, and roots, are utilised in the process of synthesising AgNPs and other metallic nanoparticles [40]. Antibacterials and disinfectants might be delivered to the human cells by using AgNPs for the delivery process. Numerous types of bacteria are directly affected by the toxicity of silver ions (Ag+) and their corresponding combinations. Plant species offer useful characteristics which enable the synthesis of metallic nanoparticles with antimicrobial abilities [41]. They hold bioactive substances like phytochemicals and enzymes, that are capable of decreasing metal ions and stabilize nanoparticles. The utilization of plant-based synthesis offers an environmentally friendly, cost-effective and scalable method for manufacturing metallic nanoparticles, making it a strategy that is highly attractive to manufacturers [40]. Throughout history, silver has been used in several traditional practices, including medical and culinary ones. As stated, silver is known for its bactericidal (eliminating) and bacteriostatic (inhibiting growth) properties, mainly due to silver ions which can kill living organisms such as bacteria and $fungi$. Ionic silver has a strong interaction with thiol groups contained in essential bacterial enzymes, causing their inactivation. Hence, these enzymes no longer have the capacity to copy DNA [42]. Silver mixtures such as silver sulphadiazine and silver nitrate are used in the treatment of burns (to ban bacterial proliferation) and in the sterilisation of drinking water. AgNPs have been widely implemented as antibacterial agents for a long time. Within the pressing challenge of antimicrobial resistance, the application of AgNPs to eliminate many types of bacteria that resist antibiotics is especially appealing. It has been shown that AgNPs destabilise membrane potential and reduce intracellular ATP levels, both of which lead to the death of bacteria. The use of AgNPs in plant protection has also increased due to the rise in fungal diseases and their development of resistance mechanisms, which reduce agricultural production. AgNPs' anti-fungal activity has been assessed against a variety of plant infections as well as human illnesses, such as $Candidaalbicans$ and $Aspergillusochraceus$. $Macrophominaphaseolina$, $Fusariumoxysporum$, $Trichoderma$, and $Alternariaalternate$ are among the commercially significant fungal pathogens against which the fungicidal properties of AgNPs have been tested [43], as are $Raffaelea$, $Alternariabrassicicola$, $Botrytiscinerea$, $Cladosporiumcucumerinum$, $Fusarium-solani$, $Corynesporacassiicola$, $Cylindrocarpondestructans$, $Didymellabryoniae$, $Glomeirellacin-gulata$, $Stemphyliumlycopersici$, $Monosporascuscannonballus$, $Pythiuma-phanidermatum$, and $Pythiumspinosum$ [44].

1.2.2 Anticancer

Cancer cells exhibit aberrant metabolic patterns and genetic expressions, resulting in a range of pathogenic and metabolic changes within the cellular microenvironment. These modifications are induced by mechanisms such as cell signalling, fast cell division, angiogenesis, and metastasis. Numerous studies have documented that the use of AgNPs effectively augments the chemotherapeutic effectiveness against cancer cells that exhibit multidrug resistance. The cytotoxicity of AgNPs synthesised utilising diverse plant extracts shows significant potential, resulting in reduced cell survival across a range of cancer cell types. In addition, it has been shown that nanoparticles ranging in size from 5 to 35 nm have a significant ability to trigger cell death by specifically targeting the structure of mitochondria [45].

1.2.3 The use of AgNPs in drug-delivery systems

Silver nanoparticles have been discovered to possess antibacterial properties, as previously mentioned [46]. The combined antibacterial effects of a medication and ligand-dependent silver release have the potential to be quite effective. To that end, in order to efficiently manufacture nanoparticles for commercial use in the treatment of infectious disorders, it is imperative to optimise the surface ligands, including coordination atoms, carbon chain lengths, and terminal groups [47].

1.2.4 The use of AgNPs in the modification of catheters

In general, microorganisms cling to the surfaces of catheters and proliferate fast, resulting in the formation of biofilms under such environmental circumstances. These biofilms might contribute to the development of bloodstream infections, exacerbating the situation. Silver-impregnated catheters have been successfully employed in many medical applications, while AgNPs have found application in a range of biomedical devices [48]. Various techniques, including casting with solvent, electrospinning, electrospraying, and silver iontophoretic technology, have been employed in the manufacture of catheters impregnated with silver. The efficiency and longevity of medical devices are contingent upon the characteristics of AgNPs and the integration of a coating.

1.2.5 Dental applications for silver nanoparticles

In addition to various dental specialties like implantology, restorative dentistry, and dental prosthesis, AgNPs have been used in the field of endodontics. AgNPs are primarily used in dentistry to improve and maintain oral health by efficiently reducing or preventing microbial growth on dental materials. Penetrating cell membranes is one of the many features that AgNPs have. This increases antibacterial action, specifically against biofilm-forming microorganisms. The integration of dental materials with AgNPs can be achieved throughout many processes, that are dependent upon the particular type of materials utilised. In the context of dental implants, titanium samples undergo immersion in a solution of silver nitrate, followed by exposure to ultraviolet (UV) light after undergoing a washing and drying process [49]. In order to enhance the solubility of silver in adhesive/resin composites, it is recommended to use a monomer, namely 2-tert-butylamino-ethyl-methacrylate [50]. Numerous investigations are now being conducted with the aim of enhancing the quality and durability of polymeric restorative materials. Repair composite materials tend to acquire a great amount of biofilms. The presence of an inadequate seal between the restorative composite material and the cavity wall might facilitate the colonisation of oral microorganisms, which subsequently contributes to the development of secondary caries and necessitates the need for replacements. In order to mitigate these complexities, it is imperative to include restorative elements that possess antibacterial properties.

1.2.6 Silver nanoparticles for wound healing

The occurrence of a wound is characterised by the disturbance of the skin's integrity, and may be categorised into three types: acute wounds such as burns, chronic wounds like diabetic foot ulcers, and pressure ulcers [51]. In light of the emergence of antibiotic resistance and the occurrence of infectious illness outbreaks, researchers are actively seeking more effective alternatives. There has been a noticeable increase in the level of interest surrounding the use of AgNPs incorporated into biopolymers for the purpose of wound healing applications. Sim et al. conducted research on patented silver-based goods and found that a total of 5000 new applications were formally submitted between 2007 and 2017 [52]. Silver-based solutions have been developed and

commercialised because of their enhanced designs and effectiveness compared to conventional dressing materials. The antibacterial properties of silver have been found to effectively mitigate the development of resistance in microorganisms, hence enhancing its efficacy against multi-drug-resistant strains. AgNPs are actively participating in wound healing mechanisms, along with their ability to prevent infections, enhance wound contraction, facilitate accelerated rates of healing, and stimulate proliferation and migration of keratinocytes [53]. Antimicrobial treatment plays a pivotal role in the management of wound and skin care by supervising processes such as colonisation, multidrug resistance, and pathogen growth. In terms of biocompatibility, there is a demand for a thorough investigation into the interaction mechanism between AgNPs and microbial flora, together with clinical toxicity studies. Medical items, such as, plasters, lotions, textile materials, ointments, gauzes, sutures, and bandages, have a promising potential for for improving their wound healing properties when enriched with AgNPs. The amalgamation of silver with the silk protein sericin has been inspected to have a synergistic effect, which would lead to enhanced tissue regeneration along with antibacterial capabilities. This natural wound dressing biomaterial has been authorised for use [54].

1.2.7 Silver nanoparticles for bone healing

The skeletal structure of humans is mostly comprised of hydroxyapatite, a crystallised compound consisting of calcium and phosphate. This substance is generally acknowledged and utilised as a body implant material. Biocompatible hydroxyapatite, mixed with either metallic or ionic silver forms, is a good option for the production of antimicrobial and bioactive bone implants, to be used as superficial implant materials. Hydroxyapatite coatings that incorporate AgNPs are indeed effective inhibitors of both Gram-positive and Gram-negative bacteria [55]. Silver nanoparticles are considered promising candidates for improving bone healing due to their antimicrobial qualities and capability to boost bone regeneration. AgNPs can also address infections at the injury site, a crucial element for achieving bone regeneration. Moreover, research has been carried out on the potential of silver nanoparticles to revive osteogenesis and to increase the growth of bone forming cells [56].

1.2.8 Silver nanoparticles' toxicity

Many in *in vitro* and *in vivo* experiments have been carried out on AgNPs in order to clarify their potential toxicity against tissues and organisms. The interaction among blood, tissues, and AgNPs has gained significant attention because of its' implications for biosafety. Given the specific physical and chemical features shown by AgNPs, it is plausible that they also elicit unique toxicity pathways. Therefore, it is imperative to develop a comprehensive understanding of the safety aspects associated with AgNPs to facilitate their increased utilisation in clinical applications [57]. Scientific research has clarified that nanosilver has the ability to stimulate the generation and subsequent buildup of Reactive Oxygen Species (ROS) inside cells, as well as change the permeability of mitochondrial membranes, which will cause damage to DNA. Various scientific studies have shown that a reduction in cell viability can take place because of the exposure to AgNPs. One reason is related to the upregulation of genes associated with apoptosis and the initiation of the apoptosis pathway [58].

1.3 The Impact of Shape and Size of Silver Nanoparticles on Cytotoxicity

Many researchers have suggested a correlation between the particle size and the biological/biomedical properties of AgNPs [59] [60]. Powers *et al* [61] reported on the characteristics of polyvinylpyrrolidone (PVP)-capped AgNPs that are size-dependent. In recent investigations, researchers have suggested that there is a connection between increased cytotoxicity and reduced size. This can be attributed to the fact that small AgNPs show increased dissolution and release of AgNPs ions, eased up by their larger surface area [61]. However, other studies have emphasised the mass-based characteristic of AgNPs, neglecting to account for their particle size and surface area. Additionally, there have been suggestions linking dissolution and stability of AgNPs with their surface modification [59] [60]. Coating and capping agents can influence the dimensions, morphology, and interfacial characteristics of AgNPs. Overall, researchers have emphasised that the dimensions, morphology, and surface characteristics of AgNPs play a role in determining their cytotoxic effects. AshaRani *et al.* (2009) conducted a study which revealed that human lung and skin cells were more severely affected by smaller silver nanoparticles (10 nm) in comparison to larger nanoparticles (75 and 100 nm) [62]. The shape of AgNPs can also influence their cytotoxicity. For example, compared to spherical nanoparticles, silver nanowires and nanorods may exhibit different toxicity profiles. A study conducted by Kim *et al* (2013) showed that silver nanowires were more cytotoxic as compared to silver nanosphers [63]. The presence of a surface coating on silver nanoparticles can alter their interaction with cells. The cytotoxicity can be influenced by coating such as citrate or PVP. Foldbjerg *et al.* (2009) conducted a study which revealed that the toxicological effects of silver nanoparticles were controlled by their surface coating, in a manner specific to the cell type under investigation [17]. In summary, the toxicity of silver nanoparticles is closely linked to interconnected factors, including nanoparticle size, surface capping, colloidal stability, and the release of silver ions. As mentioned, smaller nanoparticles, due to their increased surface-to-volume ratio, tend to dissolve more readily, leading to a higher release of silver ions, which are considered a major contributor to cytotoxicity. The nature of the capping agent plays a significant role in stabilizing nanoparticles, preventing aggregation, and influencing their biological interactions. For instance, polyvinylpyrrolidone (PVP) and citrate coatings are frequently used to stabilize silver nanoparticles in colloidal form, which directly impacts their dissolution rate and ion release. Moreover, surface capping can also alter the affinity of AgNPs for cellular membranes, thereby influencing cellular uptake and the extent of induced oxidative stress. Therefore, understanding the role of surface capping not only aids in predicting colloidal stability but also helps in tuning the dissolution and toxicological profiles of AgNPs, making it a key factor in the design of nanoparticles for biomedical application. More information and examples of the Ag NPs capping were explained in Chapter 2, 2.1.2.

1.4 Gold nanoparticles (AuNPs) and their biomedical application

Gold and silver nanoparticles have unique optical properties, related to their plasmonic behaviour, which is dependent on their shape and size. These characteristics are important in a wide range of applications, including sensing, catalysis, and biological imaging. Specifically, these nanoparticles absorb and scatter light at the so-called Localised Surface Plasmon Resonance (LSPR). This resonance manifests in a particular wavelength range, which depends on the shape, size, and environment of the nanoparticles [64]. For example, gold nanorods with a suitable aspect ratio have strong absorption and scattering properties in the near-infrared spectrum.

Notably, gold nanoparticles allow efficient conversion of the absorbed light into thermal energy, and have been widely utilised in photo-thermal therapy, where they can selectively eliminate cancer cells [65]. As compared to silver nanoparticles, gold nanoparticles are more chemically stable and biocompatible. They have been utilised for targeted drug delivery to tissues or cells, thereby enhancing the efficiency of treatment [66]. Owing to their combination of properties, gold nanoparticles have been implemented as "theranostics" agents, merging diagnosing and treatment [67]. This integration enables the real-time monitoring of the treatment response [68]. The subject of gold nanoparticles in healthcare and medical devices is under an ongoing evolution, with researchers actively investigating novel applications and uses.

1.5 Morphometric characterisation techniques

In order to optimize the effectiveness of silver and gold nanoparticles for a wide range of applications, it is necessary to measure and control their shape and size characteristics. The text below gives a brief overview of the methodologies available for these measurement.

1.5.1 Electron microscopy

Electron microscopy is an imaging methodology that uses electron beams, as opposed to light, to reach nanoscale resolution. The contrast in electron microscopy (EM) arises from differences in the interaction of electrons with various materials. Heavier elements have more electrons hence produce more electron scattering and less transmission, leading to higher/stronger contrast in the images [69]. There are two primary categories of electron microscopy, namely TEM and SEM, each possessing distinct capabilities.

1.5.1.1 Transmission Electron Microscopy (TEM)

The TEM general working principle is based on directing a high-energy electron beam through a thin sample. The change in the electron beam upon transmission through the sample is used to generate an image contrast [70]. TEM has a nanoscale spatial resolution, due to the short wavelength of an electron beam compared to light. TEM enables the analysis of particle size, crystalline structure, and morphology. It is however time-consuming, expensive, and requires experienced technical support. Moreover, samples must be prepared in thin sections and imaged under vacuum conditions [71]. TEM has a key role in material science, specifically for investigating atomic-scale features like crystalline formations, compositional analysis, and defects [71] [70].

1.5.1.2 Scanning Electron Microscopy (SEM)

The utilization of SEM has effectively changed the industry in regards to the scope of nanoscale characterization [72]. SEM technology was introduced by Dr. Max Knol and Dr. Ernst Ruska in the 1930s, and since then, it has stood out as a pivotal instrument in several scientific fields. SEM in its' early stages was dominantly utilized surface imaging. Progression in this technology contributed to expanding its' scope, allowing the examination of elemental composition alongside high-resolution images of nanostructures [73][72]. SEM is utilized in many fields including materials science, geology, and biology. Samples undergoing SEM analysis are subjected to a focused electron beam, resulting in the production of different signals, depending on the interactions between the sample and the electrons [73][72]. In order to generate an image, the focused beam is raster scanned, and signals are captured by detectors. The essential elements of SEM are an electron gun, lenses used to focus the electron beam, a scanning mechanism, which is

responsible for moving the beam over the sample, and detectors, which are utilised for data acquisition. The collection of high-quality SEM images is dependent on the sample preparation and their nature. Typically, the sample preparation for SEM imaging entails dehydration and applying a conductive coating. Additionally, this technique provides a range of methods for imaging, including secondary electron imaging (SEI) for the examination of surface morphology, backscattered electron imaging (BEI) for the study of compositional information, and X-ray microanalysis for the identification of elemental constituents.

1.5.2 Differential Interference Contrast Microscopy (DIC)

The DIC technique, also known as Nomarski microscopy, was initially introduced by George Nomarski during the 1950s. This technique was regarded as an important progression in optical microscopy to examine objects that are nearly transparent. DIC microscopy implements polarized light interference to increase contrast under brightfield microscopy illumination. This approach is beneficial for the examination of live unstained biological samples [74]. The working principle of DIC microscopy is based on detecting the optical path length difference among adjacent regions of the specimen and, in turn, converting optical phases into intensities, through interference, which result in an image contrast. DIC implements a process of dividing a polarized beam of light into two orthogonal components, which are spatially split and interact with the specimen, before being recombined. This technique produces contrast by utilizing small variations in both the thickness of the specimen and the refractive index (namely, the optical path length). Polarised light is a key component in DIC microscopy. A polariser and an analyser are employed in order to create and examine light waves. The modulation of polarisation is a crucial factor in the generation of image contrast. DIC microscopy generates an image that shows a relief-like optical appearance as a result of the differential phase change caused by the material. As mentioned, DIC is a powerful instrument for examining transparent and semi-transparent samples [75]. A typical DIC microscope consists of a light source, a condenser lens, a polariser combined with waveplate, Wollaston and/or Nomarski prisms, an objective lens, an analyser, and a camera, see Fig. 1.1. To produce contrast, the optical elements are carefully positioned, and the correct alignment of the optical configuration is key for its operation. Proper component alignment and calibration transform specimen phase gradients into visual contrast in the final image. DIC microscopy can operate with several light sources including halogen lamps, mercury arc lamps, or LEDs. The light source is decided based on the sample and experimental needs [76]. As stated before, DIC microscopy may allow observing specimens in their natural, intact form, without labelling or staining. Quantitative phase imaging using DIC microscopy can determine specimen refractive index and/or thickness changes, offering useful information in cell biology and biophysics [75][76]. As any other technique, DIC microscopy has also its own limitations. For example, the DIC spatial resolution is limited by the diffraction of light (a few hundred nanometers). DIC operates well on thin, semi-transparent specimens and has been used to determine the size of individual dielectric nanoparticles [77]. High-quality DIC microscopes are expensive, and require calibration and maintenance [74].

1.5.3 Atomic Force Microscopy (AFM)

Atomic Force Microscopy (AFM) is mainly utilized for imaging and analyzing surfaces at the nanoscale. During the second half of the 20th century, significant developments of this technology took place. The AFM works by quantifying the interactions that occur between the surface of a material and a tip-like probe, thereby providing detailed topographic pictures. Several scientific disciplines have been extensively utilizing this technique, including biology, nanotechnology, and materials science [78]. AFM is implemented for the purpose of inspecting the mechanical char-

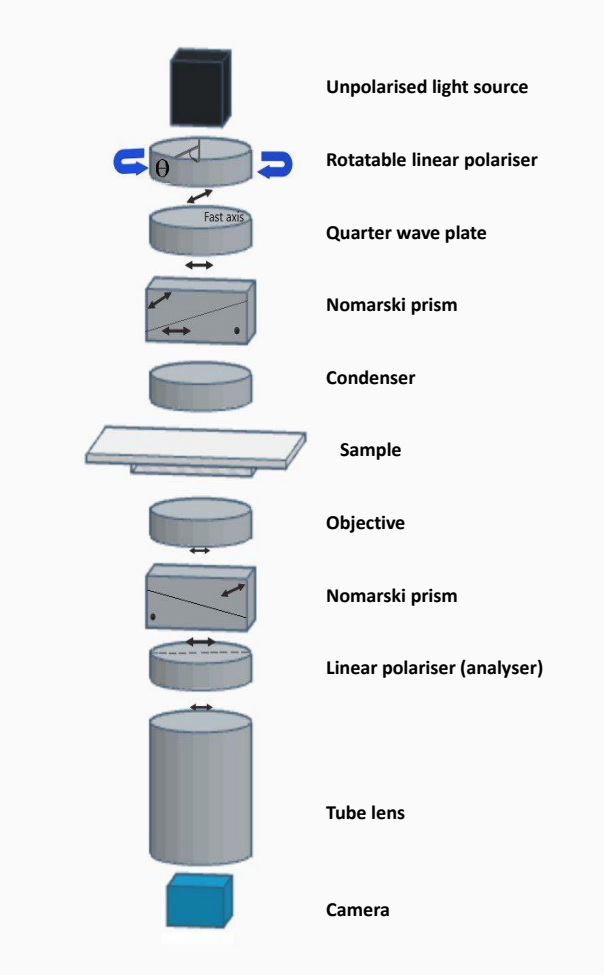

Figure 1.1: DIC set up component. Diagram illustrating the main optical components of a microscope setup employed for capturing DIC images. The set-up consists of a light source, a rotatable linear polariser, followed by a quarter-wave plate, Nomarski prisms, a condenser lens, an objective lens, a tube lens, an analyser, and a camera.

acteristics of surfaces and materials, including roughness, friction, stiffness, and adhesion, at the nanoscale. The examination of DNA and proteins as cellular components is an important application example of the AFM technique. AFM plays a crucial role in the field of nanotechnology, specifically in the analysis of nanostructures and nanomaterials. This technique is important in microelectronics and optoelectronics, as it enables the evaluation of homogeneity, thickness, and surface quality of thin films and semiconductor wafers [79]. AFM operates by using a scanning mechanism where a slender and pliable probe tip is moving over the samples' surface. Several forces, including van der Waals, electrostatic, and chemical interactions, become significant, resulting in the deflection or bending of the cantilever as the tip approaches the surface. The incidence of a laser beam provides the reference for the positioning of the cantilever, and the deflection of the laser beam is quantified by a photodetector that is position-sensitive [79] [80]. It is important to consider the limitations of AFM, such as the relatively slow imaging speed when investigating dynamic processes. The complexity during the sample preparation process

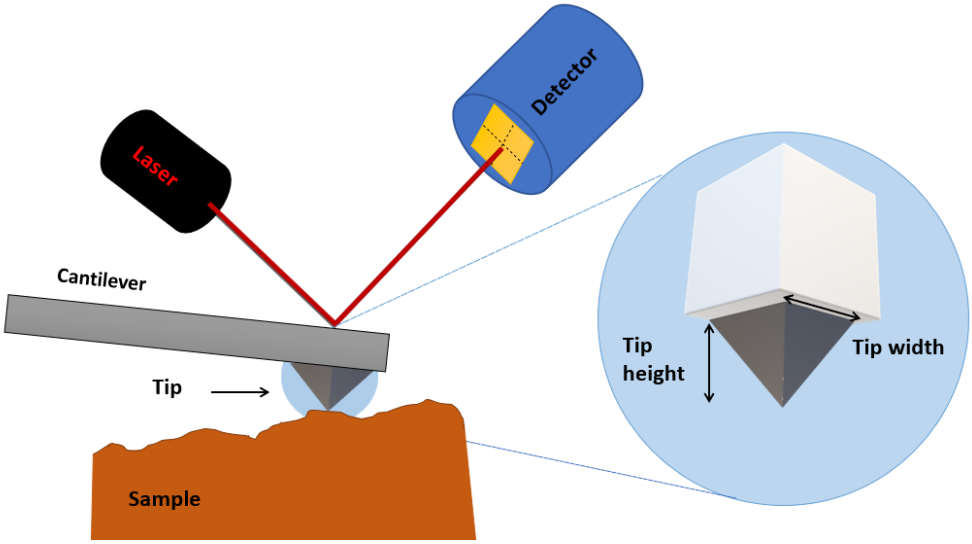

Figure 1.2: Key components of an AFM setup. The tip engages with the probed sample, and the cantilever undergoes bending due to attraction or repulsive forces. The process of bending is observed by directing a laser beam onto the gold-coated underside of the cantilever and determining the displacement of the reflected light through the use of a photodiode.

is another challenge. Moreover, the high cost of the equipment might restrict accessibility/use for simple research studies. The need for highly skilled personnel is another challenge to be considered [81].

1.5.4 Centrifugation

Centrifugation methods are implemented to assess the size distribution of particles by analysing particle settlement rates. These approaches allow the separation of particle sizes, when having samples that display a range of sizes. In certain cases, a resolution as fine as 1 nm can be achieved with the centrifugation technique. However, centrifugation methods cannot provide shape information, use particle ensembles, and rely on assumptions regarding particle density [9]. Differential centrifugal sedimentation (DCS) [82] and analytical ultracentrifugation (AUC) [83] are established centrifugation methods. DCS instruments use particles that undergo sedimentation within a transparent disc, causing the formation of a density gradient that is optically clear. A well-known configuration of DCS instruments encompasses a hollow center transparent disc, propelled by an adjustable speed motor. Fig. 1.3 shows a standard cross-sectional view of the disc. A monochromatic light beam with a wavelength of 400 nm to 500 nm is used. This range of wavelength optimizes the sensitivity of the detector while measuring particles smaller than 100 nm, see Fig. 1.3, adapted from reference [84].

AUC measurements include the process of sedimentation within a transparent sapphire cell or quartz which is leading to concentration profile information . This profile is then analyzed to determine the distributions of sedimentation coefficients. The analysis of sedimentation profiles follows a systematic approach, starting with data acquisition of sedimentation velocity through ultracentrifugation experiments. By identifying different particles and considering factors such as particle aggregation or sample heterogeneity, a thorough analysis and understanding of particle dynamics are carried out [85]. Both the DCS and AUC methods are based on the sedimentation process, but they differ in their ranges of rotation speeds, resulting in different detectable

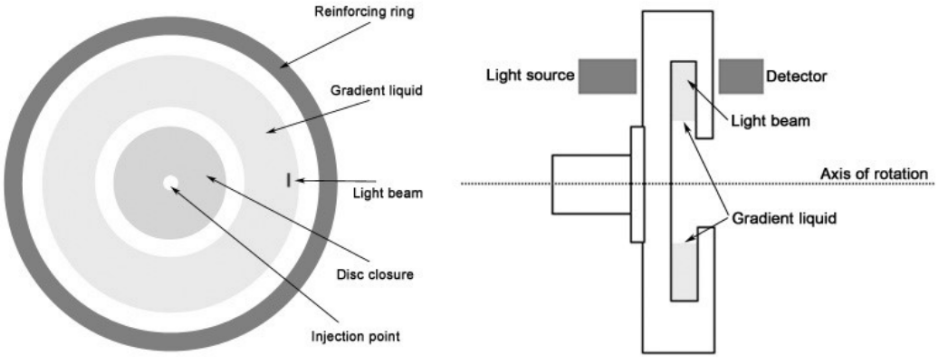

Figure 1.3: Design of DCS particle size analyser. A schematic representation of the primary components of the DCS that are utilised for the particle size analyser. Figure adapted from reference [84].

sizes.The maximum speed of DCS is comparatively reduced, hence imposing a limit on the size of smaller particles to a minimum of 5 nm . With high centrifugal forces ($> 100,000$g), AUC can analyse proteins, polymers, tiny compounds, and nanoparticles with a resolution of 1 nm or less. Big items may settle too rapidly for AUC analysis however, larger entities may settle too quickly for AUC analysis. Conversely, DCS can detect particles up to $10\,\mu$m, making it a useful tool for measuring large aggregates. In theory, both AUC and DCS techniques have the potential to accurately determine the particle size distribution of highly polydispersed samples within their respective operational boundaries [85]. However, it can be challenging to effectively separate extremely tiny and large particles simultaneously by selecting a set rotating speed. In recent studies, it has been demonstrated that the utilisation of a rotating ramp consisting of several speed increases in AUC tests may effectively address this issue. This approach enables the high resolution analysis of highly polydispersed samples, namely it provides a wider sedimentation coefficient range , improving particle size detection. [86]. A primary limitation associated with centrifugal sizing procedures is the requirement that the particles' density, must be both consistent and uniform over the whole population, in order to accurately determine the particle size distribution based on the observed sedimentation coefficient. The capacity to accurately determine the size of aggregates (or agglomerates) using AUC and DCS techniques may be constrained due to challenges in selecting and measuring their density, which can differ from the density of individual particles. Measuring alterations in size resulting from interactions between nanoparticles and proteins brings challenges due to fluctuations in the density of the NP-protein complex. In such situations, the integration of DCS measurements with precise size measurements, such as those obtained using dynamic light scattering, provides valuable insights into both the dimensions of the complex and the protein layer's thickness [87]. Sophisticated AUC equipment is outfitted with refractive index (RI) and/or absorbance detectors, enabling the examination of other key parameters for nanoparticle-encapsulated drug delivery systems, including drug loading [88][89]. In nanomedicine formulations, the molecular weight of the active pharmaceutical ingredient (API) is often significantly smaller than that of the nanoparticle carrier. In this particular scenario, the rate of sedimentation for the nanoparticles is significantly higher compared to the unbound API. In cases where the unbound API exhibits a distinct UV-Vis absorption profile, it is possible to achieve a time-independent and radius-independent absorbance background at the conclusion of the analysis by selecting a centrifugal force that leads to the sedimentation of the nanoparticle while leaving the unbound API unaffected. The

latter signal is indicative of the unbound API proportion present in the sample. The estimation of absorbance at the start of the study, along with the remaining absorbance linked to the unbound active pharmaceutical ingredient, allows for the estimation of both the unbound API fraction and the fraction of API bound to the non-specific esterase protease (NEP) in a single straightforward procedure [88][89].

1.5.5 Dynamic Light Scattering (DLS)

Dynamic Light Scattering (DLS) is an analytical method widely used across scientific fields to investigate the size, variation, and motion of particles in colloidal systems. DLS is a laser-based method used to study the movement of particles in a liquid without causing any damage. Valuable information regarding particle size, distribution, and dynamics can be gleaned by analysing the fluctuations in scattered light [89] [88] [90] [91] resulting from the Brownian motion of particles. Particle size in the sample can be calculated using the autocorrelation function of the intensity variations as a foundation. Basic DLS analysis parameters include the diffusion coefficient, and correlation function [12]. A standard DLS configuration comprises a laser light emitter, a sample housing the colloidal solution, and a detector to catch the scattered light as depicted in the figure 1.4. The scattered light is subsequently examined for variations in intensity over a period of time. Contemporary instruments frequently incorporate sophisticated functionalities like temperature regulation and the ability to measure from various angles [92] [12]. The DLS method has the ability to quantify the particles zeta potential, offering valuable

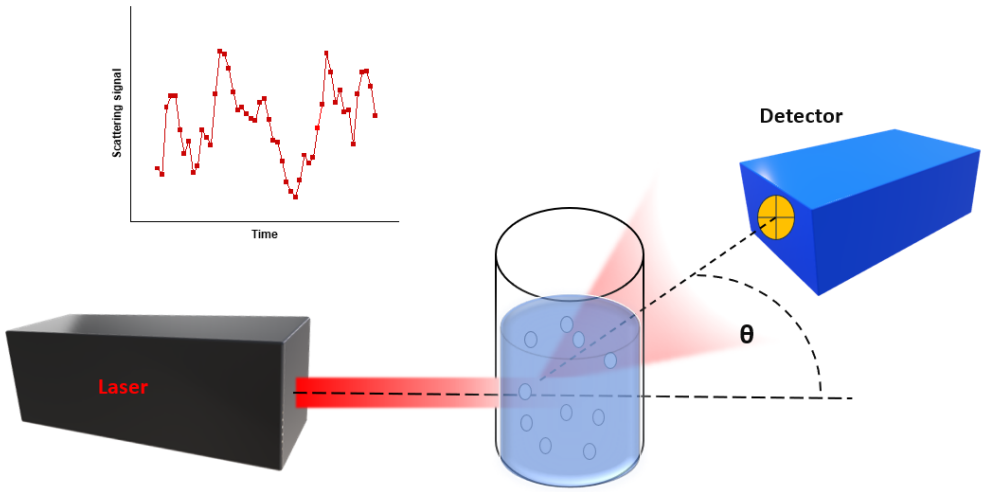

Figure 1.4: Fundamental configuration of DLS measurement system. The specimen is enclosed within a cuvette. The light emitted by the laser can be observed at various angles.

insights into their surface charge and enhancing the understanding of stability and interactions within the system. In biochemistry, DLS plays an important role in protein dynamics studies by allowing the examination of aggregation behaviour and protein size. Furthermore, polymer characterization widely uses DLS to obtain essential information about the distribution of polymers in liquid solutions and their size [92][93]. Hydrodynamic radius and diffusion coefficient are two important quantities that may be derived from the information produced by DLS. Biomedical research relies on DLS to facilitate the investigation of nanoparticles for drug delivery systems.

DLS is essential in the pharmaceutical sector for the characterization of protein aggregates, and it plays a critical role in assessing medication formulation and stability. The use of DLS in environmental science makes it possible to examine the existence of nanoparticles in environmental samples. Moreover, DLS is very useful in the field of materials science, especially to analyse the size distribution of particles in nanomaterials, allowing them to be implemented in various scopes [93][94][12].

1.5.6 Nanoparticle Tracking Analysis (NTA)

Complementary to DLS, Nanoparticle Tracking Analysis (NTA) is a methodology employed for the quantification and characterization of individual nanoparticles. The method was developed during the initial years of the 21st century and has since gained significant recognition as a prevalent approach for investigating nanoparticles at the nanoscale [95]. Similar to DLS, NTA is based on the principles of light scattering and Brownian motion in order to monitor the movements of nanoparticles that are dispersed throughout a fluid media. The technique has the capability to assess the size distribution and concentration of nanoparticles inside a given sample, hence offering significant insights into their physical characteristics. NTA holds significant importance in the examination of particles within the size range of 10 to 1,000 nanometres. This characteristic renders NTA highly relevant across a wide range of practical applications [95]. The Nanoparticle Tracking processing (NTA) system generally comprises a laser light source, an optical microscope, a sample chamber, a high-speed camera, specialised software, and data processing tools. The laser beam illuminates the nanoparticles in the sample, while the optical microscope gathers the scattered light to see and track them. The video data is then analysed by specialised software to follow the movement of each individual particle and determine their size and concentration. The sample chamber contains the suspension of nanoparticles and is frequently regulated for temperature. A high-speed camera captures the random Brownian movement of the nanoparticles [96]. One notable characteristic of the NTA system is its capacity to perform real-time analysis. Through the use of this method, scientists are able to see and track real-time alterations in populations of nanoparticles. Moreover, the NTA technique necessitates only a modest amount of samples. This characteristic makes it very suitable for situations in which the supply of samples is restricted. The NTA method is also non-destructive. The nanoparticles remain unaltered and undamaged throughout the analysis process [95]. NTA is finds applications in several scientific fields, such as drug delivery and nanomedicine. In pharmaceutical research, NTA is used to analyse drug delivery systems and assess the stability of nanoparticles. This process is crucial to guaranteeing the safety and efficacy of pharmaceutical medications. Although the NTA approach has numerous advantages, it also has limitations [97][95]. A significant limitation is the size range within which NTA may be utilised. Particles with a size lower than 10 nanometres are difficult to measure with NTA. Furthermore, it is important to recognise that NTA primarily provides data on the size and concentration of nanoparticles, but it does not produce any information related to their chemical compositions. The issue of adequate sample preparation is an additional obstacle where inadequate outcomes may arise due to the presence of aggregates or insufficiently dispersed particles within the sample. Therefore, thorough preparation is essential in order to attain meaningful results. The proficiency of the operator should also be taken into account. The interpretation of NTA data may require specialised knowledge, and the accuracy of the procedure may depend on the operator's skill level. In addition, it should be noted that NTA may be prone to potential interference caused by the presence of background particles or contaminants inside the sample. This may mandate additional filtration or purification steps to ensure the integrity of the results [98]. Another important consideration is the lack of information on NP shapes with both NTA and DLS.

1.5.7 Tunable Resistive Pulse Sensing (TRPS)

Tunable Resistive Pulse Sensing (TRPS) is method for accurately analysing the size and concentration of particles and can detect and analyse submicron colloids and bioparticles on a particle-by-particle basis [14]. While particles are moving through a pore, TRPS is able to detect changes in the electrical resistance, due to a change in ionic current through the pore. TRPS is particularly suitable for nanoscale research due to the fact that the pore size may be tuned, which enables accurate sizing and numbering of particles [14]. A conventional TRPS configuration includes a nanopore integrated into a membrane, a fluidic system for controlling the movement of particles, and electrodes for quantifying alterations in resistance. The pore size is adjustable, enabling analysis of a wide spectrum of particle sizes. The device detects and measures individual particles as they move through the pore, documenting their size, concentration, and other relevant characteristics [99]. The particles that are present in an electrolyte solution move through a conductive membrane (specifically, a nanopore) by manipulating pressure and voltage values. This membrane is exposed to an applied electrical potential, resulting in the generation of an ionic current. The software of the device detects and measures a resistive pulse signal or "blockade" caused by the passage of each individual particle. The determination of particle volume involves the assessment of pore blockage magnitude, which is subsequently converted into particle size. [14][96]. However, several limitations of TRPS restrict its uses. First, TRPS devices require sophisticated installations and expert operators. Moreover, discrepancies in particle surface characteristics might influence the precision and consistency of TRPS measurements, introducing an additional level of intricacy to the analytic procedure. The extended duration required for data collecting in TRPS, in comparison to methods such as DLS, is acknowledged as a constraint, rendering TRPS less appropriate for time-critical analysis or high-volume applications [100]. Moreover, as with DLS and NTA, also TRPS is not directly sensitive to NP shapes.

1.5.8 Four-Wave Mixing Microscopy (FWM)

The use of nonlinear optics principles in Four-Wave Mixing microscopy (FWM) allows the acquisition of high-resolution, label-free images of biological and material samples, making it an advanced imaging method. FWM microscopy has had a surge in popularity in recent years owing to its ability to provide non-invasive, chemical-specific imaging as well as to detect single small metallic nanoparticles background free, due to their electronic properties [101][8]. This characteristic makes it a desirable instrument in a range of fields, including materials science, biology and nanotechnology. Nonlinear optical microscopy methods leverage the nonlinear behaviour of materials when subjected to strong laser light in order to provide images with enhanced resolution. In its general form, FWM microscopy involves the use of three incident laser beams to produce a fourth wave upon interaction with the sample. Depending on the wavelength of the incident beams, FWM can manifests as a coherent Raman scattering nonlinearity, sensitive to molecular vibrations hence chemically specific [102]. FWM microscopy operates on the general idea of having three laser beams with frequencies ω_1, ω_2, and ω_3 interacting with a nonlinear medium, whereby a fourth beam is produced at frequency ω_4, determined by the equation $\omega_4 = \omega_1 - \omega_2 + \omega_3$. When the frequency difference $\omega_1 - \omega_2$ coincides with a vibrational resonance ω_{vib}, FWM can manifest as a coherent Raman scattering (CRS) nonlinearity, generating a signal at the anti-Stokes shift $\omega_3 + \omega_{\text{vib}}$ [102] [103]. Experimental setups commonly involve the use of an ultrafast laser source that emits pulses in the femtosecond or picosecond range. These pulses generate intense laser fields. Additionally, three laser beams with different frequencies are combined and directed towards the sample. Scanning procedures are employed, such as placing the specimen on a motorised stage for precise positioning or using galvo scanning mirrors to

scan the incident beams. Detection systems are responsible for collecting and separating the generated FWM signal from the incident beams. Photomultipliers or photodiodes are commonly used as light detectors in these systems [104].

FWM microscopy has several applications. For example, in biomedical research, label-free CRS imaging of living cells and tissues reveals cell shape, lipid content, and protein distribution. FWM microscopy has wide range of application in material science for example it can be use in organic polymer study , metals and inorganic semiconductors . FWM techniques can investigate dispersion of contaminants in samples [102]. Although FWM has extensive advantages, it also has disadvantages. These include the requirement for complex and costly apparatus, and the susceptibility of the sample to potential harm caused by the intense laser intensities [103].

1.6 Optical Extinction Microscopy

This section gives a description of optical extinction microscopy, a key modality used in this thesis to quantify the size and shapes of individual AgNPs. It provides an overview of the background and relevance of measuring the optical extinction cross-section, along with its many uses. The fundamental notions and advantages associated with this concept are also discussed.

1.6.1 Technique principle

The phenomenon of light extinction can be described as follows. Under an incident light illumination, a particle scatters and absorbs light, which reduces the amount of light transmitted. Notably, particles scatter and absorb light with a strength which depends on their size, shape, and material composition. Hence, this effect can be used to quantify their morphology. Light scattering and absorption are interrelated processes [19]. The physical quantity used to describe optical extinction, i.e. the attenuation of light due to absorption and scattering, is the so-called extinction cross section, determined by the sum of the scattering σ_{Sca} and absorption σ_{abs} cross sections, as per formula below:

$$\sigma_{\mathrm{ext}} = \sigma_{\mathrm{sca}} + \sigma_{\mathrm{abs}} \tag{1.1}$$

where σ_{ext} is the optical extinction cross section. This cross-section as the units of an area that, when multiplied by the incident light intensity, yields the power scattered and absorbed by a sample

$$\sigma_{\mathrm{ext}} = \frac{P_{\mathrm{ext}}}{I_{\mathrm{i}}} \tag{1.2}$$

P_{ext} is lost power through extinction and I_{i} the incident intensity. The optical extinction cross section can be measured by using transmission microscopy. The main optical set-up typically comprises an optical illumination source like a halogen lamp or a light-emitting diode (LED), which is used to illuminate a sample. The incident light is focused onto the sample by appropriate optics (condenser lens) and the interactions between the sample and the incident light result in changes of the transmitted intensity. In order to capture these variations, a microscope objective is used to collect the transmitted light after the sample. The objective lens focuses the transmitted light and produces a image of the specimen. A camera detector is typically utilised to capture the magnified image, enabling quantitative analysis. Extinction microscopy may use additional components such as polarisers to control the polarisation of light. In this study, we imaged Ag nanoplates with PVP coating and silica shells, which were nominal triangle of approximately 40 nm diameter and 10nm thickness, but in practice exhibited various shapes, including hexagonal, spherical, rod, and triangular morphologies. Additionally, we imaged PVP-coated Ag nanoplates, also nominally triangles of approximately 70 nm diameter and 10nm thickness, and spherical Au NPs of 30 nm in diameter. The size and shape of the nanoparticles played

a crucial role in determining their optical and plasmonic properties, which were characterized quantitative. The specific Ag nanoplates were chosen to push the optical extinction microscopy method beyond simple shapes, and also based on availability from commercial manufacturers. To that end, more/future work will need to explore different, e.g. smaller, nanoparticles and a broader range of compositions and shapes to further understand the impact of these properties on optical extinction, particularly for applications requiring precise control over surface plasmon resonance. Moreover, smaller NPs might offer improved colloidal stability or unique biomedical functionalities due to increased surface-area-to-volume ratios. Similarly, alternative compositions and anisotropic shapes could further enhance optical absorption and tunability for specific biomedical applications.

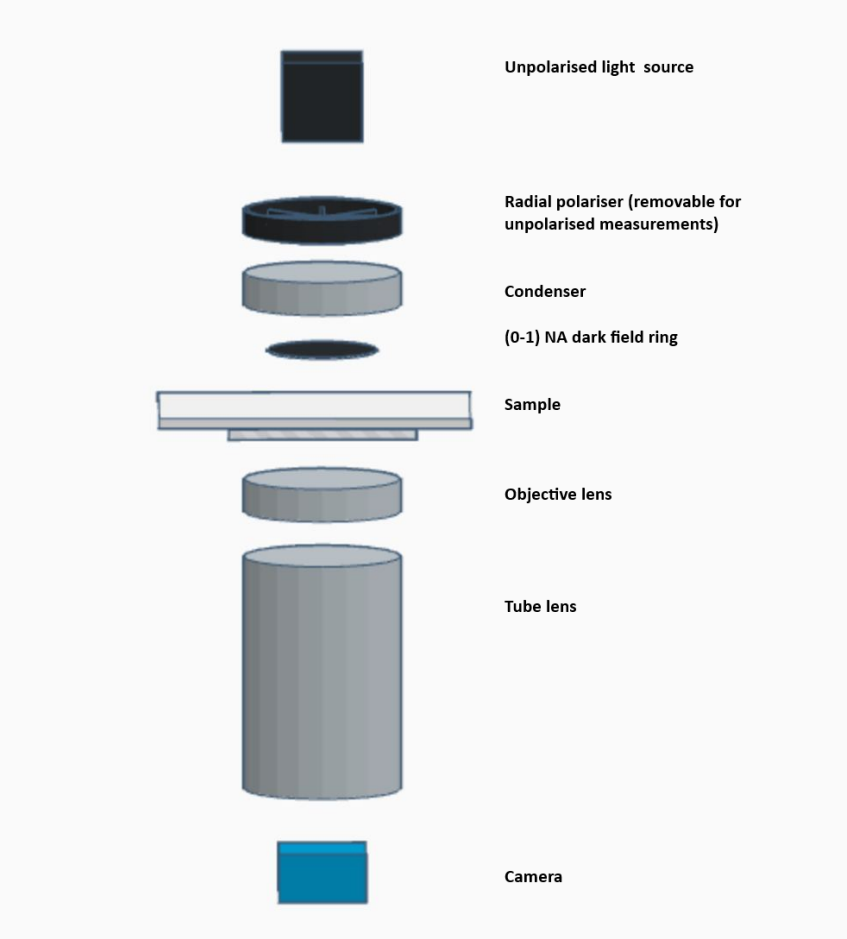

Figure 1.5: Extinction microscopy set up. Illustration representing an example of elements utilised for the extinction measurements.

1.6.2 Applications of extinction microscopy

Wide-field optical extinction microscopy offers an easy, rapid, and cost-effective way to characterise the size and shape of individual nanoparticles. Quantitative measurements of the optical extinction cross-section of single nanoparticles has many applications in material science, physics, chemistry biology and medicine [10]. Beyond nanoparticles, extinction microscopy, as exemplified in [105], can be used to measure the extinction coefficients of biological substances. This method enables the assessment of the absorption characteristics of translucent cells, such as liver sinusoidal endothelial cells (LSECs), which are usually difficult to visualise using conventional techniques. In this case, extinction microscopy uses UV light to analyse biological samples without the need for labelling. This technique offers a high level of contrast and resolution, and might be applied in diverse domains such as pathology, plant biology, and microbiology [105]. For nanoparticle analysis, single-particle extinction microscopy, has also been employed to conduct time-resolved investigations, for example of acoustic vibrations and time-resolved dynamics [106]. Generally, it enables the capture of images of individual nanoparticles, offering quantitative insights into their optical and morphometric properties [107][9][106]. These applications highlight the importance of the optical extinction microscopy in promoting studies across a variety of scientific fields.

1.7 Thesis motivation and structure

The primary motivation behind this study has been to further develop and apply the optical extinction microscopy technique for quantifying the morphometric properties of various types of individual silver, as well as spherical gold, nanoparticles. As mentioned in the previous section, optical extinction microscopy offers a fast and accurate technique for analysing the size and shape of absorbing and scattering metallic NPs the single-particle level. The method involves measuring the optical extinction cross-section of individual NPs at different wavelengths while also considering their polarisation properties. Notably, single-particle analysis methods overcome the limitation of ensemble-averaged approaches which mask variations in individual particle properties. However, in order to obtain statistically relevant information on size and shape distributions, especially for heterogeneous populations of NPs, single-particle methods need to be performed in a high-throughput modality. Our technique provides this key feature by utilising wide-field transmission microscopy to simultaneously capture images of hundreds of individual NPs inside the field of view. Previous work in the Borri-Langbein group has focused on developing and demonstrating quantitative optical extinction micro-spectroscopy with colloidal nanoparticles of simple shapes such as gold sphere and rods [108][109][9], for which mathematical formulas of the extinction cross section exist. Conversely, in this thesis, we investigated silver nanoparticles with non-trivial geometries, namely thin nanoplates of nominal triangular in-plane shape, in practice exhibiting a heterogeneous distribution of shapes, including hexagons of non-equal sides. Particular attention was devoted to developing new methods able to characterize the thin axial size as well as the in-plane shape, complementing topographic methods such as AFM. To that end, an optical configuration was developed to generate axially polarized light at the sample plane (as described in details in Chapter 3), enabling us to distinguish flat thin nanoplates from spherical NPs. Small gold nanoparticles (AuNPs) of around 30 nm diameter were included in the study, as a "positive control" sample, to benchmark the new technique against nanoparticles of well-defined geometry. The use of a radial polariser to generate axially polarized light at the sample plane was combined with a new quantitative data analysis pipeline. Specifically, quantitative measurements of the extinction cross-section over many (typically hundreds) individual nanoparticles were grouped using cluster analysis, through the definition of

appropriate predictors, with the view to separate nanoparticles according to their different morphometry. The thesis is structure as follows. Chapter 2 provides details on the materials and methods. Chapter 3 focuses on the analysis on nanoparticles deposited on a surface, and introduces a cluster analysis method developed in house to separate nanoparticles of different sizes/shapes. Chapter 4 describes the measurements and analysis of silver nanoplates floating a viscous medium. This approach was introduced to physically average over the nanoparticle orientation, in order to improve the morphometric characterisation of silver nanoplates, by removing their orientation as a variable in the cluster analysis. Chapter 5 describes the work carried out to characterise the thickness of individual silver nanoplates using AFM. A sample preparation method was also developed, aimed at measuring the same silver nanoparticle by AFM and extinction microscopy, correlatively, and is described in Chapter 5. Chapter 6 shows the optical extinction cross-section analysis carried out on a selection of nanoparticles that were measured using FWM, and exhibited reshaping due to the laser exposure. Finaly, Chapter 7 provides a summary and an outlook for this work.

Chapter 2

Material and methods

This chapter examines the description of the samples prepared and the materials used, as well as the different instruments and arrangements used to conduct the experiments described in Chapters 3, 4, 5 and 6.

2.1 Materials

2.1.1 Silver nanoplates coated polyvinylpirrolidone (PVP-AgNPL)

Stock solutions of silver nanoparticles were supplied by the manufacturer company nanoComposix. Two different types of solutions were purchased.The first type consisted of silver nanoparticles coated with PVP with an average diameter of 40 nm±15 nm, an estimated thickness of 10 nm, 0.021 mg/mL mass concentration in 5mM sodium borate and a peak absorption wavelength around 650 nm (lot number IAD0038), as shown in Fig. 2.1. Fig. 2.2 display the other type of PVP- NPLs with 70nm±20nm size and 10 nm thickness (lot number TJC0092), 1.07 mg/mL mass concentration in 5 mM sodium borate has a peak absorption wavelength around 800 nm. PVP-NPLs supplied by Nanocomposix are layered with polyvinylpyrrolidone (PVP) to improve the biocompatibility, stability , surface toxicity and surface functionality. This increases their applicability in numerous fields, such as biology, medicine, and materials science [30]. The collective mean optical absorbance spectra of the 70nm PVP-AgNPLs stock (see Fig. 2.2) exhibits the main LSPR centred at 815 nm with full-width at half maximum (FWHM) of 136 nm. Additionally, there is a less intense band in the range of 333-453 nm and a further diminished peak at 333nm.

2.1.2 Silver nanoplates with silica shell (SiO_2-AgNPLs)

There are several advantages to coating AgNPLs with a silica shell. The silica layer serves as a protective barrier that prevents direct interaction between the silver material and the environment. This coating helps to prevent nanoparticle aggregation and blocks the release of silver ions. Moreover, the silica shell provides a functional surface that can be further modified with other molecules or coatings for specialized applications[110]. To leverage these properties, SiO_2-AgNPLs were utilized, with a core silver diameter of approximately 40 nm ± 8 nm, a thickness of 10 nm, an estimated silica shell thickness of 10 nm, and a peak absorption wavelength of 657 nm in aqueous buffer (lot number DMW0588). These nanoparticles were suspended at a concentration of 1.05 mg/mL in 10 mM bicarbonate buffer (see Fig. 2.3).

Various methods can be employed to coat nanoparticles with polyvinylpyrrolidone (PVP) or silica shells to enhance their stability. The primary function of the PVP polymer is to act as a steric stabilizer due to its amphiphilic nature, preventing nanoparticle aggregation by creating

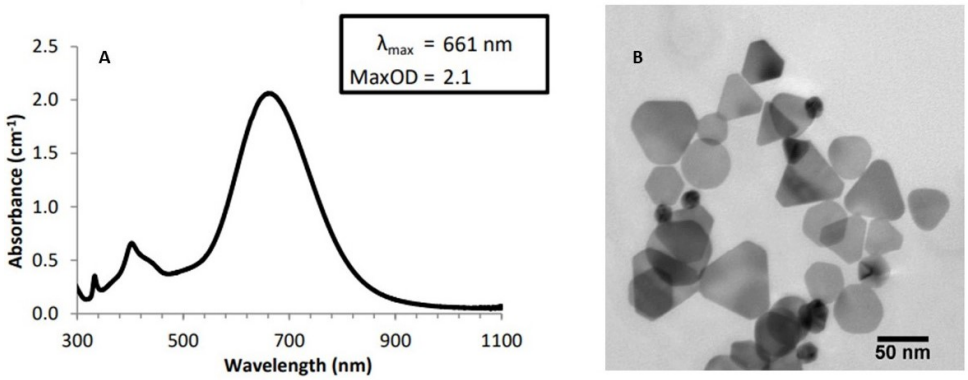

Figure 2.1: PVP-coated silver nanoplates of nominal 40nm size (A) Ensemble absorption spectrum provided by the manufacturer; (B) Electron microscopy images provided by the manufacturer nanoComposix, showing the different size and shape of 40 AgNPLs coated with PVP.

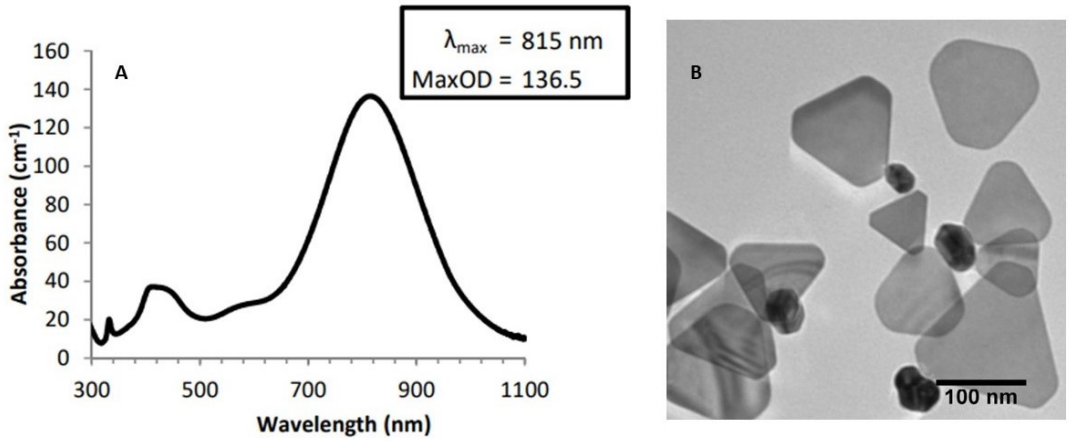

Figure 2.2: PVP-coated silver nanoplates of nominal 70nm size (A) Ensemble absorption spectrum provided by the manufacturer; (B) Electron microscopy images provided by the manufacturer nanoComposix, showing the different size and shape of 70 AgNPLs coated with PVP.

a physical barrier around them. This feature promotes uniform dispersion in different media and allows better control over the growth and structure of the nanoparticles. The stabilizing effect of PVP is particularly beneficial in catalysis applications [111]. On the other hand, silica shells provide a robust protective coating, offering greater stability while allowing for further surface modification and enhancing biocompatibility. Silica-coated nanoparticles are often used in biomedical applications due to their inert nature and ability to reduce toxicity compared to uncoated nanoparticles. Additionally, the morphology and thickness of the silica shell can be precisely controlled to meet the requirements of various applications that demand consistent surface properties[112].

The choice between PVP and silica shell coatings for nanoparticles largely depends on the specific needs of the application. For applications requiring a flexible and adaptable stabilizer,

PVP is the preferred option. It is particularly effective in catalysis and nanomedicine, where it enhances solubility and facilitates nanoparticle formation [111]. PVP's amphiphilic properties allow it to interact with a wide range of solvents and substrates, making it valuable for the synthesis of diverse nanostructures. Conversely, for applications requiring stronger protection and biological compatibility, such as in biomedical imaging and drug delivery, silica shells are often favored[112].

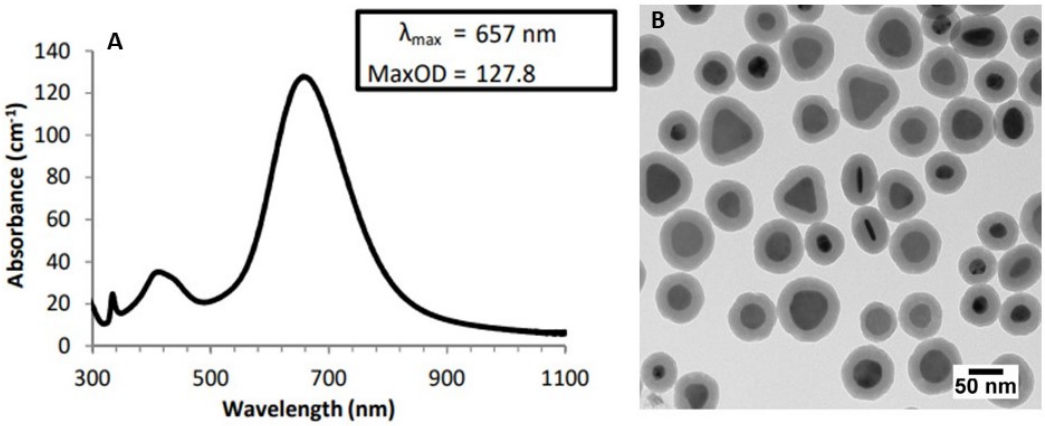

Figure 2.3: Characteristics of SiO_2-AgNPLs coated nano plates 40nm size (A) Ensemble absorption spectrum provided by the manufacturer; (B) Electron microscopy images provided by the manufacturer nanoComposix, showing the different size and shape of 40 SiO_2-AgNPLs.

2.1.3 Gold nanoparticles (AuNPs)

In this study, 30nm-sized gold nanospheres from "nanoComposix" (lot number JSF0124) were used, having a 522 nm peak absorption wavelength, 0.02 mg/mL mass concentration in 2mM sodium citrate and uniform 30 nm size as it can be seen in Fig. 2.4 .

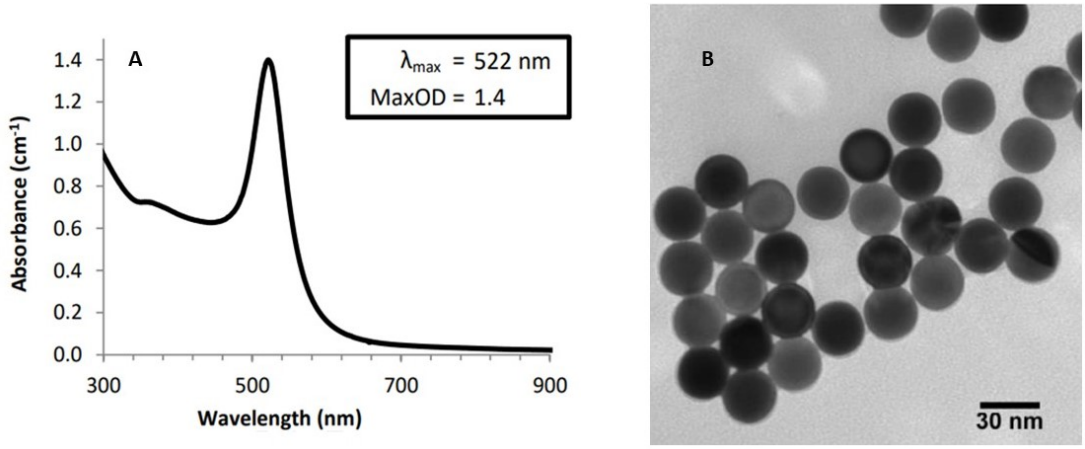

Figure 2.4: Nominally spherical ultra-uniform AuNPs (A) Ensemble absorption spectrum provided by the manufacturer; (B) Electron microscopy images provided by the manufacturer nanoComposix shows the size and shape of 30 nm AuNPs.

2.2 Chemicals and other materials

A variety of chemicals, glassware, and other materials were put to use in the course of the present research. Acetone, ethanol, polyvinylpirrolidone average mol wt40000 Da (daltons)(Lot#BCBK-8609V) and 30% hydrogen peroxide were acquired from Sigma-Aldrich. The samples were prepared using glass slides and coverslips obtained from Menzel-Gläser (#1.5). The immersion silicon oil, with a refractive index of 1.518 (AP150) originated from (Wacker). The borosilicate glass beakers of different sizes and 50ml Falcon tubes and toluene (with 99.8% purity) (Lot:2046854) were procured from Fisher Scientific (Loughborough, UK). A 50 mM borate buffer (Lot: VL315360) was acquired from Thermoscientific (USA). Honey (commercial honey purchased from a Lidl supermarket for food consumption comprises a sugar content of 79.7 grammes per 100 grammes of honey). As discussed in Chapter 4, honey was used as a viscous medium in which SiO2-AgNPLs are freely diffusing. The aim is to measure the optical extinction of SiO2-AgNPLs over an observation period where rotational diffusion provides a time-averaged over the particle orientations, while at the same time the particle is not translationally diffusing out of focus. Honey was chosen as a high-viscosity medium for that purpose. Depending on its water content, honey can reach viscosities >20 Pa s [113] , more than 10 times the viscosity of glycerol which is 1.4 Pa s at room temperature.

2.3 Preparation of samples for extinction microscopy

2.3.1 Glass cleaning process

A thorough and systematic cleaning procedure must be applied on glass slides to avoid debris and enable observation of silver and gold nanoparticles under extinction microscopy. The cleaning process must be carefully executed throughout several steps. Glass slides of 51 mm x 26 mm and cover slips of 24mm x 24mm side and #1.5, i.e., around 170 microns thickness are cleaned by consecutive sonication steps in different solvents, with 20 minutes per step. The first step is done by immersing the cover slip and the slides in a toluene solution to guarantee the removal of any non-polar substances, then acetone to remove the residues of stuck toluene. After that, both cover slips and slide are going to be rinsed and treated with boiling deionized water.

Next, the samples must be held in a solution with a concentration of 30% of hydrogen peroxide for at least one day before they become ready for sample preparation enabling the oxidation of any remaining surface impurities, while also making the glass surfaces more hydrophilic. It is important to note that numerous problems with the cleaning process's efficacy have been encountered in numerous instances, and the surface exhibited only moderate hydrophilicity. Due to the gradual decay of H_2O_2 into H_2O over time, it was discovered that older H_2O_2 produced comparatively fewer bubbles at the surface upon addition. This was used as a qualitative metric to determine if the H_2O_2 supply needed to be replenished. H_2O_2 acts as a powerful oxidizing agent in glass cleaning, effectively breaking down organic stains and residues. It can also help eliminate bacteria and mold, contributing to a more hygienic surface. Additionally, H_2O_2 can enhance the overall clarity and remove grime without leaving streaks on the glass surface [114]. Glass cleaning procedures were developed through the accumulated efforts of the group members in Borri's laboratory.

2.3.2 Wet casting

To deposit silver nanoparticles onto a glass surface, a wet casting method was applied. Initially, the concentration of the nanoparticles to be applied onto the glass slide is determined by considering the dimensions of NPs and the concentration of the stock solution provided by the manufacturer. For this estimate, in the case of the PVP-coated AgNPLs with a nominal edge length of 40 nm, guided by TEM, triangular nanoplates are considered with a specified edge length of 40 nm and a thickness of 10 nm. The known mass density of silver is 10.49 g/cm^3. The NP density was determined to be 2.9x10^{11} NPs/mL (as shown in the approximate calculations below).

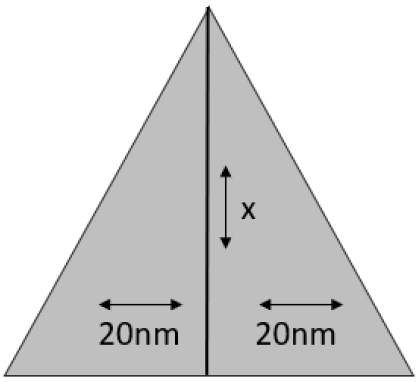

Figure 2.5: Triangular AgNPL: The dimensions of single triangular Ag nano plate.

The surface area A of the triangle is calculated as $A = b \cdot \frac{x}{2}$, where $b = 40\,\text{nm}$ and x is given by the triangle formula: :

$$40^2 = 20^2 + x^2, \tag{2.1}$$

$$x = 34.64 \text{ nm}$$

The volume of a traingular AgNPL is

$$V = A \times H \tag{2.2}$$

where A is the area of traingle and H is the 10 nm thickness according to the information provided by the manufacturer

$$V = 6.928 \times 10^{-24}\,\text{m}^3 \tag{2.3}$$

The following calculations are made with respect to the 50mL PVP-AgNPLs stock solution provided by nanoComposix. The manufacture provided us with the mass concentration MC of silver in the solution, from which we can determine the total mass $M(Ag)$ of silver in the stock volume Vs as.

$$MC = \frac{M(Ag)}{V_s} \tag{2.4}$$

$$0.021\text{mg/mL} = \frac{M(Ag)}{50\text{mL}} \tag{2.5}$$

$$M(\text{Ag}) = 1.05 \times 10^{-3}\text{g} \tag{2.6}$$

We can calculate the mass m of a single nanoplate using the known density of silver and the volume V of the nanoplate:

$$10490\text{Kg/m}^3 = \frac{m}{6.928 \times 10^{-24}\ \text{m}^3} \tag{2.7}$$

$$m = 7.267 \times 10^{-17}\text{g} \tag{2.8}$$

The number of PVP-AgNPLs particles in 50 mL of a 0.021 mg/mL suspension is then given by the total mass $M(Ag)$ divided by the mass m of a single plate:

$$NOP = \frac{1.05 \times 10^{-3}\text{g}}{7.267 \times 10^{-17}\text{g}} \tag{2.9}$$

$$NOP = 1.444 \times 10^{13} NPs \tag{2.10}$$

From this NOP in 50mL we can calculate the nanoparticle concentration, as number of particles per unit volume: $\rho = 2.9 \times 10^{11}$Nps /mL

Following the same assumptions, the densities of 40 nm SiO_2-AgNPLs, 70nm PVP-AgNPLs and Au NPs were calculated as $2.9 * 10^{11}$ nanoparticles /mL , $2.9 * 10^{11}$ NPs/mL , $2.291 * 10^{10}$ NPs/mL respectively. The resulting average NP distance was estimated to be about 6µm assuming all NPs attach onto the surface of a 24 mmx24 mm coverslip, when pipetting a 50µL volume of solution diluted from the stock. This average distance was required, so that the majority of nanoplates can be resolved with well-separated point spread functions in the absence of aggregation. To ensure the completion of the aforementioned undertaking, the stock solution had a dilution of 1:1000 using a 5mM Borate buffer.

After the process of preparing the concentrations and before depositing NPs, the slides and cover slips are rinsed with DI water and dried with nitrogen flow, and then 50μL of the diluted solution is cast across the coverslip area. It is very important to maintain a wet atmosphere by placing wet wipes near the coverslip area and covering the sample with a petri dish to prevent drying (hence the name "wet" casting). We chose this method because if the samples are placed in a dry environment, there will be a surface tension, and the particles will start to aggregate, making it very difficult to control the surface density. Conversely, using a wet atmosphere the particles will sediment and attach to the surface of the coverslips without aggregation. The samples are placed in a wet atmosphere for one hour, and subsequently, any remaining liquid on the coverslip is carefully removed by rinsing it with DI water. Later, the coverslip was placed in a vertical position to allow the water to drain off and finally dried using a flow of nitrogen. After that, 25 µL silicon oil index matched to glass was pipetted onto the surface of the cover slip to provide an index-matched medium surrounding the NPs. Subsequently, a glass slide was placed over the surface. The coverslip was pressed on the slide manually to decrease the thickness of the oil. Any extra oil on the borders of the coverslip was removed by using cleanroom tissue soaked in acetone. As last step, the sample was enclosed by sealing the coverslip edges with nail varnish. see Fig. 2.6.

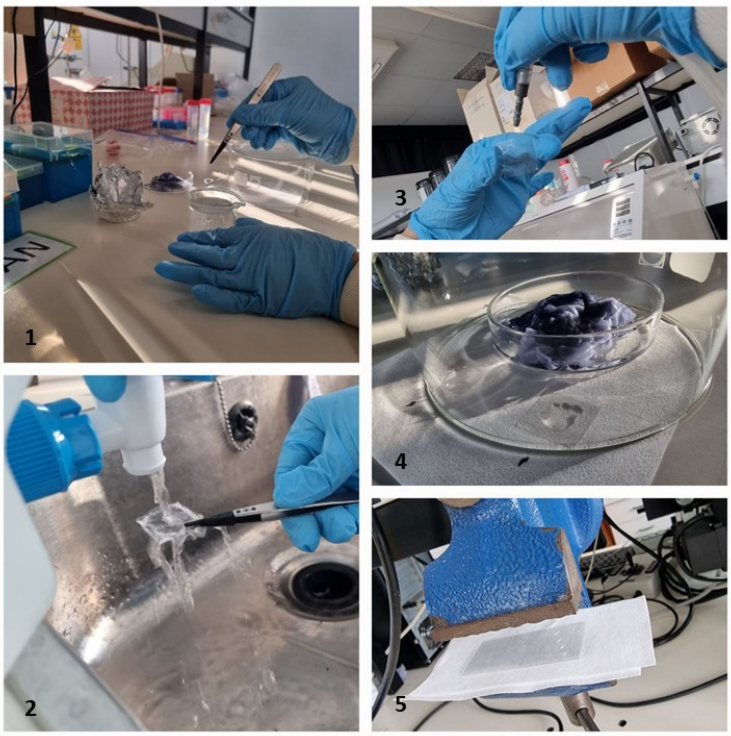

Figure 2.6: Wet casting method: The images summarise the sequence of steps for the wet casting method, beginning with (1,2) removing the H_2O_2 by rinsing the glass slide and coverslips with DI water (3) drying the coverslips with a flow of nitrogen (4) pouring the NPs solution and keeping the sample in wet atmosphere (5) adding the silicon oil then squeezing and sealing the samples.

2.3.3 Embedding NPs in viscous medium

As discussed in Chapter 4, we acquired the extinction cross-section of Ag nanoplates while they are diffusing in a medium of controlled viscosity. The aim is to enable NPs to rotate over the observation time needed to acquire the cross-section, in a way such that the measured extinction value is an average over the NP orientation angles. On the other hand, the translational diffusion of NPs needs to be sufficiently slow, to avoid that this motion is blurring the optical point-spread function, which would affect the quantitative image analysis pipeline. To that end, calculations have been performed to determine the optimal viscosity. For Brownian diffusion [115]

$$L^2 = 2Dt \tag{2.11}$$

where L is the root mean square displacement, D Diffusion constant and t time of measurement. Our condition requires L to be below 100nm, to avoid blurring the optical point spread function, which results in:

$$(100 * 10^{-9})^2 \mathrm{m}^2 > 2D \times 20\mathrm{s} \tag{2.12}$$

$$10^{-14} \mathrm{m}^2 > 2D \times 20\mathrm{s} \tag{2.13}$$

$$D < \frac{10^{-14}\,\mathrm{m}^2}{2 \times 20\,\mathrm{s}} \tag{2.14}$$

The value of D is substituted into the following equation.

$$D = \frac{K_B T}{6\pi R \eta} \tag{2.15}$$

where kB Boltzmann constant, T Absolute temperature (in kelvin), (η) Viscosity and R: Spherical particle radius assumed to be 20 nm for this estimate

$$\frac{1.3806 \times 10^{-23}\ \frac{\mathrm{m}^2\,\mathrm{Kg}}{\mathrm{s}^2} \times 293 \times 20\,\mathrm{s}}{3 \times 3.14 \times (20 \times 10^{-9})\,\mathrm{m} \times 10^{-14} \times \mathrm{m}^2} < \eta \tag{2.16}$$

$$\mathrm{P}a.s43 < \eta(\mathrm{Pa\ is\ Pascal}) \tag{2.17}$$

It was found that honey could be the viscous medium within the calculated range of viscosity. Honey crystallises in different ways depending on its unique composition and the amount of sugar it contains. As stated in Section 2.3.1, it is crucial to maintain the cleanliness of the glass substrate in this specific method, as honey will act as an intermediary substance between the glass and the coverslip. The honey must be well purified and free from any contaminants or debris. The process of honey sample preparation includes three different stages. The first step requires the purifying of honey. Afterward, the concentration of the AgNPLs solvent is modified by mixing it with honey. In the last stage, the honey solution is cast on the coverslip. A purification strategy was developed to cleanse the honey by mixing it with 20% water. The procedure involves utilizing 1 mL of honey and adding 144 μL of water, based on weight ratios of 20%. Following a 30-second sonication of the water and honey mixture, the resulting solution was subjected to centrifugation at 20000 rpm for 15 minutes to facilitate the settling of sugar particles or debris. A portion comprising the top 60% of the mixture was extracted. Subsequently, the honey was subjected to a temperature of 50 degrees in order to eliminate any excess water and preserve the original viscosity of the honey. The next step involves the creation of concentrates that are particular to each sample. 2.5 µL of a stock solution containing SiO_2-AgNPLs was combined with 1mL of honey. A sonicator stick was employed to ensure complete and thorough

mixing. The solution containing SiO_2-AgNPLs was subjected to heating at a temperature of $50C^0$ for a duration of 5 minutes in order to remove the bicarbonate buffer present in the stock solution. The samples are created by dispensing 10 µL of the prepared concentration onto a clean coverslip, which is subsequently covered with a glass slide. A flat weight weighing 800 grammes is then placed on the sample for a duration of 5 minutes to achieve a layer that is as homogeneous as possible see Fig. 2.7. The last stage involves preparing the sample, where the honey's viscosity, time and applied weight carefully controlled to get the 10 µm thickness of the sample [116].

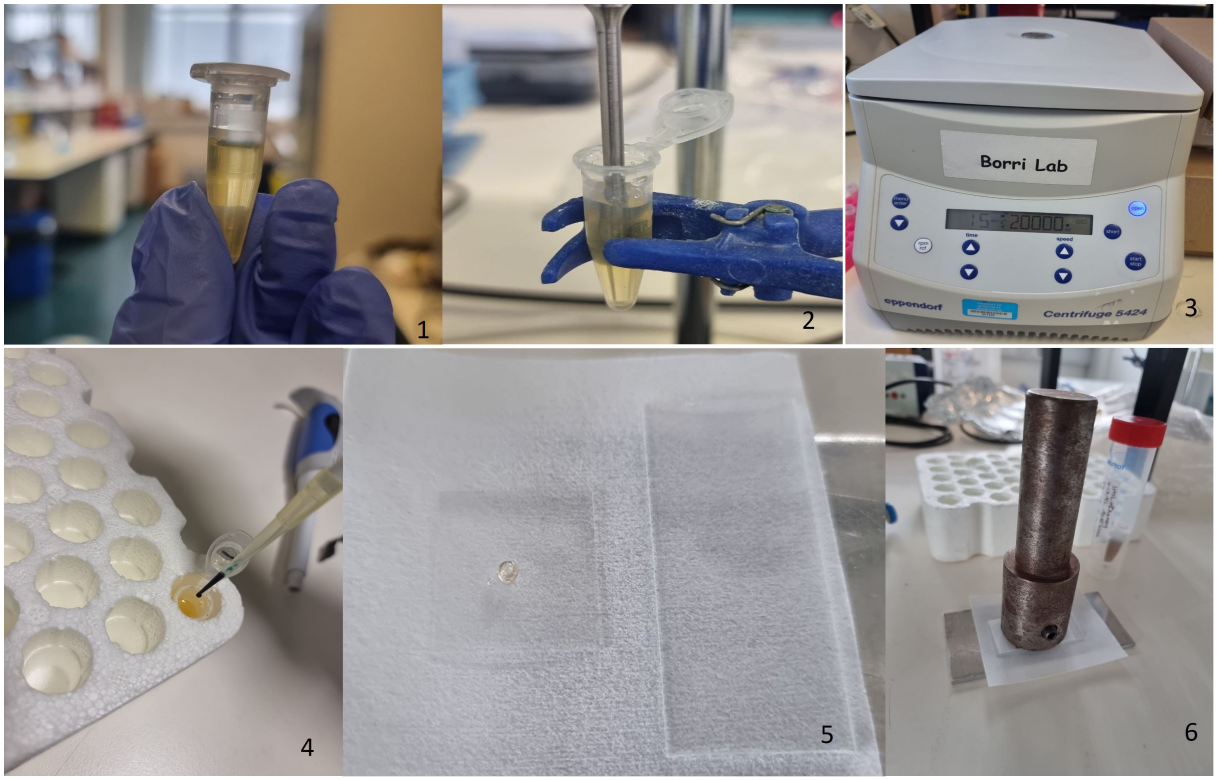

Figure 2.7: Sample preparation embedding NPs in viscous medium. The diagram summarizes the sequence of steps for sample preparation using honey as a viscous medium, beginning with (1, 2) adding and mixing honey with 20% water, (3) centrifuging the mixture for 15 minutes, (4) adding the SiO_2-AgNPLs to the purified honey, (5) pipetting the mixture of honey and SiO_2-AgNPLs onto the coverslip, and (6) applying a weight to obtain a homogeneous sample.

2.4 Measurements

2.4.1 Optical extinction microscope set-up

The primary instrument utilised in this study is a Nikon Ti-U inverted microscope. In order to achieve optimal lighting conditions, a halogen lamp (TI-DH DIA Nikon) with a power output of 100 W was employed with a diffuser and bandpass filters (FKB-VIS-40, Thorlabs) with a width of 40 nm and a centre wavelength that spans the range of 500 nm to 750 nm in 50 nm steps, applied sequentially. The lamp was turned on and adjusted to ensure a stable output and to prevent any fluctuations. Using a 1.34 NA oil-immersion condenser (Nikon MEL41410), the light was directed onto the sample. Either a radial polariser or a rotatable linear polariser at an angle γ_P controlled the light polarisation in the collimated beam path to the condenser. The position of the sample was precisely controlled in three dimensions using a piezoelectric nanopositioning stage (Mad City Labs NanoLP200). A 100×1.45 NA oil immersion objective (Nikon MRD01905) and a $1\times$ tube lens were used to capture the transmitted light. The camera, a PCO Edge 5.5 scientific-CMOS (sCMOS) model, could capture 100 frames per second at 2560×2160 pixels of $6.5\,\mu$m size and had a full well capacity (N_{fw}) 30,000 electrons. The power density is calculated as 3 mW/mm^2, derived from the following parameters: a pixel size of 6.5 μm, 20,000 electrons, an exposure time of 2 ms, $100\times$ magnification, a photon energy of 2 eV, 50% quantum efficiency, and 50% transmission from the sample to the camera. The calculation is given by:

$$\frac{20{,}000 \cdot 1.6\times10^{-19}\,\mathrm{J} \cdot 2}{0.5 \cdot 0.5} \div \frac{2\times10^{-3}}{\left(\frac{6.5\times10^{-3}\,\mathrm{mm}}{100}\right)^2} = 3\,\mathrm{mW/mm^2}.$$

MultiCARS software was created by Prof. Wolfgang Langbein and is coded using Labwindows/CVI. This programme efficiently controls many movable parts of the microscope, including filters, the nano-stage, and the objective lens, while also easing the acquisition of data.

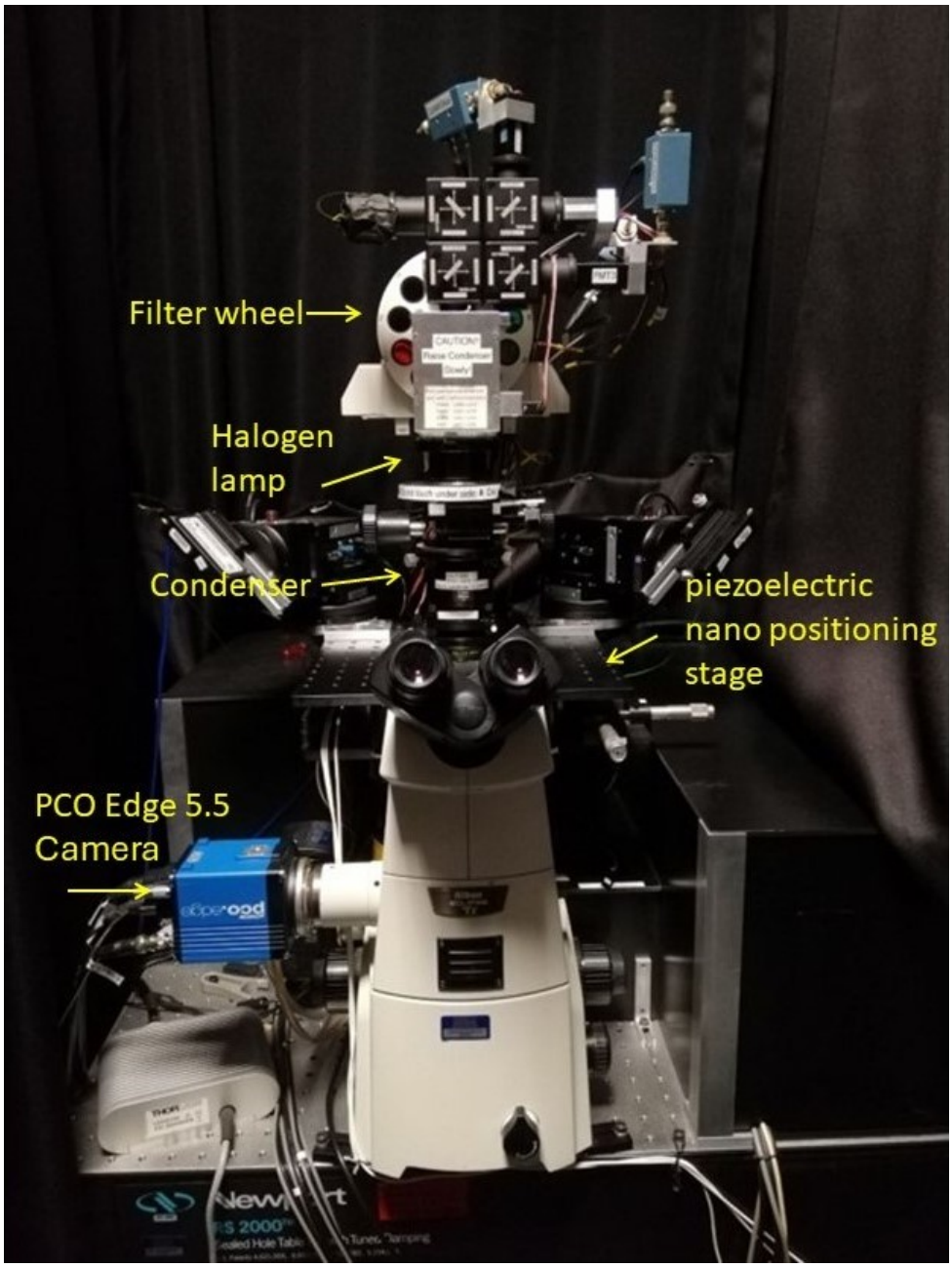

Figure 2.8: Nikon Microscope the image illustrate the Ti-U microscope from Nikon company with all the components used to acquire the data for different samples.

2.4.2 Linear and radial polariser

A radial polariser is an optical component utilized for managing the direction of polarisation of light in microscopes. A radial polariser is designed to transform unpolarised light into radially polarised light meaning that the electrical vectors in the light waves are aligned in a radial direction [117][118]. Our laboratory has constructed a radial polariser as well as a rotatable linear polariser. An aluminium wire-grid polariser foil (MLP-WG, MeCan, USA) was utilised that exhibits a co-polarised transmission of 90% and less than 0.1% cross polarised over the wavelength range of 400-1200 nm. Compared with traditional film polarisers, which usually have a transmission of 50% and a spectral range of 400-700 nm, this film offers a wider spectral range and better transmission. Using a 3D printed holder, a 6-segment disc was constructed as illustrated in Fig. 2.9 a and b. The foil was cut into separate segments along their symmetry lines (see yellow arrows in Fig. 2.9 b). To make a rotatable linear polariser, in the Nikon Ti-U illumination path, the polariser of the de-Senarmont compensator (T-P2 DIC Polariser HT MEN51941, Nikon) was replaced with a 3D printed servo-actuated mount, which allowed the film to rotate and work as a linear polariser (Fig. 2.9 c). A digital 3-turn RC servo (GWSnS125-3T-D/2BB) and a 90-degree gear were used to motorize the rotation of the linear polariser. A digital RC servo (Futaba S3150) and a linear gear were used to motorize the insertion of the DIC module, which provided a switch between the linear and radial polarisers. The Ultimaker 3 Extended was used to 3D print the mounts and gears. The print head was AA 0.25 and the layer thickness was 0.1mm. The material used was black PLA or ABS.

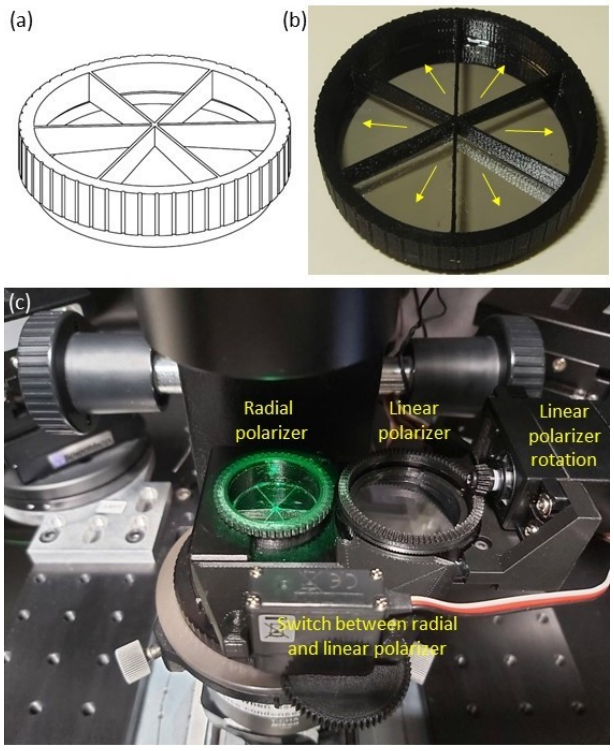

Figure 2.9: Linear and radial polarisers (a) Radial polariser drawing. (b) Assembled radial polariser. (c) Polarisers on a modified de-Senarmont unit (T-P2 DIC Polariser HT MEN51941, Nikon) with servo-automation of linear angle and switch between linear and radial polarisers in the Ti-U trans-illumination pathway.

2.4.3 Dark annular ring

To block the central illumination of the $0-1$ NA range in radial polarisation, a replacement was made to the oil-immersion condenser by constructing an inset that replaced a Nikon PH1 module. This is illustrated in Figure 2.10. This inset is specifically designed to provide darkfield contrast. It contains discs of varying diameters that match lower NA limitations of illumination. In this experiment, we used the 1.0 NA disc and set the condenser aperture to its maximum value of 1.34 NA.

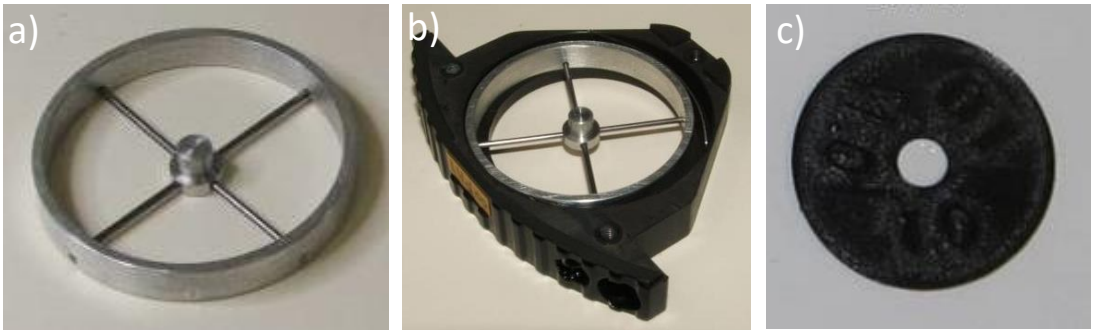

Figure 2.10: Details of the dark-field disc. a) The dark-field disc holder.b) The holder has been placed in the PH1 module of the oil immersion condenser (T-C HNA-OIL High N.A. MEL41410, Nikon), replacing the original PH1 inset provided by Nikon. c) A 1.0 NA darkfield disc was placed to achieve radial polarisation.

2.4.4 Collecting and analysing optical exctinction microscopy data

The process of collecting data starts after the sample has been mounted and is ready to observe under the microscope (see Fig. 2.11). After the setup has been configured, the sample is mounted directly on the objective lens after dropping a small amount of immersion silicon oil with a refractive index of 1.52. Every sample was examined using a PCOs camera able to collect (10-100) images averaging 128 frames. The data was acquired using the shifting method. This method involves two transmission images, I_1 and I_2, that are captured in which a particle of interest is positioned at P_1 in the first image and the sample is laterally shifted by a distance of 1.8 µm (larger than the spatial resolution) resulting in a new particle position, P_2, in the second image. Two extinction contrast images, Δ_1 and Δ_2, are produced to show a differential transmission contrast. Δ_1 is calculated as

$$(\Delta_1) = (1 - \frac{I_1}{I_2}), \tag{2.18}$$

while Δ_2 is calculated as

$$(\Delta_2) = (1 - \frac{I_2}{I_1}) \tag{2.19}$$

These images are constructed using the shifted image P_2 as a reference for P_1 and vice versa. The cross-section σ is determined by performing a spatial integral. This integral is given by

$$2\sigma = \int_A A_i(P_1)\Delta_1 dA + \int_A A_i(P_2)\Delta_2 dA \tag{2.20}$$

where $A_i(P_{1,2})$ represent circular areas centered at $P_{1,2}$, respectively. These areas have a radius $r_i \approx \frac{3\lambda}{2NA}$,(where λ is the wavelength of the applied light and NA is the numerical aperture of the objective lens) which is approximately located in the second Airy ring of the objective

point-spread function (PSF). An average over a number of individual images acquisitions was taken for these two positions to minimise the shot noise and increase the sensitivity. The shifting referencing method is a highly efficient method for subtracting the local background and enhancing the signal-to-noise ratio. Essentially, if we assume that there are no significant changes in the background surrounding a particle, the local background's effect on σ is equally strong but with opposite sign in $\Delta 1$ and $\Delta 2$, resulting in its cancellation when the two are added together. Furthermore, taking the average of two measurements that are independent of each other decreases the level of noise by a factor of $\sqrt{2}$. The quick temporal referencing prevents the impact of gradual drift in the setup for more details about the shifting method check the [109]. For the collected data, the stage-camera system was consistently triggered with one trigger occurring approximately every $\tau = 10$ ms , resulting in the camera capturing a single acquisition with each trigger. The exposure time τ_e is equal to $\tau_e = \tau - 2$ ms. The precise exposure duration values utilised are dependent upon the wavelength and polariser; they will be indicated in the results (Chapters 3, 4, and 5). At a specific stage position, 128 frames are captured and then averaged in real time using software. The resulting average is then saved. Subsequently, the stage undergoes a change in position, and additional frames are collected. The process is iterated 20 times, yielding a total of 20 images, with 10 images for each position, which are then stored for subsequent processing. Significantly, in the course of this acquisition, the sample has the potential to move horizontally, with a drift of several micrometres per hour. Therefore, an in-house registration software was used to correct for this drift. In addition, software provides an automated analysis of the contrast images and corresponding particle cross-sections for datasets with hundreds of particles. Notably, the sensitivity of this technique is highly dependent on the sample surface cleanliness. The glass surface should be very clean; otherwise, any dielectric debries will cause an unwanted scattering background. In addition to the radial polariser, six differing filters were applied to each field of view to collect the data, which included results from a linear polariser. Four different angles (0, 45, 90, and 135)° were utilized for taking the linear polarisation images in order to determine the extinction cross-section area for different size and shape of AgNPLs. Any acquired images must include background images for this procedure where the background images were captured by blocking the illumination rather than turning off the lamp to prevent illumination intensity fluctuations/drifts upon turning the lamp on and off.

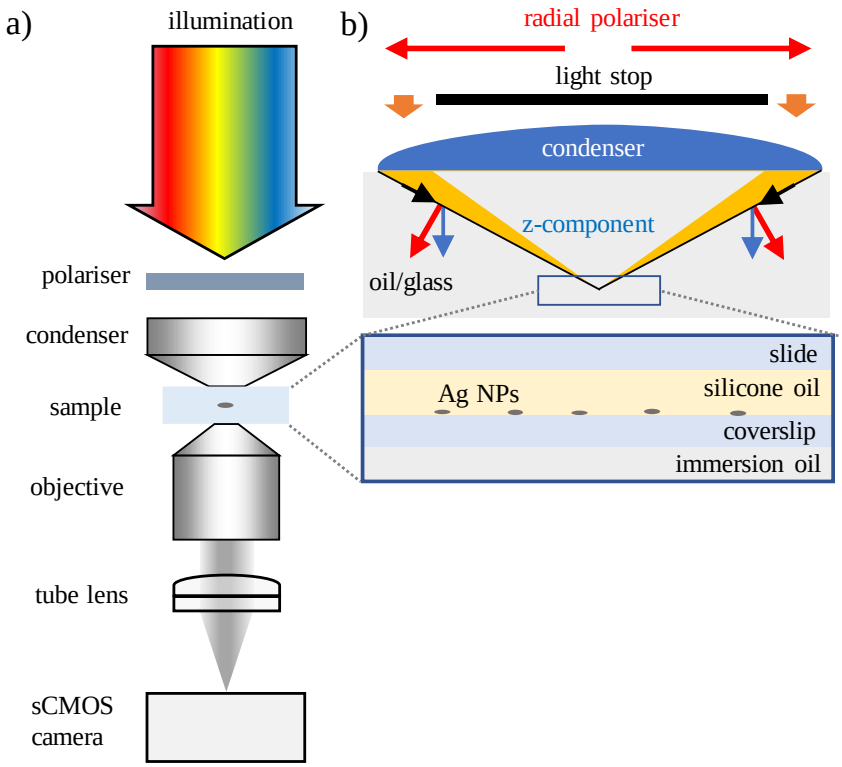

Figure 2.11: Illustration of the microscope configuration and the sample under investigation. a) The sample is illuminated with Köhler illumination, which allows for the selection of different wavelengths. The image of the sample is then captured by a camera, employing a condenser with a numerical aperture (NA) of 1.34 and an objective with a NA of 1.45. b) The lighting employs either a rotatable linear polariser or a radial polariser with a light stop positioned in the back focal plane of the condenser. The radial polariser generates a significant axial polarisation component in the focal plane. The sample consists of discrete silver nanoplates attached to a glass coverslip, surrounded by silicone oil that matches the refractive index of glass.

2.4.5 Optical extinction analysis

The extinction microscopy technique is able to provide us with images containing data for several hundred particles. The process of manually analysing that amount of data is time-consuming, and laborious; therefore, a programme for automated data analysis was designed and developed by Dr.Lukas Payne. The programme called Extinction Suite (ES). This software is extensively employed and can be applied to any kind of NPs and any microscope containing a camera where the analysis plugin has been designed in a simplified manner and is widely applicable experimentally as an analytical assistant. Imagej's macro language was used to create the ES, where Imagej is a highly effective, free-to-download, image manipulation and analysis programme offering a user-friendly interface and a variety of image manipulation, analysis and

measurement tools. The ES software includes a registration that was developed, utilising pattern recognition, to monitor the particles and adjust the frames accordingly. Figure 2.12 displays

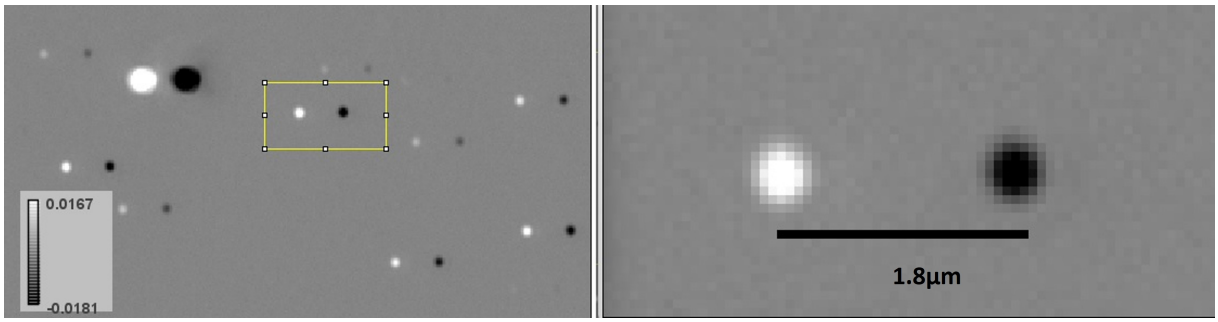

Figure 2.12: Part of the Field of view of extinction image of AgNPLs of 40nm diameter utilising a 100X, 1.45 NA oil objective,and a PCOs camera, the calibration bar represent the gray scale min=-0.018,max=0.0167. The right image is a magnification region denoted by a yellow selecting frame.

an illustrative Δ_1 extinction image of a portion of a single field of view. The separation of the bright-dark spot pairs, which is 1.8 µm, is clearly visible. Additionally, there is a high signal-to-noise ratio of approximately 100 for the strongest signals, with roughly 5% extinction seen. The measured particle density is consistent with the average distance of 6 µm between nanoparticles, as determined from the preparation technique.

In this section, how to analyse the data by using the ES programme shall be explained. Firstly, the extinction cross-section can be calculated as stated in equations 2.18 and 2.20. These equations show us how to go from what we measured, which is the intensity represented by images, to a physical quantity, the extinction cross-section with a value and unit. Alpha (α), an additional important parameter, is calculated with the ES from data. This parameter is related to the particle's shape in relation to the linear polariser's angle, hence the in-plane polarisation direction of the illumination. It refers to the ability of a particle to absorb and scatter light when illuminated by an external electric field with a linear polarisation direction. Four different angles of polarised light were used to illuminate the sample in order to obtain an understanding of the particle's shapes. The experimental data are fitted with the function

$$\sigma(\theta) = \sigma_0 \left(1 + \alpha \cos\left(2(\theta - \theta_0)\right)\right) \tag{2.21}$$

where σ_0 polaraisation average cross section σ, $\alpha \geq$ and the angular offset is related to the direction of the NPL asymmetry is $0 \geq \theta_0 \geq \pi$. From knowing σ_{ext} and α, it is possible to infer information on the shape and size of nanoparticles. As shown in Fig. 2.13 ES is comprised of four primary modules, of which two were utilised in our data analysis, namely the extinction analysis and particle analysis. The input format, selected mode, and experimental type determined the options available for each mode. For broad applicability, the ES accepts a variety of image input formats. When more than one form of data is collected for the same field of view (FOV), ES makes data analysis simple by providing the user with multiple experimental options; for example, one can analyse the extinction and dark field measurements together.

The process of determining the r_i is not arbitrary, so it is important to take a sufficient distance between the two positions of the particles during the measurement larger than $2\mathrm{r_i}$ so the PSF are well separated (see Fig. 2.14).

A challenging aspect of the software is specifying the conditions needed to identify the positions of the nanoparticles in the image, based on their brightness, which can be done by selecting the "find maxima" option. The aim is to determine where the bright peaks representing

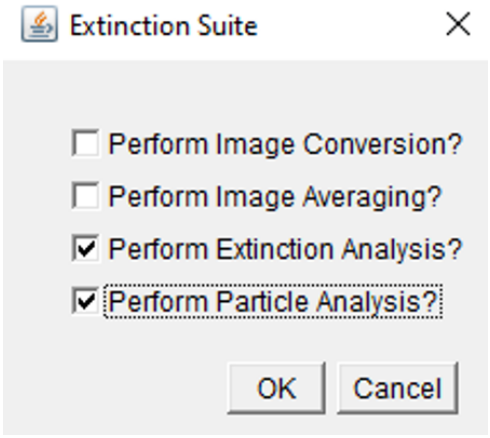

Figure 2.13: Extinction suite interface

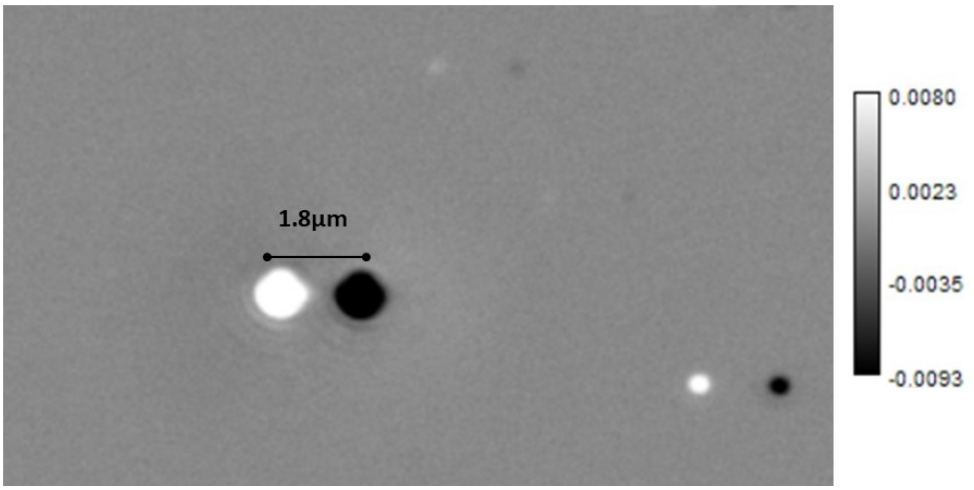

Figure 2.14: The zoomed-in image of the FOV region: the image revealed large particles separated with a sufficient distance between the signal and reference positions to avoid overlapping (Greyscale minimum = -0.0093, maximum = 0.0080)

.

useful nanoparticles are in the image , while avoiding to be affected by background and/or noise, resulting in "false positive" nanoparticle attributions. To that end, to software allows the user to enter a value called "noise tolerance" that must be precisely adjusted to find an acceptable balance to include all particles instead of noise and background. The registration step follows the selection of the noise tolerance value, and is used to locate and register the particle image peaks.

The images might represent the average of a number of takes captured within a time interval. Averaging over a number of acquisitions reduces image noise by a factor of $1/\sqrt{N}$, where N is the total takes of images averaged which is 128 in our work. Moreover, for the analysis process, The number of repetitions at each position is also a required parameter in software. As well as providing the value of the extinction cross-section for each nanoparticle, the ES software also evaluates the uncertainty due to the photon shot-noise in the image. To achieve this, ES fits the experimental data using the equation 2.21, and then refits the data, allowing each point to vary with the noise, and this process is repeated many times in order to determine

the standard deviation of the fitted parameter and assess the precision that could be obtained for σ_{ext} and α. Moreover, the ES provides the overview of the obtained cross-section values as an histogram for all particles analyzed, see example in Fig. 2.15. ES also provides a measure of the background and noise in the data, by calculating the cross-section on randomly selected positions where there are no particles. The resulting histogram is shown colored in gray in the example in Fig. 2.15. The center position of this gray histogram provides the background and its standard deviation is a measured of the noise. Notably, from the measured noise, one can infer which part of the measured statistical distribution comes from particle size/shape heterogeneity, by subtracting the noise contribution. This is shown in Fig. 2.15, where "sample standard deviation with noise" refers to the measured sample distribution, while "sample standard deviation without noise" refers to the contribution calculated by subtracting the effect of the noise, as discussed in Ref [101]. The Extinction Suite software can be accessed at the following URL: https://langsrv.astro.cf.ac.uk/Crosssection/Crosssection.html For further information, please refer to the provided references [101] and [109].

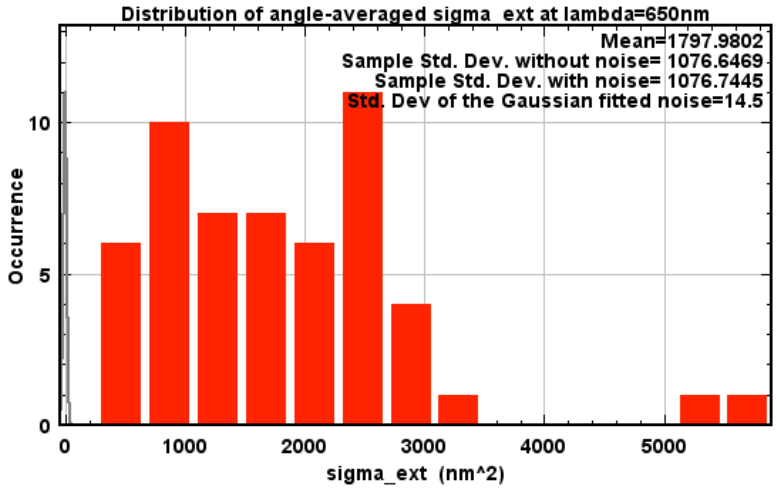

Figure 2.15: Histogram of the polarisation averaged extinction cross-section, measured over many nanoparticles at 650nm wavelength for PVP-AgNPLs with 40nm size. The red bars show the histogram of σ_{ext} for the nanoparticles, while the gray histogram is the distribution measured in regions of the sample without nanoparticles (NPs), hence representing the background and noise in the data. The gray histogram is centered around zero, indicating that there is no background, and has a standard deviation of 14.5 nm^2 representing the noise in the data. The distribution of cross-sections for the particles has a mean of 1797.98 nm^2, as indicated, and a standard deviation of 1076.74 nm^2. This is dominated by the particle size/shape distribution. The standard deviation calculated after subtracting the contribution from the noise is indicated as the "sample standard deviation without noise", see Ref[101].

2.4.6 AFM characterisation for PVP-AgNPLs

Atomic force microscopy (AFM) is a versatile technique for micro/nanostructured surface analysis, producing high-resolution topographic images in air or liquid environments. It can image various surfaces, including glass, ceramics, composites, polymers, and biological samples. AFM provides qualitative and quantitative data on physical properties, as well as statistical information. It can characterize a broad spectrum of particulate sizes in a single scan. AFM microscopes use a micromachined silicon probe with a sharp edge to acquire images. There are three main imaging modes: contact dc mode, ac mode (tapping and non-contact), and deflection mode [119].

A Bruker Dimension Icon atomic force microscope was utilised to examine the surfaces of glass coverslips that contained PVP-AgNPLs following the wet-casting and drying step in the sample preparation (section 2.3.2). To image the samples, an automatic peak force tapping mode was used. We employed a silicon nitride tip (ScanAsyst-Air, Bruker) with a tip diameter of 4nm and facet angles ranging from 15 to 25 degrees relative to the vertical direction. During peak force tapping mode, the z-piezo on the scanner head adjusts the frequency of modulation to 2 kHz and the amplitude to 150 nm for each pixel in the image. This causes the probe tip to intermittently make contact with the substrate, creating a fast force curve that takes around 15 ms per point. The highest value acquired from each force curve functions as a feedback signal for the imaging procedure. The measurements were made in ambient air conditions. The typical images are captured using a square region with a length of 250 to 400 nm. The imaging process involves 128 point per line. The obtained results will be presented and discussed in Chapter 5. I express my gratitude to Vikramdeep Singh for providing me with guidance and instruction in operating the AFM instrument.

2.4.7 TEM characterisation for AgNPLs

In addition to the TEM characterization provided by the manufacturer, TEM was carried out in house using the EM facility available at Cardiff University. Wet samples were distributed onto 300 mesh Cu holey carbon film grids. Blotting was used to sequentially add 6 μL drops of the stock solution until an appropriate coverage was achieved. A transmission electron microscope (JEOL JEM 2100) running at 200 kV was used for sample analysis. A TEM image overview with different scale in Fig. 2.16 and Fig. 2.17 depicts a typical TEM image. As evidenced by the TEM images of PVP-AgNPLs and SiO_2-AgNPLs, both AgNPLs plates have spherical, triangular, hexagonal, and rod morphologies of various sizes and shapes. As evidenced by the TEM images of PVP-AgNPLs and SiO_2-AgNPLs, both types of AgNPLs exhibit spherical, triangular, hexagonal, and rod morphologies of various sizes and shapes. This observation agrees with the results provided by the manufacturer, which report a variability of (40 $\pm$ 10) nm in size and shapes similar to those shown in Fig. 2.1, Fig. 2.3.

Furthermore, the time factor, specifically the shelf life of the nanoparticles, plays a critical role in their stability and performance. According to the manufacturer's specifications, the shelf life of the Ag NPs with PVP coating and a silica shell is approximately one year. In this study, TEM was performed within the first few months of sample preparation, well within the manufacturer-recommended shelf life. During this period, the nanoparticles exhibited stability, with no noticeable aggregation or significant changes in morphology.

This suggests that, within the early stages of their lifespan, the nanoparticles retained their intended properties, which is essential for reproducibility and accuracy in experiments. However, it is worth noting that as the nanoparticles approach the end of their shelf life, factors such as aggregation, changes in size distribution, and optical properties may begin to compromise their stability. This will be important to monitor in future long-term studies.

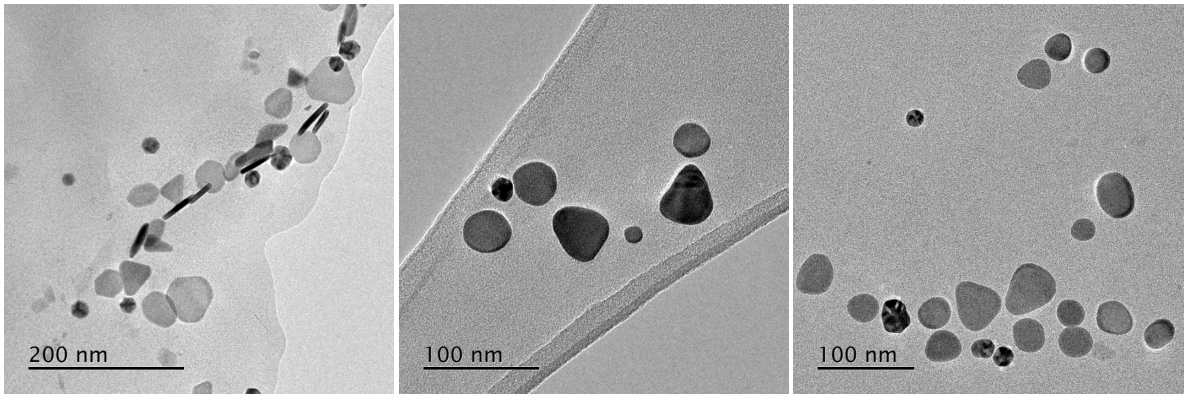

Figure 2.16: TEM images for PVP-AgNPLs. TEM images of PVP-AgNPLs used in this work at different magnification showing the variety of shapes and sizes.

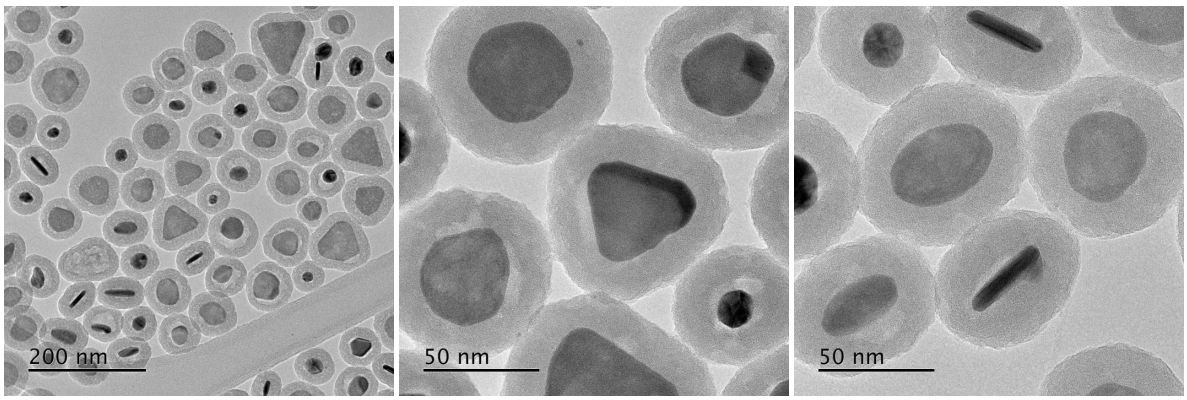

Figure 2.17: TEM images for SiO_2-AgNPLs. TEM images of SiO_2-AgNPLs used in this work at different magnification showing the variety of shapes and sizes.

Chapter 3

Polarisation resolved optical extinction

As introduced in Chapter 1, metallic nanoparticles produce morphology-dependent localized surface plasmon resonances (LSPR) that couple to light, and appear as amplitude peaks of the optical absorption and scattering spectra at the LSPR frequency [120]. Gold and silver nanoparticles, have plasmonic characteristics in the visible wavelength range, hence useful for optical applications. The ability to control the size and shape of these metal nanostructures enables the manipulation of their LSPR and their sensitivity to the surrounding environment [121]. Gold nanoparticles are biocompatible and chemically stable, while silver nanoparticles have better optical qualities, such as stronger and sharper LSPR resonances, because silver has smaller imaginary component of the permittivity related to its lower non-radiative damping compared to gold [122]. In this Chapter, a novel implementation of the extinction microscopy technique is described and shown for gold and silver nanoparticles. Quantitative optical extinction microscopy is a powerful method to characterise the size and shape of individual metallic nanoparticles [109]. In this Chapter, quantitative optical extinction is shown using a new optical element that has been designed and installed in the light beam path, a radial polariser, to aid the morphometric characterisation of thin nanoplates. Detailed explanations on how the measurements were carried out will be provided, along with the challenges found during the measurements and how were they overcome. Notably, from the large number of the optical extinction data measured on hundreds of individual nanoparticles a cluster analysis was employed to categorize NPs into different groups that correspond to different particle morphologies.

3.1 Linear and radial polarisation

In the condition of linear polarisation, the electric field generated by light oscillates in a well-defined direction. If a nanoparticle possesses aÂ LSPRÂ mode with a well definedÂ polarisation direction, such as the longitudinal LSPR mode in a nanorod, altering the orientation of the particle in interaction with linearly polarised incident light will exhibit optical absorption and scatteringÂ controlled appropriately, with a maximum occurring when the particle is aligned such that the polarisation of LSPR aligns with that of light. This phenomena has been well examined [109]. For nanoparticles attached onto a surface, as well as considering polarisation directions oriented in the sample plane, it is useful to consider the axial polarisation direction perpendicular to plane, as this can provide complementary information on the nanoparticle thickness. To generate such polarisation component, one can introduce a high numerical aperture annular illumination pattern coupled with a radial polariser in the back focal plane of a microscope condenser lens used to focus light on the sample plane [123]. The radial polariser results in light

field is mostly orientated radially, nanoplate which is then converted into a significant axial component in the sample plane. This is what was used in our experiments, as described in Chapter 2, section 2.4.2. The optical extinction cross-section section was measured using the microscope set-up described in Chapter 2, section 2.4.1. A rotatable linear polariser as well as the radial polariser were utilised. In both cases, an illumination numerical aperture NA of 1.34 was used. With the linear polariser, four linear polarisation directions were applied, discribed by γ_P (0, 45, 90, and 135 degrees). With the radial polariser, a light stop was inserted to block the central part and obtain a 1 to 1.34 NA annular ring illumination generating a significant axial polarisation component. Individual silver nanoplates as well as nominally spherical gold nanoparticles were investigated. All the nanoparticle samples were deposited on a glass surface using the wet casting method as explained in section 2.3.2. For the silver nanoplates, two types were studied, namely PVP-coated (PVP-AgNPLs) and silica-coated (SiO2-AgNPLs). As discussed in section 2.4.7, these nanoparticles are specified by the manufacturer to be nominally of triangular shape with a 40 nm diameter and a 10 nm thickness, but in practice show a heterogeneous distribution of sizes and shapes, as confirmed by TEM examination. The ensemble optical absorbance spectra of the PVP-AgNPLs stock provided by the manufacturer (see Fig. 2.1) exhibits a main LSPR centred at 660nm wavelength with full-width at half maximum (FWHM) of 175nm. In addition, there is a peak at 340 nm and a less prominent band at 400-450 nm. Comparing with the literature [124][125], the primary LSPR peak can be attributed to an in-plane dipole mode, the 400-450 nm band to an in-plane quadrupole mode, and the 340 nm peak an out-of-plane dipole mode. The significant FWHM value of the main LSPR is in agreement with the size and shape distribution of these nanoplates, as the wavelength of the in-plane dipole resonance shifts towards longer wavelengths with larger triangle edge lengths and thinner plate thicknesses [126].

Optical extinction measurements were carried for different light wavelengths, using colour band pass filters in the illumination, as described in Chapter 2. A summary table giving exposure duration for each specific wavelength and polariser configuration utilised with PVP-AgNPLs is presented in Table 3.1.

Table 3.1: Exposure time in extinction microscopy for each wavelength and polariser condition used for PVP-AgNPLs.

λ (nm)	τ_e linear pol. (ms)	τ_e radial pol. (ms)
500	3.3	10.3
550	1.45	4.5
600	1.05	3.3
650	1.05	3.3
700	1.25	4.1
750	2.3	7.8

An illustration of the extinction image obtained from a specific field of view is presented in Fig. 3.1. For quantitative analysis, the shifted method with a sample displacement of 1.8 µm was used (see Chapter 2). Briefly two images were acquired, the first one at a given position and a second one at a shifted position, acting as reference transmission in the absence of a particle. As a result, a differential transmission image is generated, where each individual particle appears as a pair of bright and dark spots. From these images, a quantitative extinction cross section is measured, as an areal integral of the differential transmission image centred at a nanoparticle position (see Chapter 2 equations 2.20).

Fig. 3.2 displays the optical extinction cross-section spectra selected of individual nanopar-

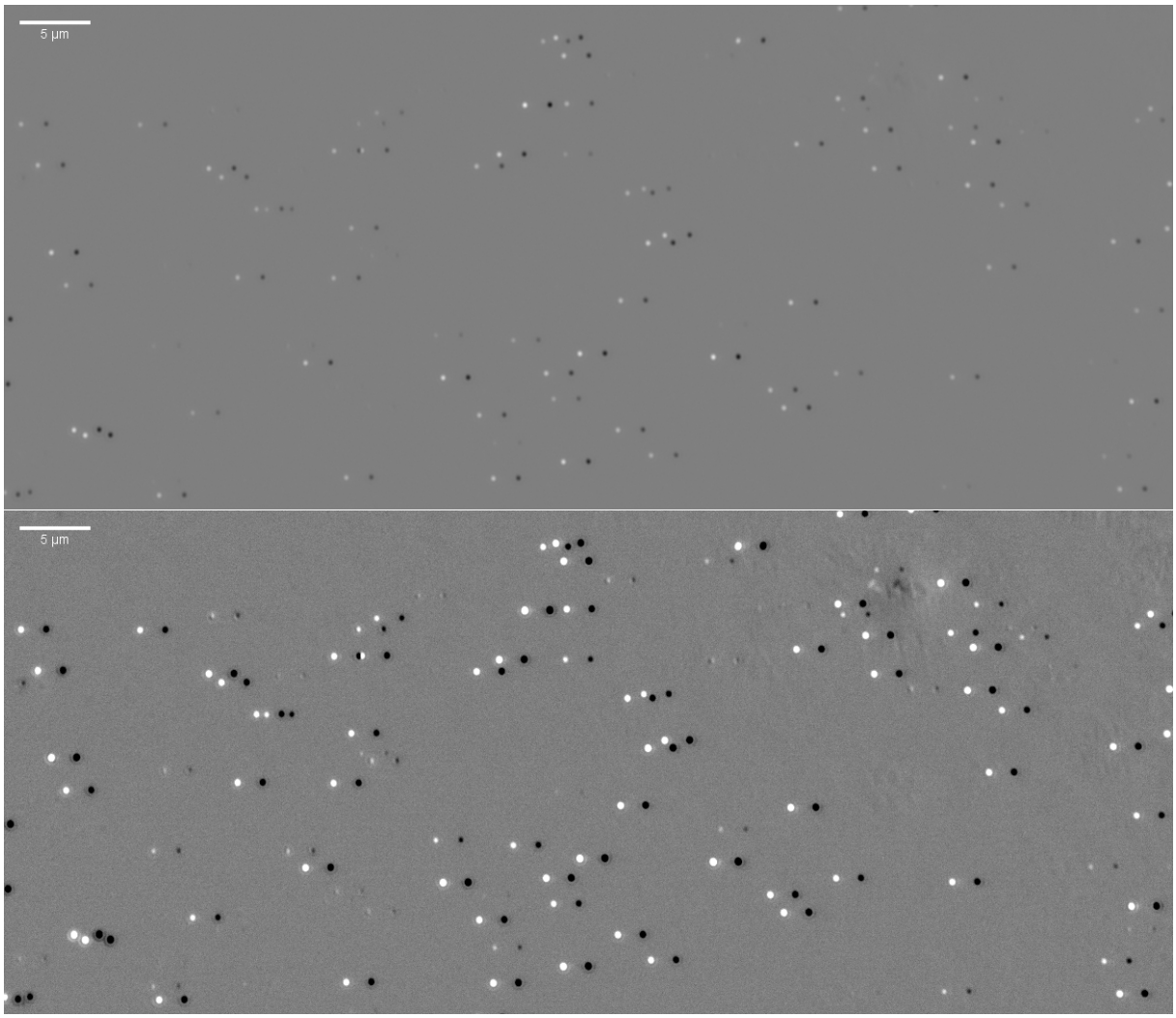

Figure 3.1: Example of extinction contrast Δ_1 for nominal 40nm PVP-AgNPLs. Linear polariser angle $\gamma_P = 0°$, and wavelength $\lambda = 650\,\text{nm}$. The image consists of 1256×540 pixels with pixel size of 65 nm. Both images are shown in greyscale, with the top one ranging from -0.05 to 0.05 and the bottom one from -0.005 to 0.005.

ticles as examples. The extinction contrast images, denoted as Δ_1, specific to a chosen AgNPL, are depicted in Fig. 3.2 (a) for both linear and radial polarisations. For this nanoparticle, the contrast is significantly reduced going from linear to radial polarisation. The spectra of σ for linear polarisation at four different γ_P, as well as for radial polarisation, are provided in Fig. 3.2 (b). From the measured polarisation dependence, this the nanoparticle exhibits a minor dipolar in-plane asymmetry, with no significant differences seen when changing γ_P. The main LSPR occurs around 650nm, and there is a drop in the magnitude of σ by more than a factor of 2 when utilizing the radial polariser. An example of different nanoparticle is shown in Fig. 3.2 (c). This nanoparticle has an LSPR in blue that clearly depends on γ_P, and its linear and radial values are about the same. The dependency on γ_P at $\lambda = 500$ nm is illustrated in the inset of Fig. 3.2(c). It is fitted using the function $\sigma_L(1 + \alpha\cos(2(\gamma_P - \gamma)))$. The fit parameters are provided, including errors that account for the measurement noise (see Chapter2 for additional information regarding the methodology employed to address measurement uncertainties, please refer to Refs [9] and [109]).

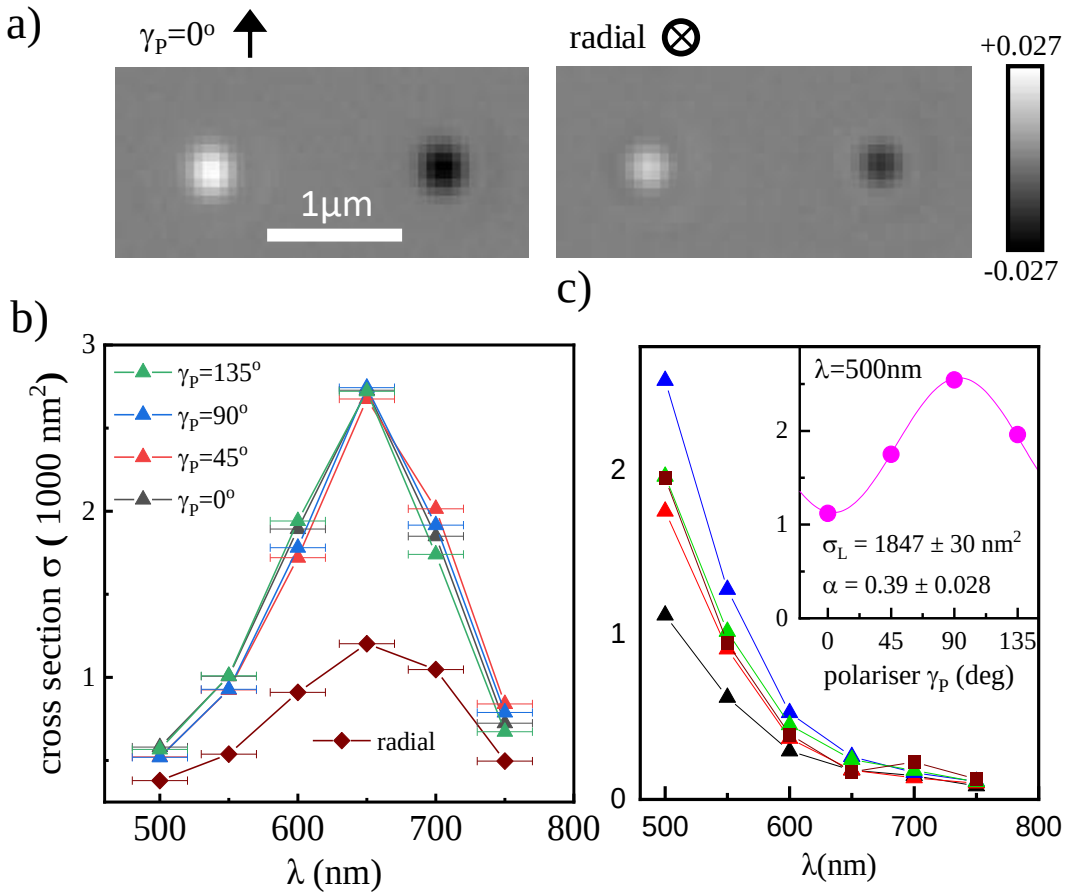

Figure 3.2: Linear and radial optical extinction cross-sections measured for different individual PVP-AgNPLs. (a) The optical extinction contrast image Δ_1 is obtained by imaging a specific individual PVP-AgNPL at a wavelength of 650nm using either a linear polariser at an angle $\gamma_P = 0°$ or a radial polariser.(b) The extinction cross-section spectra for the NP in (a) are measured at various linear polariser angles and with the radial polariser, as shown. (c) Cross-section extinction spectra, similar to those described in (b), but obtained for different PVP-AgNPL. The inset displays the cross-section at a wavelength of 500nm versus γ_P. A sinusoidal fit has been applied to the data, yielding the parameters. For experimental data, measured spectra in (b)(c), the lines are guides to the eye.

The observed distinctions arise from differences in the morphological characteristics of the two PVP-AgNPLs. The spectra depicted in Fig. 3.2 (b) indicate the presence of a small, thin, triangular nanoplate, while those in Fig. 3.2 (c) suggest a thicker spheroidal NP exhibiting in-plane dipolar asymmetry. Concerning the observed reduction in the magnitude of the cross-section from linear to radial polarisation illustrated in Fig. 3.2 (b), this can be understood by comparison with numerical simulations in the literature [125]. These indicate that the absorption cross-section spectrum of a thin nanoplate within the wavelength range corresponding to the primary dipole LSPR mode is negligible when exposed to axially polarised light. In the experimental setup, the relative intensity of the illumination components on the sample was determined, distinguishing between in-plane ($I_{\parallel}$, $I_{\perp}$) and axial (I_z) polarization, as discussed in Ref [9]. Utilizing the linear polariser and a NA ranging from 0 to 1.34, its found that $I_{\parallel,L} = 0.825$, $I_{\perp,L} = 0.007$, and $I_{z,L} = 0.168$, where $\parallel$ indicates the direction along the polariser axis, and $\perp$ is orthogonal to it. Conversely, employing a radial polariser and annular illumination within the NA range of 1.00 to 1.34, the values $I_{\parallel,R} = I_{\perp,R} = 0.209$ and $I_{z,R} = 0.582$ were obtained [127].

This results in a correction factor of approximately 1.25 for measured optical cross-sections within the range of 0 to 1.34 NA and about 1.6 for the range of 1.00 to 1.34 NA. Consequently, the ratio of measured σ_R to σ_L incorporates a factor of 1.28. Fig. 3.2 (b) shows that when a radial polariser is used, the cross-sectional area (σ) at the LSPR peak wavelength ($\lambda = 650$ nm) reduced to approximately 44% relative to the value using of a linear polariser. This reduction is consistent with having a thin nanoplate that is flat on the substrate, hence almost no extinction at the LSPR for axial polarisation, and taking into account the in-plane illumination components that are present when measuring σ_R and σ_L . Conversely, for the NP shown in Fig. 3.2 (c), the cross-section magnitude under radial and linear polarisations appear similar. This similarity suggests the presence of a spheroidal NP with comparable dimensions in both axial and in-plane orientations. To obtain a statistically relevant overview, multiple sample areas were examined, resulting in a total of 219 individual NPs being evaluated. A variety of behaviours were seen, consistent with the wide range of shapes and dimensions observed in the sample by TEM.

The plot in Figure 3.3 gives an overview of the results for these 219 nanoparticles. 3.3 (a) illustrates the relationship between σ_R and σ_L, which provides an indication of the axial to in-plane shape aspect ratio, as discussed previously. More precisely, spheres would have a value of σ_R equal to σ_L (shown by the solid line), while flat lying plates would have a value of σ_R smaller than σ_L (represented by the dashed line showing $\sigma_R = 0.5\sigma_L$). Fig. 3.3 (b) illustrates the relationship between the values of α and σ_L. This an indicator of an in-plane shape asymmetry, where symmetric equilateral-triangular or hexagonal plates exhibit $\alpha = 0$, while flat-lying elongated rods display α values up to 1. The findings indicate a range of behaviours, consistent with the various shapes and sizes present in the sample. Notably, numerous NPs exhibit $\sigma_R < \sigma_L$ at a wavelength of 700 nm, suggesting that they are thin plates. Although the values of α exhibit considerable variation, plates with significant σ_L at 700 nm generally correspond to small α values (< 0.4). This implies a prevalent presence of nanoplates with approximately 3-fold rotation symmetry in-plane, characterized by flat-lying triangles, hexagons, or disks.

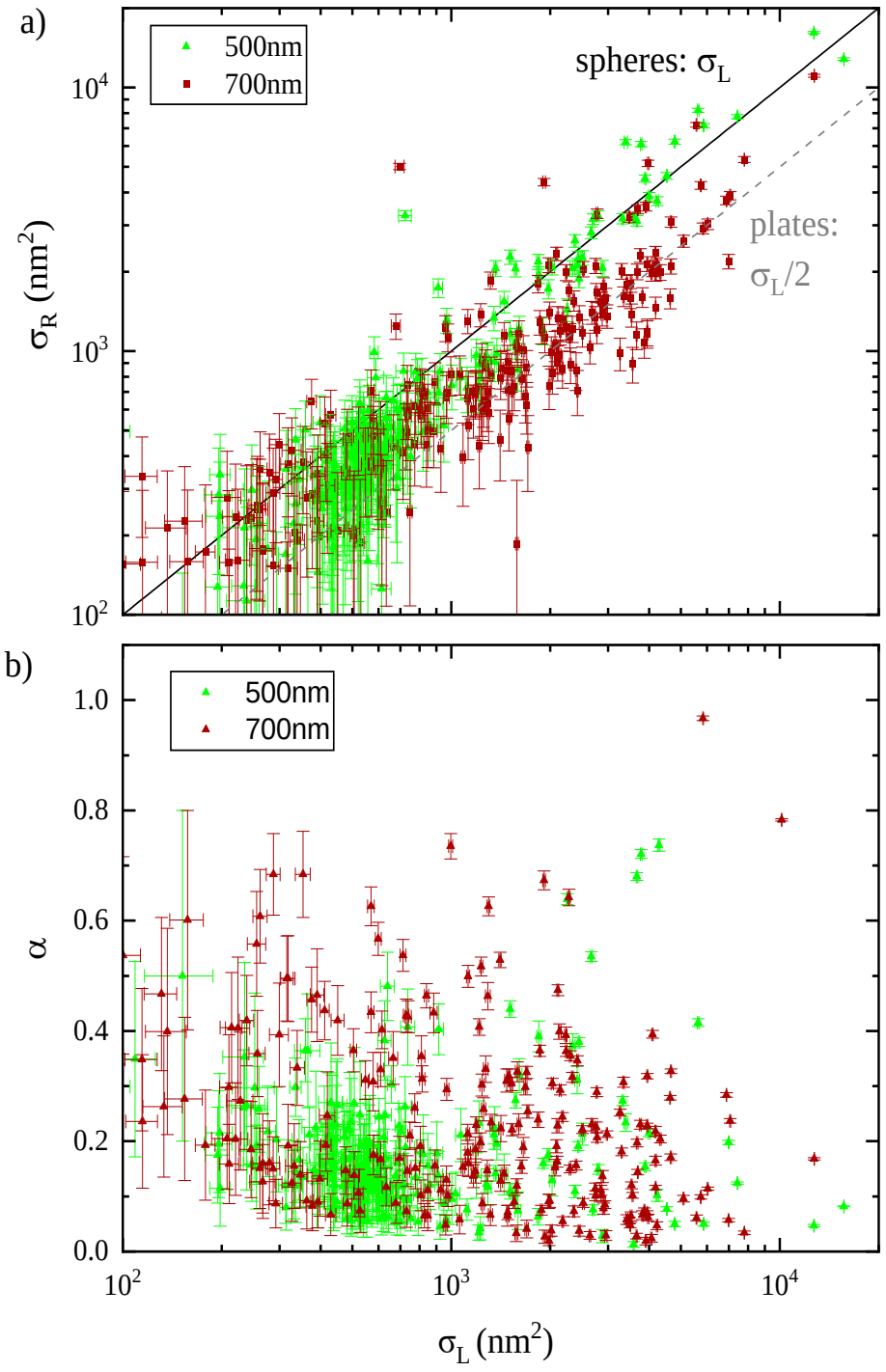

Figure 3.3: Summary of extinction cross-section values for 219 individual nominal 40nm PVP-AgNPLs. The values obtained with the radial polariser are denoted as σ_R, whereas the values obtained with the linear polariser are represented by the fit parameters σ_L and α. a) Comparison between σ_R and σ_L. The expected values of σ_L for spherical particles and $0.5\sigma_L$ for plates are displayed lines. b) Comparison between α and σ_L. Green symbols correspond to a wavelength of 500 nm, whereas red symbols correspond to a wavelength of 700 nm. Error bars represent the level of uncertainty resulting from shot noise in the measurements.

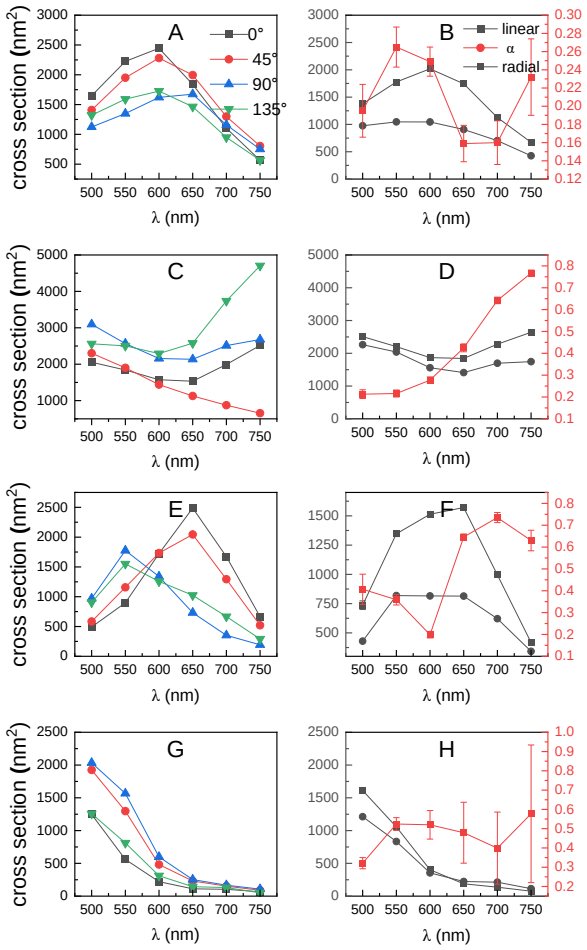

Figure 3.4: Optical extinction cross-sections measured on four different individual PVP-AgNPLs: The left column represents the linear σ_L at (0, 45, 90, and 135)°polarisation for four different AgNPLs of nominal 40nm size and 10 nm thickness with six different wavelengths. The right column shows the relative amplitudes (α), the avarage linear σ_L and the radial σ_R for the same PVP-AgNPLs in the left column.

Fig. 3.4 displays the extinction cross-section for linear and radial polarisation at different wavelengths, for four distinct nanoparticles, to further exemplify the range of observed behaviours in specific cases. The left column exhibits the polarisation dependence at four polarisation angles, offering valuable insights about the shape of the nanoparticles. In Fig. 3.4 (G)(H) the nanoparticle exhibits a blue LSPR, and a cross-section magnitude that changes with γ_P. Furthermore, both its linear and radial cross-section values are about equal. This behaviour is similar to the particle shown in Fig. 3.2 (C), attributed to a thick spheroid with some in-plane asymmetry. Conversely, for both particles in Fig. 3.4 (A)(B) and (E)(F), there are two resonance peaks, exhibiting a polarisation dependence and a clear difference between the linear and radial cross section magnitude. These are therefore thin plates, however not fully triangularly symmetric in plane, for example slightly elongated hexagons. The particle in Fig. 3.4 (C)(D) has a resonance in the red (>750nm range) with a strong polarisation dependence, hence is likely an elongated nanorod, with some thickness as shown by the similar magnitude of the linear and

radial cross-sections.

3.1.1 Optical extinction measurements of individual SiO_2-AgNPLs

The manufacturer specifications for the investigated SiO_2-AgNPLs, indicate a variety of sizes and shapes. Fig. 2.3 shows the stock ensemble optical absorbance spectrum of the SiO_2-AgNPLs which reveals a main LSPR at 657nm with 153 nm FWHM, a weaker band between 340-500 nm, and weaker peak at 334 nm. The same procedures illustrated in section 3.1 have been employed using slightly different measurement times, as summarised in the table 3.2. For these particles, the radial polariser was used however, without the incorporation of the light stop, hence the illumination covered the full 0-1.34NA range. In this case, the illumination components were calculated to be $I_{\parallel,R} = I_{\perp,R} = 0.333$, $I_{z,R} = 0.334$. In Fig. 3.5 left column represents linear σ_{L}

Table 3.2: Exposure time in extinction microscopy for each wavelength and polariser condition used for SiO_2-AgNPLs.

λ (nm)	τ_{e} linear pol. (ms)	τ_{e} radial pol. (ms)
500	8.5	8.5
550	3.5	3.5
600	2.4	2.4
650	2.3	2.3
700	2.8	2.8
750	5	5

at (0, 45, 90, and 135)°polarisation angles for five selected SiO_2-AgNPLs of nominal 40nm size and 10 nm thickness with six different wavelengths. Clear changes are observed, for instance in Fig. 3.5 (C) it is evident that the magnitude of σ_{L} at 90°, and 135°is nearly double the value of σ_{L} at 0°, and 45°. The figures shown in the right column illustrate the polarisation average σ_{L} and radial σ_{R} values with varying wavelengths, which exhibit a high degree of similarity. The observed behaviour may be explained due to the presence of a thick silica-coated shell around the Ag-NPLs, which hinders them from assuming a flat orientation. Consequently, when NPs are not lying flat, due to their thick shell, their vertical orientation may introduce an increase in the measured σ_{R} . To that end, as will be discussed in a later section, different combinations of the measured σ_{L} and σ_{R} values have been used to obtain signatures of particle morphologies when analysing the SiO2-AgNPLs compared to the PVP-AgNPLs.

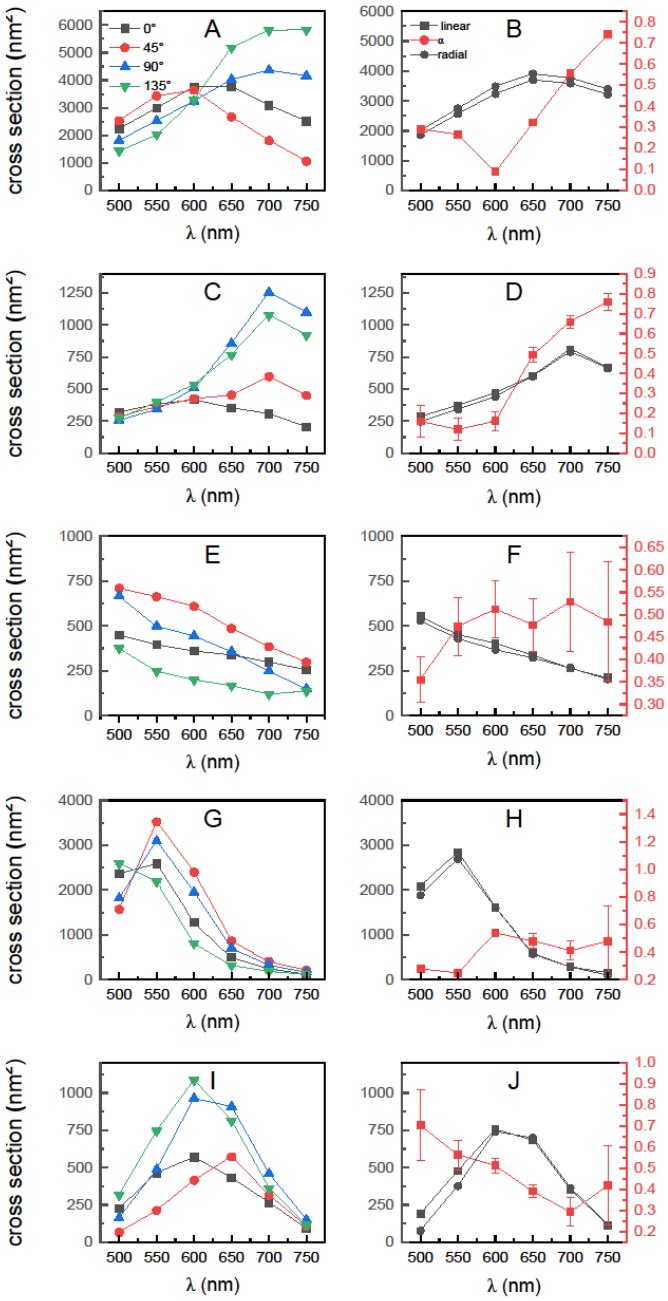

Figure 3.5: Optical extinction cross-sections measured on five different individual SiO_2-AgNPLs: The left column represents σ_L measured at (0, 45, 90, and 135)°polarisation angles for five selected SiO_2-AgNPLs of nominal 40nm size and 10 nm thickness with six different wavelengths. The right column shows the relative amplitudes (α), the polarisation average σ_L and the radial σ_R for the same SiO_2-AgNPLs in the left column.

The plot in Fig. 3.6 provides a summary of the results obtained for these SiO_2-AgNPLs, over a total of 377 measured particles (similar to the overview in Fig.3.3 for the PVP-coated particles). Fig. 3.6 (a) shows the correlation between σ_R and σ_L. As discussed for Fig. 3.3, this correlation serves as an indicator of the axial versus in-plane shapes, where, spheres would exhibit a value of σ_R that is equal to σ_L (as indicated by the solid line), whereas flat lying

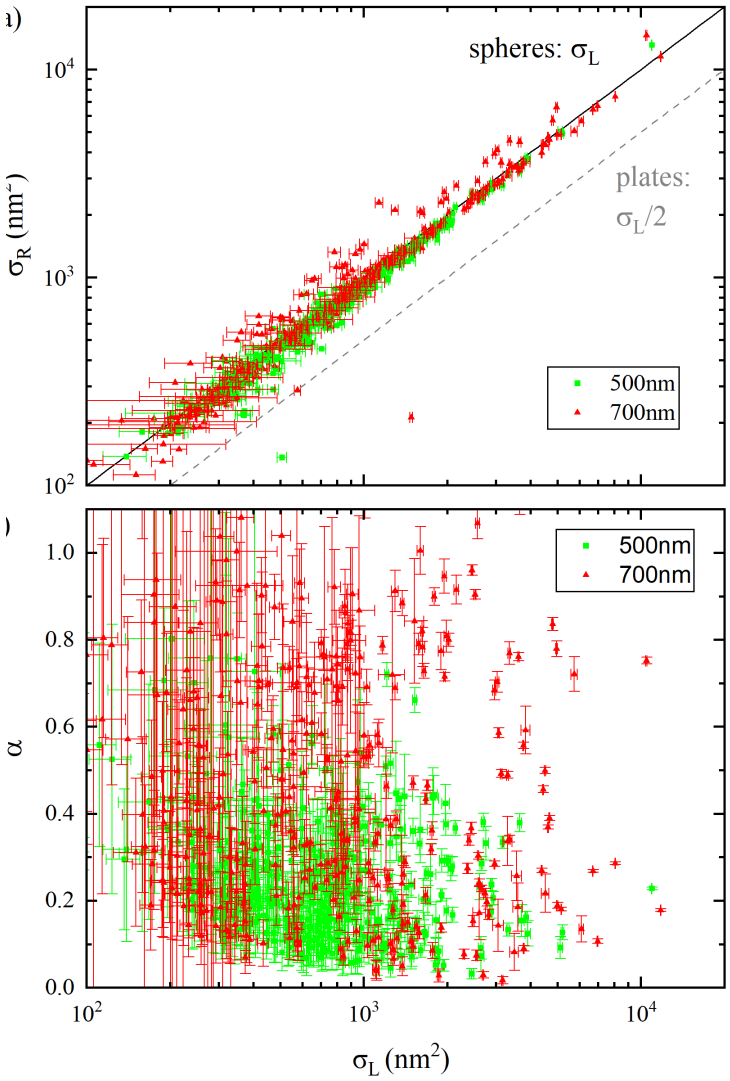

Figure 3.6: Summary of extinction cross-section values for 377 individual SiO_2-AgNPLs. The values obtained with the radial polariser are denoted as σ_R, whereas the values obtained with the linear polariser are represented by the fit parameters σ_L and α. a) Comparison between σ_R and σ_L. The expected values of σ_L for spherical particles and $0.5\sigma_L$ for plates are displayed for comparison. b) Comparison between α and σ_L. Green symbols correspond to a wavelength of 500 nm, whereas red symbols correspond to a wavelength of 700 nm. Error bars represent the level of uncertainty resulting from shot noise in the measurements.

plates would have a smaller value of σ_R compared to σ_L (represented by the dashed line). This overview suggests that the majority of these AgNPLs did not lie flat due to the presence of a thick silica shell. Therefore, new sets of measurements were conducted for this particular type of AgNPLs, where the motion of particles is described by rotational and translational dynamics

associated with Brownian diffusion in the viscous medium, as described in Chapter4.

3.1.2 Optical Measurement of Au NPs

Spherical gold nanoparticles with a diameter of 30 nm were used for comparison, serving as a benchmark for the optical extinction method against particles with a well-defined size and shape. These gold nanoparticles are marketed as "ultra-uniform" by the manufacturer and exhibit a very narrow size and shape distribution of 30 ± 3 nm (see Fig. **??**). Given that spherical particles exhibit isotropic optical properties, this experiment aimed to verify whether the measured extinction cross-section would remain independent of the chosen polariser configuration. Particular attention was given to comparing the results obtained using linear and radial polarisers. . Section 2.3.2 provides an in-depth description of the sample preparation process. The processes described in Section 3.1 have been applied using the measurement exposure times shown in Table 3.3. For these measurement, the radial polariser was employed without the light-stop (as discussed for the silica-coated AgNPLs in the previous section). As discussed extensively in the literature, changes in AuNP size affect the magnitude of the extinction cross-section [101][109]. Generally larger nanoparticles higher extinction cross-sections than smaller ones, with a scaling law $\sigma_{\text{abs}} \sim r^3$ and $\sigma_{\text{sca}} \sim r^6$ for a particle radius r in the wavelength limit of $\lambda \gg r$ (Rayleigh limit). Depending on the medium dielectric constant, 30 nm diameter gold nanoparticles have an extinction cross section peak ranging between 510 and 550 nm going from air (n=1) to n=1.5 refractive index [128]. Fig. 3.7, provides an example of the measured polarisation dependence for the extinction cross-section of a selected 30 nm Au NP across six distinct wavelengths. Since these particles were embedded in silicon oil (n=1.52), they exhibit a maximum extinction cross-section magnitude at 550 nm wavelength, as expected. The measured cross-section exhibits no dependence on light polarisation direction, consistent with the TEM results in Fig. 2.4, showing the uniform spherical shape of these nanoparticles. Conversely, in silver nanoparticles, variations in shape lead to distinct polarisation dependencies, as discussed in the previous sections. In the right column of Fig. 3.7, The wavelength dependence of σ_L measured for four polarisation angles is shown. In the left column, corresponding to the same particle, the polarisation-average cross-section σ_L, the radial cross-section σ_R, and α are provided. As expected for spherical particles, σ_L and σ_R are very similar, and $\alpha \sim 0$.

Table 3.3: Exposure time in extinction microscopy for each wavelength and polariser condition used for Au NPs.

λ (nm)	τ_e linear pol. (ms)	τ_e radial pol. (ms)
450	11.4	11.4
500	3.25	3.25
550	1.4	1.4
600	1	1
650	1	1
700	1.2	1.2

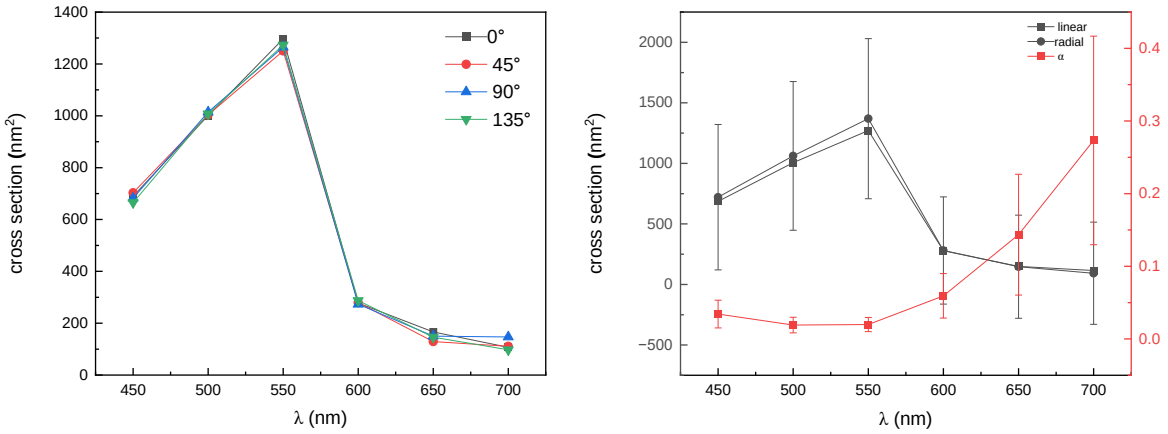

Figure 3.7: Optical extinction cross-sections measured on a selected individual spherical AuNP. The left column represents σ_L measured at (0, 45, 90, and 135)°polarisation angles for a AuNP of nominal 30nm size with six different wavelengths. The right column shows the amplitude (α), the polarisation averaged σ_L and the radial σ_{R} for the same AuNP in the left column.

3.2 PVP-AgNPLs cluster analyses

A method of unsupervised cluster analysis to categorize NPs based on their particle morphologies has been developed and implemented by Dr. Francesco Masia. This method is used to sort the large amount of nanoparticles investigated into sub-groups, to help characterising and quantifying their size/shape heterogeneity. In the context of this analysis, each individual NP is characterized by 18 predictors derived from the wavelength resolved values of $\tilde{\sigma}_{\mathrm{L}}$, $2\alpha\tilde{\sigma}_{\mathrm{L}}$ and $\tilde{\sigma}_{\mathrm{R}}$. Here $\tilde{\sigma}_{\mathrm{L}}$ and $\tilde{\sigma}_{\mathrm{R}}$ represent cross-section values for the linear and radial polarisations, normalised to the mean cross section $\bar{\sigma}$ averaged across all wavelengths and polarisations. This normalization process effectively eliminates the inherent influence of absolute cross-sectional information, predominantly related to the particle size rather than shape. A hierarchical cluster analysis (HCA) was carried out utilising a cosine metric and average linkage. To eliminate outliers, the NPs that create individual groups for HCA utilizing fewer than 9 clusters were also removed. When using the cosine metrics, these were 3 NPs for average linkage (4 when excluding $\tilde{\sigma}_{\mathrm{R}}$), 2 for complete linkage and 6 for single linkage. For euclidean metrics these were 6 NPs for average linkage and 4 for complete linkage. The results for 9 groups are shown in Fig. 3.8. These groups separate nanoplates having different LSPR wavelength ranges. A principal component analysis (PCA) of the predictors, showing the first two components over the NP ensemble, is displayed in Fig. 3.8 (a), with colours separating the nine groups. The dendrogram corresponding to this analysis is displayed in Fig. 3.11 Additionally, a histogram illustrating the distribution of the mean $\bar{\sigma}$ with in each group is presented in Fig. 3.9. The cluster analysis separate the NPs into adjacent regions in Fig. 3.9, showing a rather continuous spread of shape. Note that

the groups partially overlap when eliminating the radial polariser data in the PCA (see Fig. 3.8 (b)). Additionally, when repeating the HCA without the radial polariser data, there is a less effective separation of the plate-like NPs (see Fig. 3.13). These findings highlight the importance of measuring σ_R in order to distinguish plate-like nanoparticles. Moreover, adding the measured cross-section's magnitude as a predictor does not increase the groups' separation [123]. The average spectra of the predictors for each group, as shown in Fig. 3.8 (c), exhibit various features that reflect the corresponding properties of NPs. Groups 2, 1, and 7 have a prominent $\tilde{\sigma}_{\mathrm{L}}$, accompanied by a minor α_{L} value of approximately 0.2 and a $\tilde{\sigma}_{\mathrm{R}}$ value that is half of $\tilde{\sigma}_{\mathrm{L}}$. These results suggest the presence of nanoplates that are lying flat. The distinguishing factor among these groups is the LSPR wavelength, moving from a $> 750\,\mathrm{nm}$ in cluster 2 to 670 nm in group 1, and further to 600 nm in group 7. The majority of NPs, namely 72% of the ensemble, are represented by these three groups of nanoplates. These groups are thus referred to as large, medium, and small plates. With LSPRs at about 500 nm, group 9 has a significant $\alpha \sim 1$, and $\widetilde{\sigma}_R$ is only marginally smaller than $\widetilde{\sigma}_L$. This suggests that the group consists of thick particles that are elongated in the plane, such as bipyramids or spheroids with a high aspect ratio, hence a high α . This cluster will be referred to as "rods" in the following. Group 5 closely resembles group 9, but with LSPRs that shift more towards the blue part of the spectrum, below 500 nm, outside the range of our measurements, suggesting a quasi-spherical form. Consequently, this group is referred to as spheroids in the following. Furthermore, $\widetilde{\sigma}_R$ slightly exceeds $\widetilde{\sigma}_L$, and α_L is reduced to approximately 0.5. This suggests the presence of pillars, namely plates that are thicker than they are wide and are standing upright. These pillars resemble the one observed in TEM image shown in Fig. 2.16, which has a diameter of around 25 nm. Alternatively, they could be spheroids with a longer axis oriented out-of-plane. To that end, the previously noted "long shadow effect" results in a 28% increase in $\widetilde{\sigma}_R$ compared to $\widetilde{\sigma}_L$ for a spherical NP.

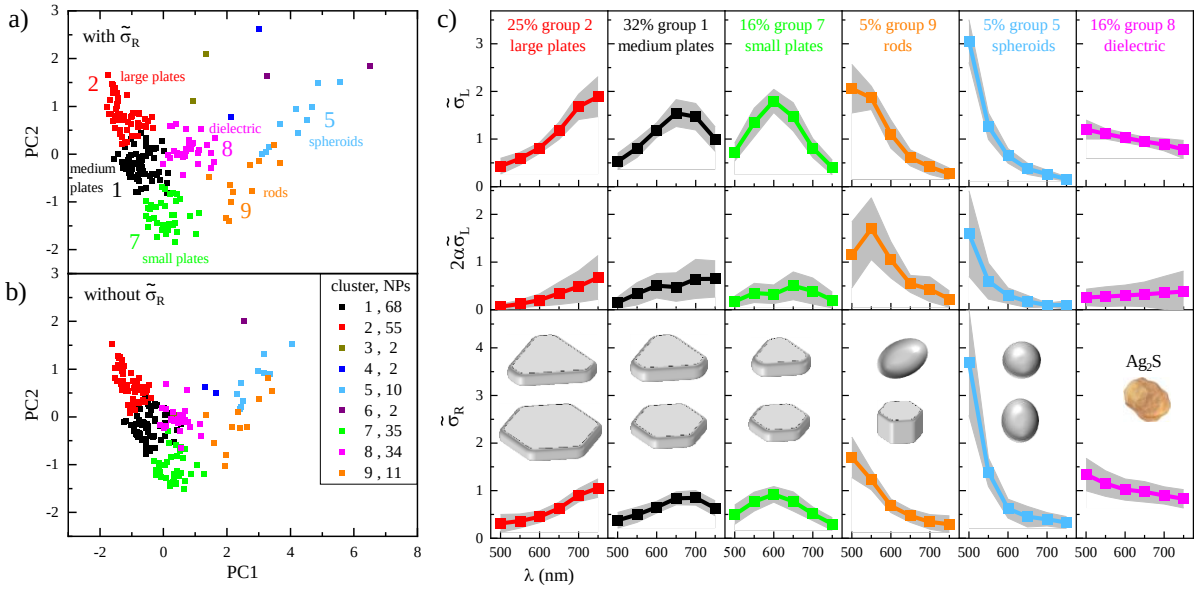

Figure 3.8: Cluster analysis results. a) Principal component analysis of the predictors over the nanoparticle ensemble, where values for the first and second principle components are shown. The symbol colour represents the group, with the group number and name specified. b) same as a) but not including $\tilde{\sigma}_{\mathrm{R}}$ in the Principal component Analysis. The number of NPs in each group is provided. c) Spectral analysis of the predictors for groups containing more than two NPs. The symbols represent the mean, whereas the grey area represents the standard deviation over the NPs in the group. The percentage of NPs in each groups indicated. Illustrative sketches of possible shapes are shown.

Furthermore, group 8 has a distinct behaviour: no LSPR and a steadily growing cross-section with decreasing wavelength, together with a nearly isotropic cross-section (small α and $\tilde{\sigma}_R$ close to $\tilde{\sigma}_L$). This suggests that Ag_2S contamination is likely because it occurs frequently. AgNPs are known to react more readily with sulfur compounds than with oxygen. The source of S^2 in the nanoparticle solution could be environmental contamination, such as exposure to atmospheric sulfur compounds like hydrogen sulfide or carbonyl sulfide. It is well-documented that AgNPs tarnish even under ambient conditions, forming a surface layer typically identified as silver sulfide (Ag_2S) [129][130][131][132]. However, further studies are necessary to confirm the precise composition of this contamination , or air bubbles in the oil medium. The cluster is referred to as "dielectric" in the following (more details were provided in 3.2.2).

3.2.1 Cluster analysis

Further details related to the cluster analysis are presented in this section. Unless otherwise stated, results denote the 9 group analysis which includes $\tilde{\sigma}_R$ as described in the previous section. As stated, the obtained cross-sections were normalised taking the average $\bar{\sigma}$ over all wavelengths and polarisations, for each particle. After that, the linear polarisation data were fitted as a function of γ_P to determine $\tilde{\sigma}_L$ and α. As explained previously, an 18-dimensional vector was employed as a descriptor for the clustering. This vector consisted of the values $\tilde{\sigma}_L$, $2\alpha\tilde{\sigma}_L$, and $\tilde{\sigma}_R$ at each wavelength. The average distributions of the cross section $\bar{\sigma}$ of the NPs within groups that include more than 10 NPs shown Fig. 3.9. The typical values are on the order of several few 1000 nm^2 . Group 2, consisting of NPLs with the highest aspect ratio (LSPR approximately 700 nm), exhibits the largest average area of about 2000 nm^2. By contrast, group 1, composed of NPLs with LSPR around 650 nm, has an average cross-section of about 1200 nm^2, while group 7, consisting of NPLs with LSPR around 600 nm, has an average cross-section of about 900 nm^2. This trend suggests that the height of the nanoplates remains relatively constant, with changes in aspect ratio mostly driven by variations in lateral size. Group 9 and 5, which consist of spheroids and rods, exhibit cross-sections values that resemble those of the small plates in group 7. Group 8, which contains dielectric NPLs, displays a cross-section histogram with a broad distribution, suggesting a wide range of sizes.

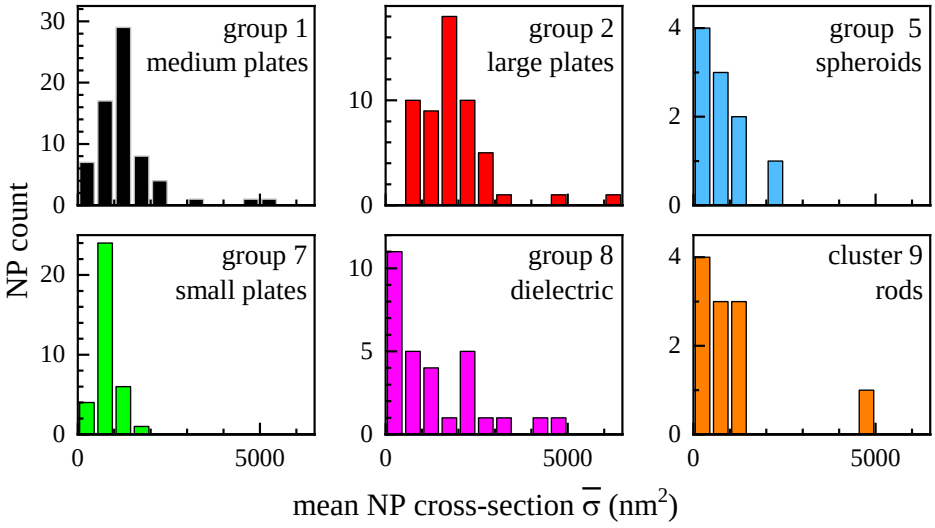

Figure 3.9: Histograms showing the average NP cross-section $\bar{\sigma}$ inside the corresponding clusters, as indicated by the labels.

3.2.1.1 Cluster separation

In order to examine the separation between pairs of groups in the 18-dimensional predictor space, Fig. 3.10 shows for each group pair the distribution of NP distances along the direction in the predictor space connecting the two group centroids. A distance of zero represents the midpoint between the centroids. As suggested by Fig. 3.8, group 1 is near group 2, and group 2 is near group 7. There is little separation between these groups and group 8. Group 9 has small separation to group 7, and group 9 is near to group 5. Group 9 is also adjacent to group 8. The other group pairings exhibit clear separation.

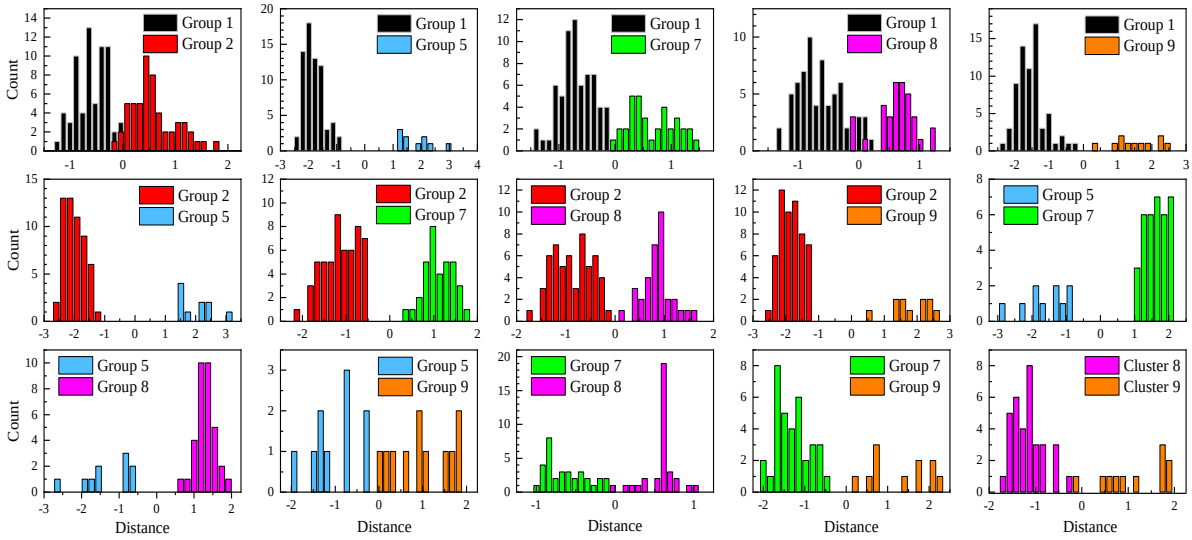

Figure 3.10: Histograms of the projected distance between NPs for pairs of groups. The groups are indicated and distances are measured along the connecting the group centroids in 18-dimensional predictor space. The zero position is set at the midpoint between the centroids. HCA data in Fig. 3.8.

The dendrogram of the cluster analysis in Fig. 3.8 and section 3.2.1 is displayed in Fig. 3.11, maintaining the colour coding of the clusters for the relevant branches.

3.2.1.2 Different number of groups

Fig. 3.12 displays the results of HCA using 5 to 12 groups, to highlight the choice of 9 components discussed in section 3.2.1. The figure shows the first and second PCA components and uses a cluster colour coding. When using five groups, the most populated ones are made up of rods and spheroids, small plates and dielectric, and large and medium plates. The dielectric NP and small plates are split when using more than 5 groups, while the large and medium plates are split when using more than 8 groups. By increasing the group number from 9 to 11, the outliers are divided into separate groups. With 12 groups, three NPs are separated from the small plates and form a group found between the small plates and rods. Therefore, the choice of 9 groups appears optimal to separate particles into meaningful groups, without under or over splitting.

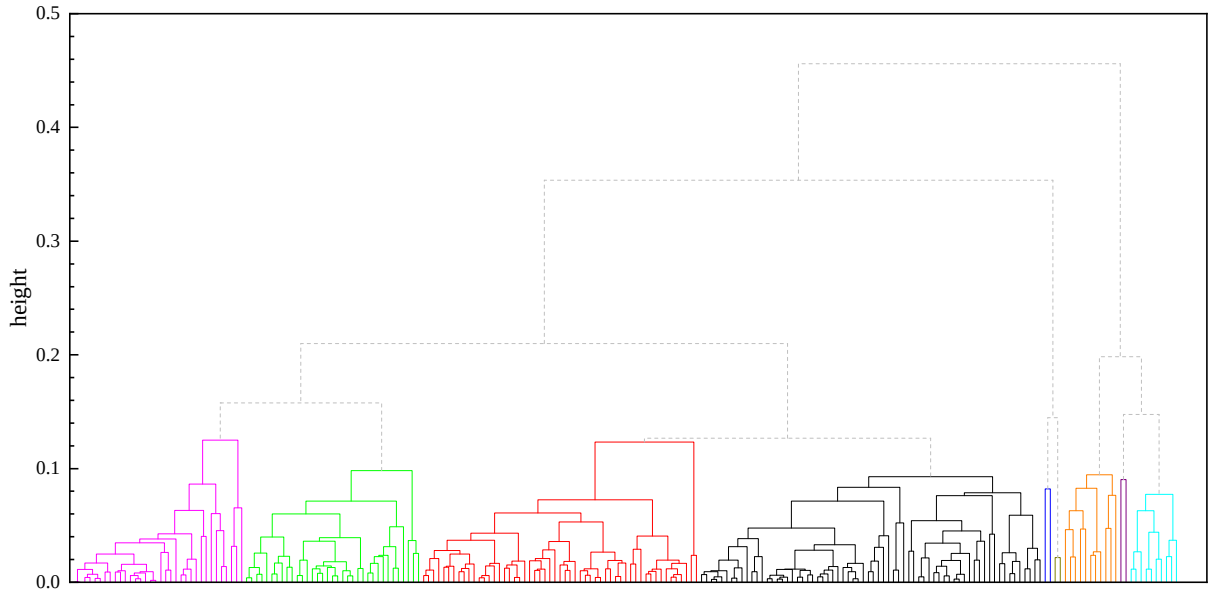

Figure 3.11: The dendrogram displays the hierarchical cluster analysis discussed in section 3.2.1, utilizing a cosine metric and average linkage. The branches' colors are the same as for the groups in Fig. 3.8.

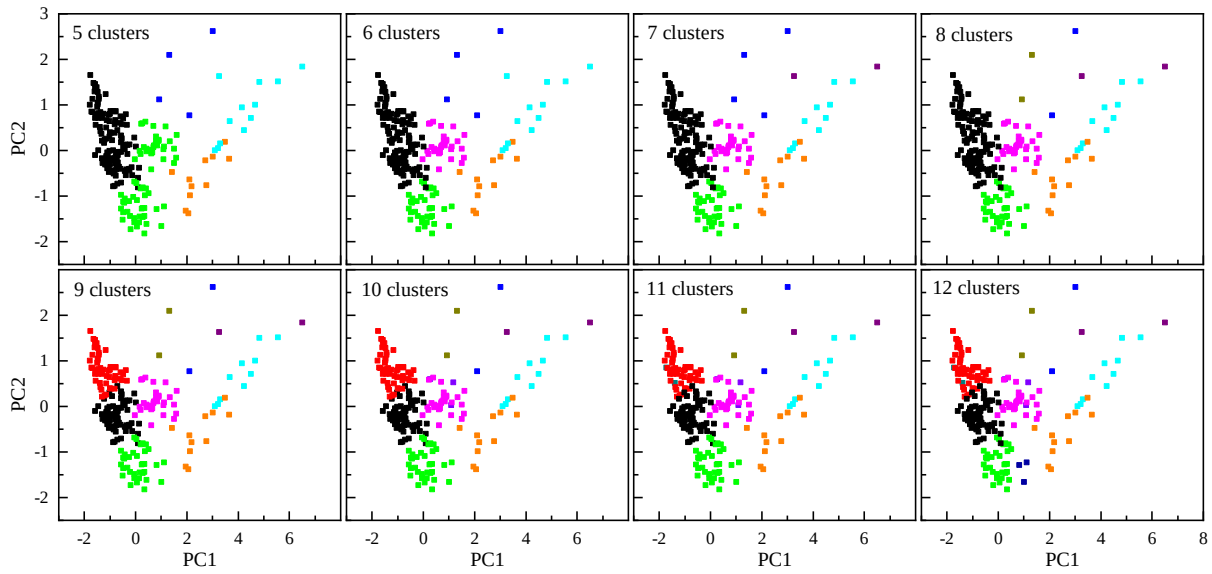

Figure 3.12: NP predictor first and second principal component values as in Fig. 3.8, using different number of groups. Number of groups ranging from 5 to 12, as indicated. NPs of different clusters have differently coloured symbols.

More analysis results for the 9 groups, as described in section 3.2.1, but using different linkages and metrics are shown in Ref [123].

3.2.1.3 Cluster analysis without radial polariser descriptors

HCA results when eliminating the radial polariser data ($\tilde{\sigma}_{\mathrm{R}}$) as predictors are displayed in Fig. 3.13. The separation between plates and dielectric NPs is no longer present. This can be understood considering the missing information about the axial polarisation response that relates to the extension of the NPs along the axial direction.

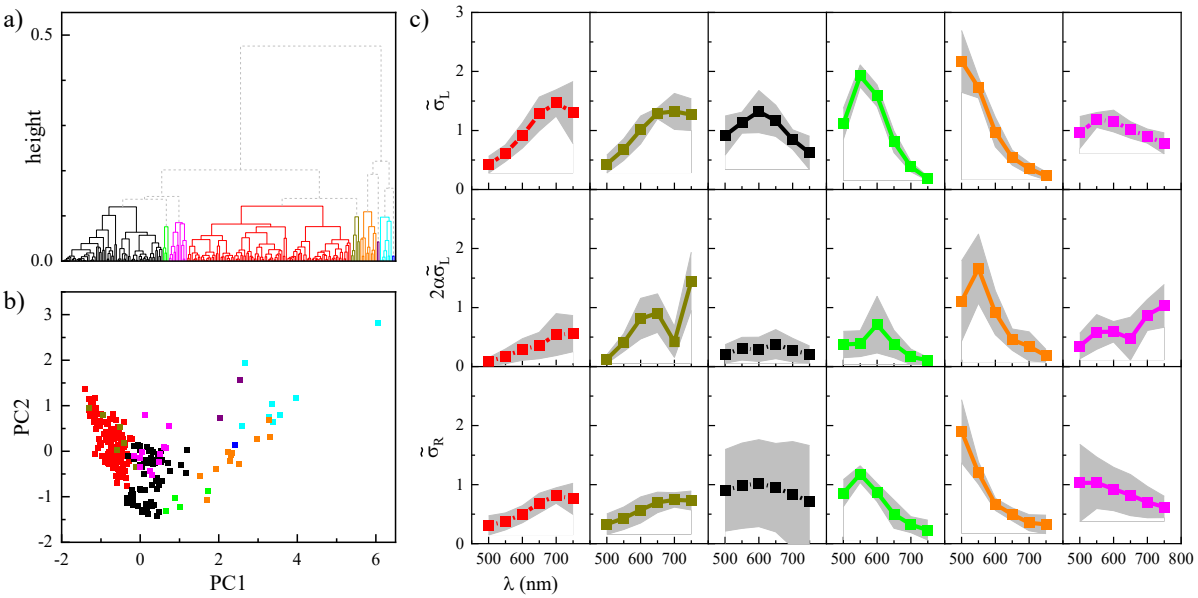

Figure 3.13: Results of HCA excluding the radial polariser cross-section. a) Dendrogram. b) First and second principal component values for predictors. The symbol's colour represents each group. c) Predictor spectra for group with more than two NPs. The average and standard deviation are shown by symbols and shaded region, respectively.

3.2.2 Modelling dielectric particles

As mentioned, nanoparticles in Group 8 in Fig. 3.8 display an small α_L and have $\tilde{\sigma}_R$ of similar value to ($\tilde{\sigma}_L$). They are not showing a LSPR, but instead, their cross-section value gradually increases as the wavelength decreases. This suggests an attribution of these particles as absorption of non-metallic dielectric NPs, possibly made of Ag_2S, which is the primary product of Ag decomposition, commonly referred to as tarnish. Ag_2S is a semiconductor that has a band gap of around 1 electron volt (eV) [126]. By utilizing the refractive index ($n = 3.08$) and absorption index ($\kappa = 0.77$) reported in section 3.2 on Ag tarnish with a thickness of 38 nm at a wavelength of 500 nm [126], the absorption cross-section of a spherical NP with radius r in the dipole limit, can be calculated as follows [133].

$$\sigma_{abs} = \frac{8\pi^2 r^3 \sqrt{\epsilon_m}}{\lambda} \mathrm{Im}\left[\frac{\epsilon_p - \epsilon_m}{\epsilon_p + 2\epsilon_m}\right], \tag{3.1}$$

where $\epsilon_p = (n + i\kappa)^2$ is the permittivity of the NP and ϵ_m is the medium permittivity. Using the silicon oil refractive index $\sqrt{\epsilon_m} = 1.52$, an NP radius of 30 nm this formula gives a cross-section of $1000\,\mathrm{nm}^2$, consistent with the measured values (see Fig. 3.9). The group spectra in Fig. 3.8(c) illustrate that there cross-section drop by about a factor of two, going from 500 nm to 750nm wavelength. This is consistent with the calculation in equation 3.1 when using the reported values of n = 2.93 and $\kappa = 0.34$ at 700nm which results in a cross section (for the same particle radius) reduced to 354 nm^2 [134]. Moreover, converting a silver plate of 40 nm across and 10 nm thick into the volume of a sphere gives a radius of only 16.5 nm, which for Ag_2S results in a cross-section of 173 nm^2. Considering the distribution of measured cross-section magnitudes in Fig. 3.9, it is likely that aggregation of these tarnish NPs occurs, and accounts for part of the observed results. Another possibility is to explain the NPs in a group 8 as, air bubbles. Based on Mie theory (MiePlot v3413), the scattering cross-section of air bubbles in oil versus their radius is shown in Fig. 3.14 for the 6 wavelengths utilised in the measurements. For radii greater than 30 nm, one can observe a deviation from the r^6 scaling of the Rayleigh limit. At a radius of 80 nm, the scattering cross-section is in the range of $1000\,\mathrm{nm}^2$, which is comparable to the $\bar{\sigma}$ value of the dielectric group 8 (Fig. 3.9).

The wavelength dependence at this radius (as seen in the inset in Fig. 3.14) exhibits a decrease by a factor of 3 from 500 nm to 750 nm, slightly more than the observed experimental trend. Notably scattering light is partially collected by the high NA objective, resulting in a decrease of approximately 30% in the measured extinction cross-section compared to the nominal one for isotropic scattering. Moreover, a bubble with a radius of 80 nm exceeds the Rayleigh limit and exhibits higher forward scattering than backward scattering, which increases the amount of scattered light being collected by the objective and thus decreases the measured cross-section. In turn, this could explain the reduced dependence on wavelength found in the data. Bubbles are likely spherical in shape and thus expected to have a small α_L. The observed $2\alpha\tilde{\sigma}_L$ exhibits a standard deviation that is equivalent to the mean, as illustrated in Fig. 3.8. This suggests the presence of both bubbles with small $\alpha < 0.1$ and non-spherical tarnish NPs with significant α within this group.

3.3 Modelling AgNPLs extinction

Prof. Wolfgang Langbein utilized the finite element solver COMSOL to simulate the scattering and absorption spectra of AgNPLs and compare these computational expectations with the experiments. A comparison between calculated and experimental spectra for specific nanoparticles representative within given groups are displayed in Fig. 3.15. For the simulations, a flexible geometric model had to be developed to precisely define a silver nanoplate, including the edge and

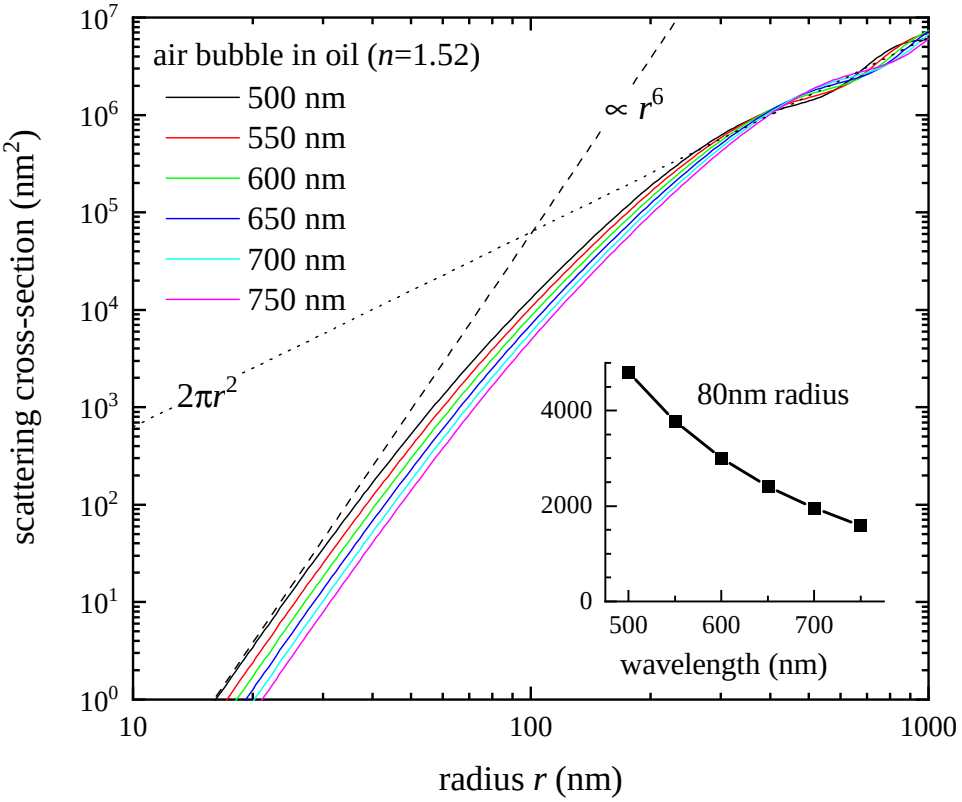

Figure 3.14: scattering cross-section of air bubbles in oil ($n = 1.52$) as a function of bubble radius at various wavelengths. The dashed line represents the r_6 scaling in the Rayleigh limit, when r is much smaller than λ. The dotted line represents twice the geometrical cross section $2\pi r^2$, which is approached when r is greater than λ. The inset shows how the scattering cross-section for a bubble with a radius of 80 nm varies with the wavelength.

corner radii, thickness, and distances of all six edges to the centre of the plate [123]. A 2 nm edge rounding, and a 5 nm corner rounding were typically used. In group 2, the chosen NP exhibits a LSPR at around 710 nm, with minimal polarisation splitting and a significantly high peak cross-section of approximately 6000 nm^2.The simulated spectra showed good agreement for both linear and radial polarisers data, using a geometry consisting of a nearly hexagonal nanoplate with a height of 6.3 nm and center-to-edge distances of 24 nm along the x-axis and 23 nm for the other distances. For group 1, a comparison is made with two selected NPs. NP #1 exhibits no polarisation splitting of the LSPR, centred at a wavelength of 650 nm, which is consistent with the simulated spectra of a hexagonal nanoplate with a height of 5.4 nm and a center-to-edge distance of 16.5 nm. A triangular shape was found to similarly model the experimental spectra, although with slightly less agreement. NP #2 exhibits a strong polarisation separation of the LSPR, with peaks at 710 nm and 610 nm, indicating the presence of an elongated plate. Simulated spectra assuming a nanoplate with a height of 5 nm, a centre-to-edge distance of 18 nm along the x axis, and 14 nm for the other distances show good agreement with the experiments. Group 7 does not show any polarisation splitting of the LSPR at 650 nm. The selected NP data are well explained by simulated spectra assuming a triangular nanoplate with a height of 6.1 nm and alternating center-to-edge distances of 10 nm and 14 nm. A hexagonal geometry can also be used to represent the data, however assuming a thickness less than 5 nm, significantly below the nanoplate specifications from the manufacturer. Additional details, on these calculation, such as

scattering and absorption spectra, as well as local field distributions, can be found in [123]. The observed spectra can be understood not as contributions from dielectric particles, oil bubbles, or silver tarnish, but rather from the geometries anticipated in the sample, as confirmed by TEM analysis.

In conclusion, the comparison between simulation and experimental data shows consistency in terms of particle size and shape. The amplitude, localized surface plasmon resonance position, and spectral width align reasonably well with the experimental results, as observed in the TEM images. However, an exact match is not achieved due to the lack of precise knowledge about the geometry of the specific particles analysed experimentally. The observed spectra can be interpreted using silver plate geometries that correspond to those identified in our sample. A more precise one-to-one comparison would require correlative analysis, as demonstrated in Ref [150].

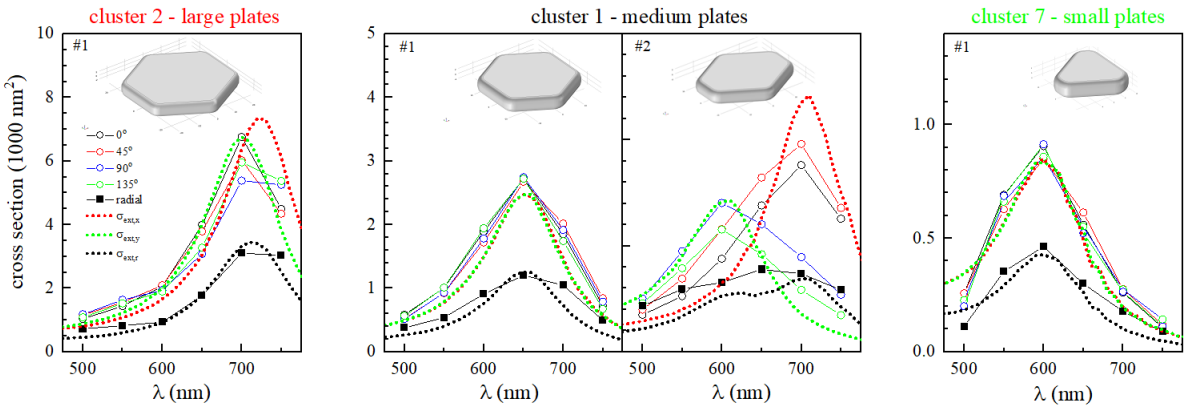

Figure 3.15: Comparison between simulated and experimental cross-section spectra for selected NPs. The spectra were measured using linear polarisation at four angles γ_P (shown by circles), as well as for the radial polariser (represented by squares). For experimental data, measured spectra, the lines are guides to the eye. Simulated spectra, represented by dotted lines, are displayed alongside their corresponding geometries. These spectra are displayed for the linear polariser along the longer wavelength LSPR axis x (red), the shorter wavelength LSPR axis y (green), and for the radial polariser (black).

3.4 SiO_2-AgNPLs cluster analysis

The cluster analysis of SiO_2-AgNPLs was performed following the same steps outlined in section 3.2. However, using the same predictors as for the PVP-AgNPLs did not produce a meaningful outcome, namely particles were not separated into groups having different spectra. A significant difference between silica coated and PVP coated plates, is the shape and thickness of the silica shell which may cause particles not to lie flat on the glass surface after deposition. To that end, new combinations of the measured cross-sections were considered as alternative predictors. The main idea was to look for a combination of cross-sections giving an average over the particle orientations, such that identical particles oriented differently would appear in the same group. Therefore, a new predictor was defined as the normalised average between σ_R and σ_L, at each wavelength, as shown in equation 3.2.

$$\bar{P} = \frac{\sigma_{R,i} + f_{\sigma_L}\sigma_{L,i}}{\frac{1}{W}\sum_i (\sigma_{R,i} + f_{\sigma_L}\sigma_{L,i})} \tag{3.2}$$

Where i refers to the wavelength index, and W=6 is the number of measured wavelenghts. The factor f_{σ_L} is estimated by minimizing the following quantity:

$$\sum_{i=1}^{W} \mathrm{var}(P) \tag{3.3}$$

where var is the variance calculated over the NP population and P is given by

$$P = \begin{cases} \frac{\sigma_{R,i}+f_{\sigma_L}\sigma_{L,i}}{\sigma_{n,i}} < 0 & \frac{\sigma_{R,i}+f_{\sigma_{L,i}}\sigma_{L,i}}{\sigma_{n,i}} \\ \frac{\sigma_{R,i}+f_{\sigma_L}\sigma_{L,i}}{\sigma_{n,i}} \geq 0 & \log\left(\frac{\sigma_{R,i}+f_{\sigma_L}\sigma_{L,i}}{\sigma_{n,i}} + 1\right) \end{cases} \tag{3.4}$$

with $\sigma_{n,i}$ defined as

$$\sigma_{n,i} = \frac{1}{Q}\sum_{j=1}^{Q}\sqrt{\frac{1}{N}\sum_{l=1}^{N}\left(\sigma_{i,j,l} - \frac{1}{N}\sum_{l=1}^{N}\sigma_{i,j,l}\right)^2} \tag{3.5}$$

where j is the polarisation index (For the noise measurement, only linear polariser was used (N=4) and 1 radial) and l is the datapoint index used to calculate the noise in the data with N=1001 datapoints evaluating the cross-section in regions without nanoparticles. In essence, P represents as value that accounts for the magnitude of the cross section, and is calculated such that big particles with large cross-section are not dominating, by taking the logarithm. The normalisation to σ_n is introduced to create a unitless quantity such that the log function can be applied. The criteria of having f_{σ_L} as the value that minimises the variance of P over the particle population is then applied, in order to find the combination of σ_R and σ_L that minimises the variance due to particle orientations. Interestingly, this value is found to be f_{σ_L}= -0.11, indicating that the predictor is dominated by σ_R. This can be understood considering that, for these experiments, the radial polariser in the illumination was used without the stop-light disk, so the full illumination NA from 0 to 1.34 NA was applied. This resulted in illumination polarisation components that were nearly identical, hence, effectively illuminating particles equally, irrespective of their orientation. The results of the cluster analysis using the predictor in equation 3.2 and shown in Fig. 3.16. For this analysis, it was found that 10 groups provided an optimum separation between the particles, resulting in distinct spectra of the predictors, without under or over splitting. An overview of the first and second principal components for the NP predictors when varying the group number from 7 to 14 is shown in Fig. 3.17.

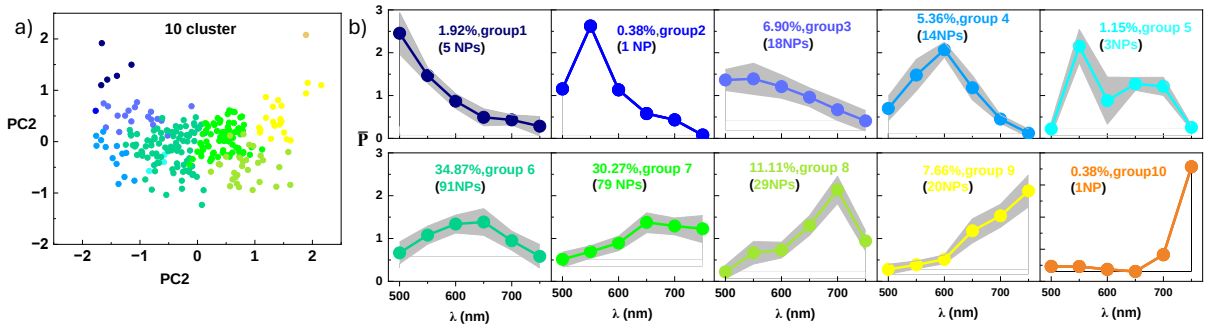

Figure 3.16: SiO_2-AgNPLs cluster analysis results. a) First and second principal component values for the NP predictors in equation 3.2. The symbol colour represents 10 different groups. b) Predictor spectra for the 10 groups in (a). The symbols represent the mean, whereas the grey area represents the standard deviation over the SiO_2-AgNPLs in the group. The distribution of NPs in each cluster is provided.

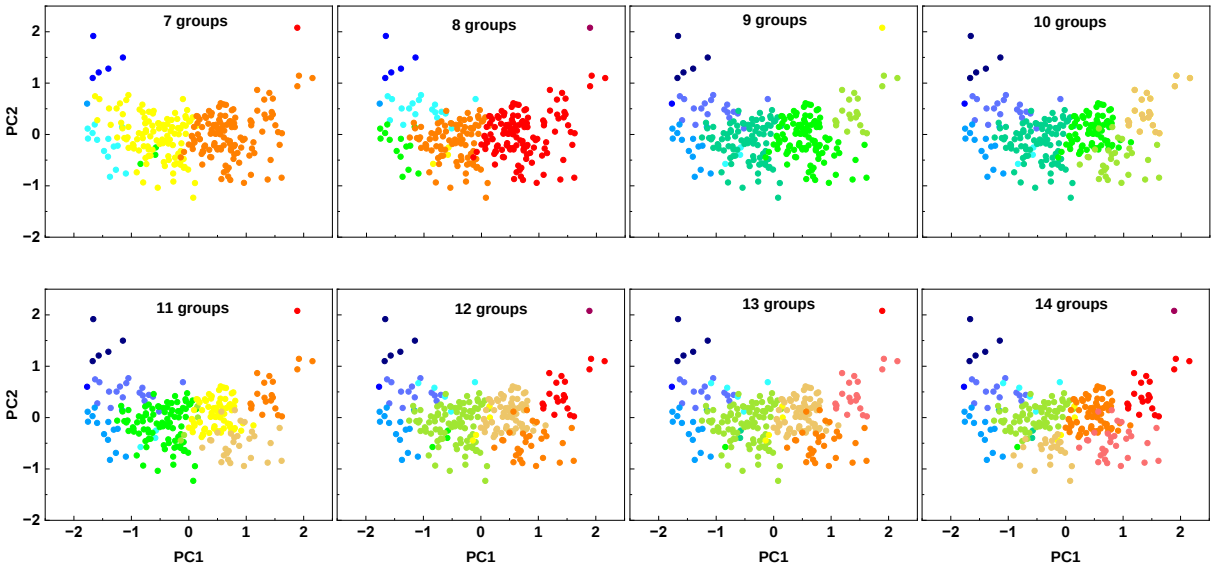

Figure 3.17: NP predictor first and second principal component for different number of groups. Cluster analyses as in Fig. 3.16, using different number of groups from 7 to 14, as indicated. SiO_2-AgNPLs in different groups have differently coloured symbols.

When the cluster analysis was repeated using only σ_R in the predictor, namely:

$$\overline{P} = \frac{\sigma_{R,i}}{\left(\frac{1}{W}\sum_i \sigma_{R,i}\right)} \tag{3.6}$$

similar results were obtained, in terms of particle separations into groups, as depicted in Fig. 3.18. Here, it was found that an optimum separation was achieved using 9 groups, see also Fig. 3.19 (where the NP predictor first and second principal component for different number of groups

was shown). To that end, an interesting conclusion of this work is that the measurement method can be simplified by utilizing solely the radial polariser with full 0-1.34 NA, to provide a form of isotropic illumination and hence averaging over the particle orientation.

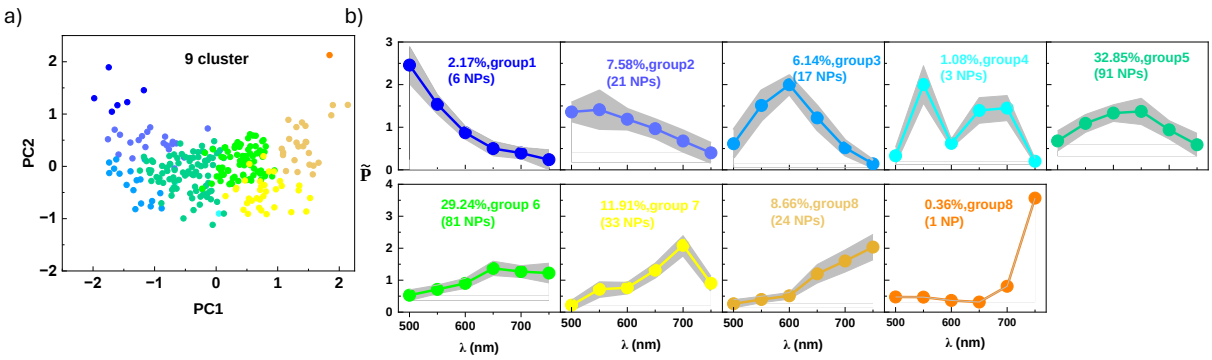

Figure 3.18: SiO_2-AgNPLs Cluster analysis results using $\tilde{\sigma}_R$ only. a) First and second principal component values for the NP predictors. The symbol colour represents 9 different groups. b) Predictor spectra. The symbols represent the mean, whereas the grey area represents the standard deviation over the SiO_2-AgNPLs in the group. The distribution of NPs in each cluster is provided.

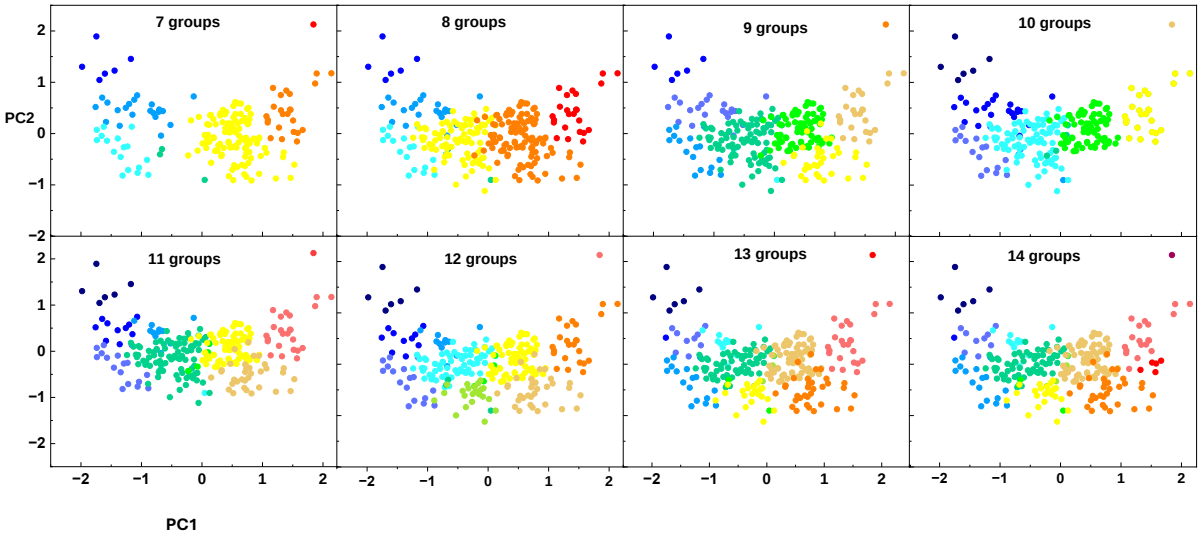

Figure 3.19: NP predictor first and second principal component values with group number from 7 to 14 , using cluster analyses as in Fig. 3.18. SiO_2-AgNPLs of different clusters have differently coloured symbols.

Chapter 4

Rotational averaging in viscous medium

4.1 Object rotational averaging in viscous medium

The characterization of particle movement within a viscous medium is an importance topic in many research fields including biophysics, fluid mechanics and colloid science [135]. In a medium with known viscosity, the random motion of particles is well characterized by rotational and translational dynamics, related to Brownian diffusion. The idea behind rotational diffusion dynamics in our experiments involves the examination of the time-averaged characteristics shown by a silver nanoparticles within a certain duration, sufficiently long to provide an average over all possible particle orientations. Factors that influence rotational averaging are the viscosity of the surrounding medium, the size and shape of the particle, temperature and any external forces applied. For example, under Brownian motion smaller objects diffuse faster. Moreover, the viscosity of a substance can be influenced by temperature [136]. The key point behind the employment of SiO_2-AgNPLs in conjunction with a viscous medium lies in the shape characteristics of these nanoparticles. The thick and round-edged silica shell surrounding these particles prohibits them from having a flat orientation when deposited onto glass surface. As a result, identical SiO2-AgNPLs would exhibit different optical extinction cross sections under polarised-light illumination, due to their different orientation, as discussed Chapter 3. When examining a heterogeneous population of nanoparticles, it becomes important to remove this variability due to particle orientation, in order to distinguish nanoparticles solely based on their different sizes and shapes. In this Chapter, we examined SiO_2-AgNPLs diffusing in a viscous medium, and measured their extinction cross section, with the view to achieve a time average of the rotational behaviour. As stated in Chapter 2 section 2.3.3, the equation of Brownian translation diffusion has been utilized as a precious tool to determine the viscosity in a relevant liquid. In the following, equation 4.1 is used to describe the rotational behaviour of a nanoparticle. The angle of diffusion (mean-square angular deviation) around a single axis over the time (t) can be determined by equation $\theta^2 = 2D_r t$, where D_r represents the rotational diffusion constant [137]. For a spherical particle, this constant is defined as

$$\mathrm{Dr} = \frac{k_B T}{8\pi\eta_s r_p^3} \tag{4.1}$$

The symbol k_B represents Boltzmann's constant, which has a value of 1.38×10^{-23} J/K. T is the temperature measured in Kelvin (K), with a typical value of 300 K for room temperature. η_s represents the dynamic viscosity of the solvent, measured in units of [Ns/m^2] equivalent to [Pa s]. The variable r_p represents the radius of the particle, measured in metres. Notably, we found

that honey possesses the required viscosity, making it the suitable liquid for our experiments (see also Chapter 2)

4.2 Using honey as viscous medium

Honey, an organic product with a rich historical background in therapeutic usage, has recently gained recognition as a promising option owing to its remarkable physical and chemical characteristics. Ancient people used natural honey for medicine. Honey was originally used as a medicine in 2100-2000 BC in a Sumerian tablet and ointment [138][139]. Many animal research showed that honey influences cardiovascular risk factors like hyperlipidemia and free radical generation [140]. Honey has a viscosity significantly larger than water (η_s for water is 0.001 Pa.s), with values ranging from 3 to 20 Pa.s at room temperature [113], which may be adjusted by composition and moisture. Honey is noted for its biocompatibility and no toxicity. It has been used for ages to heal wounds and treat numerous ailments topically. Its safety makes it excellent for biomedical nanoparticle transport, decreasing unknown reactions. Honey has medicinal benefits as well as carrier properties. Its antibacterial, anti-inflammatory, and antioxidant properties boost nanoparticle therapy [141]. Recent research has investigated the utilisation of honey as a medium for transporting many types of nanoparticles, including gold, silver, and drug-loaded nanoparticles.

4.2.1 Physical properties of honey

Honey is a sweet substance that is naturally occurring and produced by honeybees through the enzymatic transformation of flower nectar, and has numerous physical characteristics. It exhibits a noticeable viscosity, as shown by its slow motion and elevated consistency. The variation in viscosity can be relative to certain fluctuations in temperature and moisture content. The colour of honey differs within a range from light yellow to dark amber by taking into consideration the type of flower from which the nectar is formed. In general, light honey displays a more subdued flavour profile, and vice versa for the dark honey. Even though honey is transparent, the presence of suspended particles like pollen or air bubbles can negatively influence its purity. Honey, has an approximate density of 1.4 g/cm^3, significantly higher than water 1 g/cm^3. The crystallization process of honey may occur over a period of time, depending on several factors such as composition and temperature. Crystallized honey can be transformed into a liquid state again by gently heating it. Honey displays a relatively elevated surface tension, which will lead to the formation of a unique convex shape when poured and will show resistance to easy spillage. Moreover, it has a distinctive scent, and the origin of nectar would determine its variation. Differing along the spectrum from subtle to intense, the taste profile of honey is well known for its sweetness. The nectar source is of course the key player in this variation. The pH level of honey varies from 3.4 to 6.1, which is slightly acidic, although there might be specific variations depending on the specific type of honey. Honey effectively attracts and retains moisture, mainly due to its hygroscopic nature, which provides it with preservative properties. In terms of thermal properties, honey has been widely used as a natural sweetener in the culinary arts because of its special attributes of resistance to temperature fluctuations and high heat capacity. Moreover, honey is considered substance with low electrical conductivity; this property by itself is used in the process of differentiating original honey from those that have been diluted or adulterated. It is important to note that the physical properties of honey exhibit variations, as they are subjected to numerous influences, including floral source, processing techniques, and geographic origin [139][142]. Honey typically contains 80–85% carbs, 15–16% water, 0.1–0.4% protein, and 0.2% ash, enzymes, vitamins, trace amino acids, and phenolic antioxidants. The physical

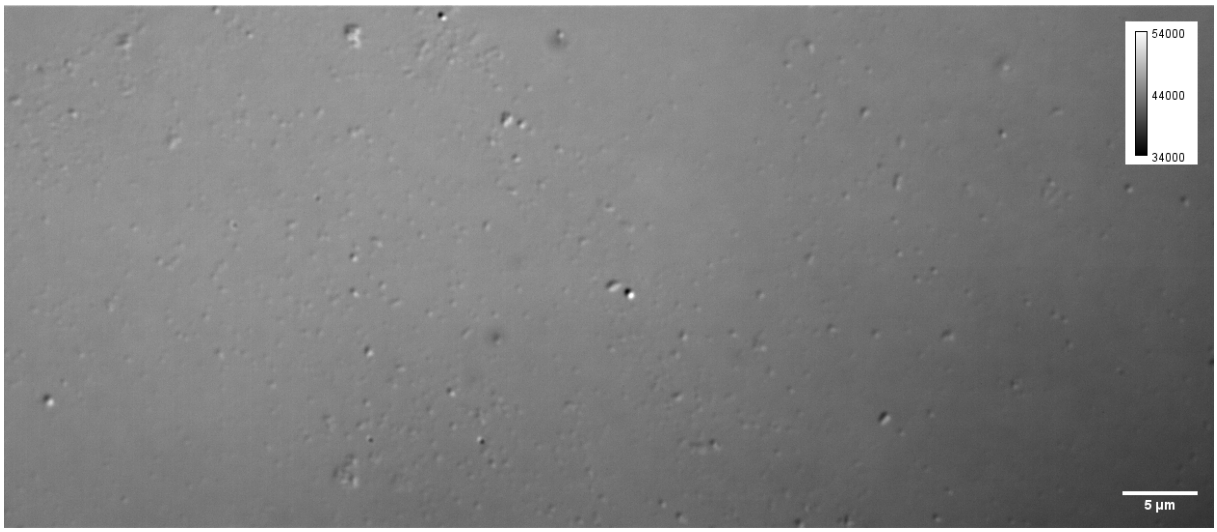

Figure 4.1: Unpurified Honey with Debris and Sugar particles : This transmission DIC image depicts unpurified honey with visible debris and sugar crystals. The sample was prepared by adding 10µL of honey that had not undergone any filtration or refinement processes on a clean coverslip, then covered with a glass slide, highlighting the presence of impurities and unprocessed components within the honey. A 100 × 1.45 NA oil immersion objective (Nikon MRD01905) and a 1× tube lens were used to capture the transmitted light at an polarisation angle $\gamma_P = 15°$, with 80 ms exposure time, and averaging over 128 frames. A green interference filter (GIF) from Nikon was used to produce light with a peak emission wavelength of 550 nm and blue filter (SchottBG40) was used to cut off infra red wavelength outside the working range of the DIC optical components but detectable on camera. The image size is 1256 × 541 pixels with a pixel size of 64.1 nm. The image contrast is on a linear grayscale, as indicated.

and chemical qualities of honey rely on different factors such as climate, vegetation, and plant type. Main carbs like fructose and glucose are swiftly absorbed in the gut. Honey contains vitamin C, B1, and B2 complex vitamins, plus various levels of proteins. Flavonoids, phenolics, and bioactives are present. Minerals include potassium, calcium, magnesium, sodium, sulfur, phosphorus, iron, copper, zinc, and manganese [139].

4.2.2 Honey purification

As mentioned above, there are many types of honey, and each type differs from the other depending on many factors, for example, the amount of sugar present. Therefore, when using honey as the viscous medium for our experiments with silver nanoparticles, high purity must be obtained in order to get rid of any sugar crystals and debris inside it. Otherwise, these impurities will appear against the background, causing confusion in interpreting the results of the extinction cross-sectional area, especially when these debris can scatter or absorb light. Therefore, a significant amount of work was devoted to developing and optimise a specific protocol through which the honey was purified.

4.2.2.1 Sugar particles and debris

The scattering and absorption of light by sugar can vary, depending upon parameters such as its physical forms, concentration, and the particular sugar species under consideration [19]. As a result, work was done to purify the honey from these impurities as mentioned in Section 2.3.3,

namely by diluting the honey with water and using a centrifuge to ensure the sedimentation of these impurities and getting rid of them. The image in figure 4.1 shows the optical contrast (transmission DIC) of raw honey before undergoing any purification process.

4.2.2.2 Heat treatment

As previously discussed in section 2.3.3, after water was added to honey, it was removed in order to maintain the viscosity of honey by the process of evaporating the additional water content. Moreover, it was found that treating the honey with high temperatures, such as 70°C, resulted in a change in its colour prior to the removal of the additional water volume [143]. Honey's sugars caramelise when heated, darkening its colour [144]. The heating process also forms blue-green low molecular-weight chemicals, which darken honey [145]. Consequently, it was determined that the honey maintains its inherent characteristics, including colour stability, while subjected to a temperature of up to 50°C. The rate of evaporation of the introduced water is observed to be very slow. It takes approximately 10 hours. Fig. 4.2 shows an example of honey before and after heating at 70 C, highlighting the colour change.

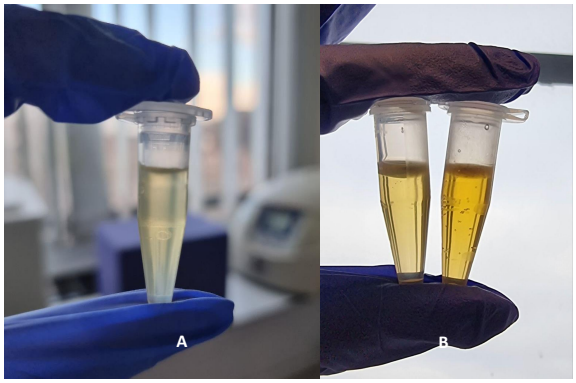

Figure 4.2: Comparison of honey before and after heat treatment, demonstrating colour change : (A) mixture of honey and added water before any processing (B) one the right hand side of image B honey is treated with 70°C while on the left hand side honey is treated with 50°C .

4.2.2.3 Sample preparation process

To prepare a sample containing nanoparticles diffusing in a viscous liquid, there are several factors that need to be controlled. A parameter that was specifically addressed in our sample preparation method, was the thickness of the honey layer, within which nanoparticles are diffusing. Controlling this thickness is important in order to ensure that nanoparticles are diffusing within a volume that is accessible optically, in the extinction microscopy experiment. For example, if this thickness is smaller than the microscope objective axial depth of focus, nanoparticles can be maintained axially in focus while diffusing. To control the thickness of the sample several factors must be considered, including the viscosity of the honey used, the time and pressure applied to vertically squeeze the honey, and the temperature. A formula was derived to scaling the thickness of the honey versus the time for the sample coverslip squeezing, by considering laminar flow of the honey between the two inner surfaces based on this reference [116].

$$\frac{F}{\rho \cdot \nu^2} = -\frac{3\pi}{2}\left(\frac{r_e}{h}\right)^4 \cdot \frac{h}{\nu}\frac{\partial h}{\partial t} + \left(\frac{\partial h}{\partial t}\right)^2 \tag{4.2}$$

Where (ν) is the kinetic viscosity, h thickness, r_e is the radius of the coverslip area over which a pressing force is applied, t is the time, ρ is the density and F is the applied force, and

$$v = \frac{\eta}{\delta} \tag{4.3}$$

with η being the dynamic viscosity. Neglecting the quadratic term on the right hand side in equation 4.2 (negligible for small thicknesses and high viscosities), we have:

$$F = -\frac{3\pi}{2}(\frac{r_e}{h})^4 \cdot \eta\frac{\partial h}{\partial t} \tag{4.4}$$

$$dt = -\frac{3\pi\eta r_e^4}{2F} \cdot \frac{dh}{h^3} \tag{4.5}$$

$$\int_0^t dt = \int_{h(0)}^{h(t)}(-\frac{3\pi\eta r_e^4}{2F} \cdot \frac{dh}{h^3}) \tag{4.6}$$

$$t = \frac{3\pi\eta r_e^4}{4Fh^2}|_{h(0)}^{h(t)} \tag{4.7}$$

Simplify more

$$t = \frac{3\pi\eta r_e^4}{4F}\left[\frac{1}{h} - \frac{1}{h(0)^2}\right] \tag{4.8}$$

$$h(t) = \frac{1}{\sqrt{\frac{1}{h(0)^2} + \frac{4Ft}{3\pi\eta r_e^4}}} \tag{4.9}$$

For large t, this can be further simplified as

$$h(t) = \sqrt{\frac{3\pi\eta}{4Ft}}\, r_e^2 \tag{4.10}$$

Using this formula, the following estimates can be made. Let us consider a coverslip of diameter $\varnothing = 24$ mm, hence $r_e = 12$ mm, and an initial thickness $h(0) = 10.5\,\mu$m (corresponding to a volume of $50\,\mu$L). For the viscosity η of honey, let us consider the values of 0.1 Pa.s at $T = 60°$C, 1.316 Pa.s at $T = 40°$C, and 14 Pa.s at $T = 20°$C [146]. Using a force of $F = 10$ N, at $T = 60°$C we obtain $h = 2.2\,\mu$m after $t = 100$ s, and $0.7\,\mu$m after 1000 s. Assuming $F = 2$ N

and $T = 40°\mathrm{C}$, we obtain $h = 5.7\,\mu\mathrm{m}$ after 1000 s, and $0.9\,\mu\mathrm{m}$ after 12 hours. A value $h < 1\,\mu\mathrm{m}$ is suited for a thickness smaller than the microscope depth of field.

However, it has been found that preparing a very thin sample leads to seeing the shadow of particles stuck to both surfaces (the glass slide and the coverslip), which is undesirable as they are fixed particles. An example of this effect is shown in Fig. 4.3.

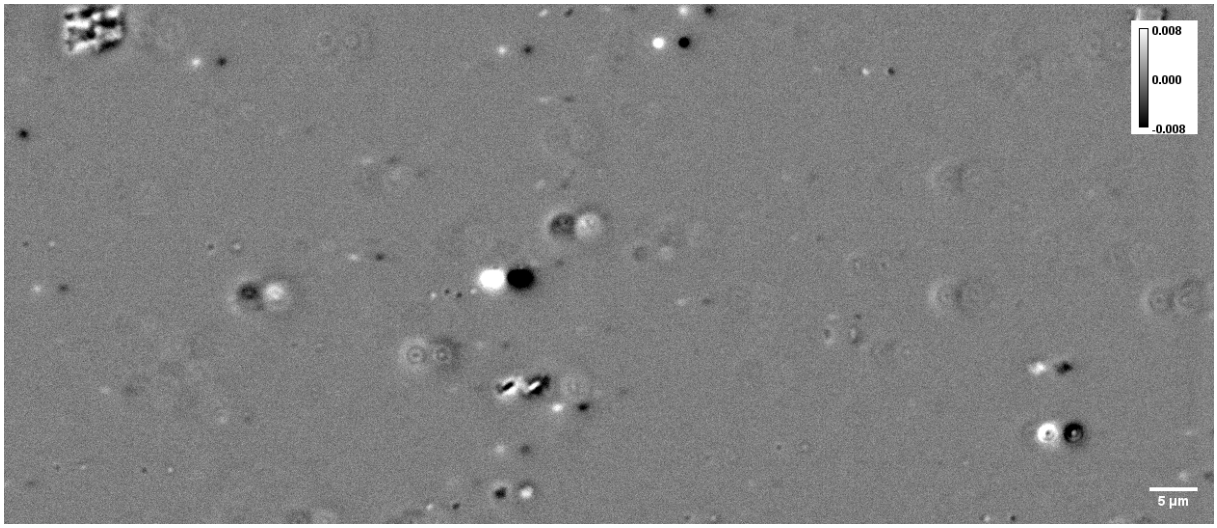

Figure 4.3: Extinction contrast image at 650 nm wavelength showing a representative field of view for a sample containing SiO_2-AgNPLs in a thin layer of honey (2.5 µm thickness): The sample is imaged in the middle between two inner glass surfaces. The image shows fixed SiO_2-AgNPLs particles on both surfaces, causing shadows. The image contrast is on a linear grayscale, as indicated.

As stated previously, our aim is to measure particles free to rotate in the viscous honey, as sketched in Fig. 4.4.

Therefore, work was done to prepare a sample with about 10 µm thickness and then measure the extinction cross-sectional area in the middle of this thickness, to get rid of the shadow form fixed particles on both surfaces of the sample. It is worth noting that the thickness of the honey layer is measured by determining the location of the two inner glass surfaces of the sample , namely the top coverslip and the bottom glassslide surface, by controlling the axial position of the sample using the nano-stage. The thickness of the layer was found to be different from one region to another and this could be due to the applied weight used to generate F not being perfectly level. To avoid this issue, a metal plate was placed under the coverslip when the weight was applied during the sample preparation Fig. 2.7 step 6. Furthermore, it was discovered that some of the coverslips utilized were not quite level, as shown by the findings of some AFM images (see Fig. 4.5), which will be elucidated in Chapter 5.

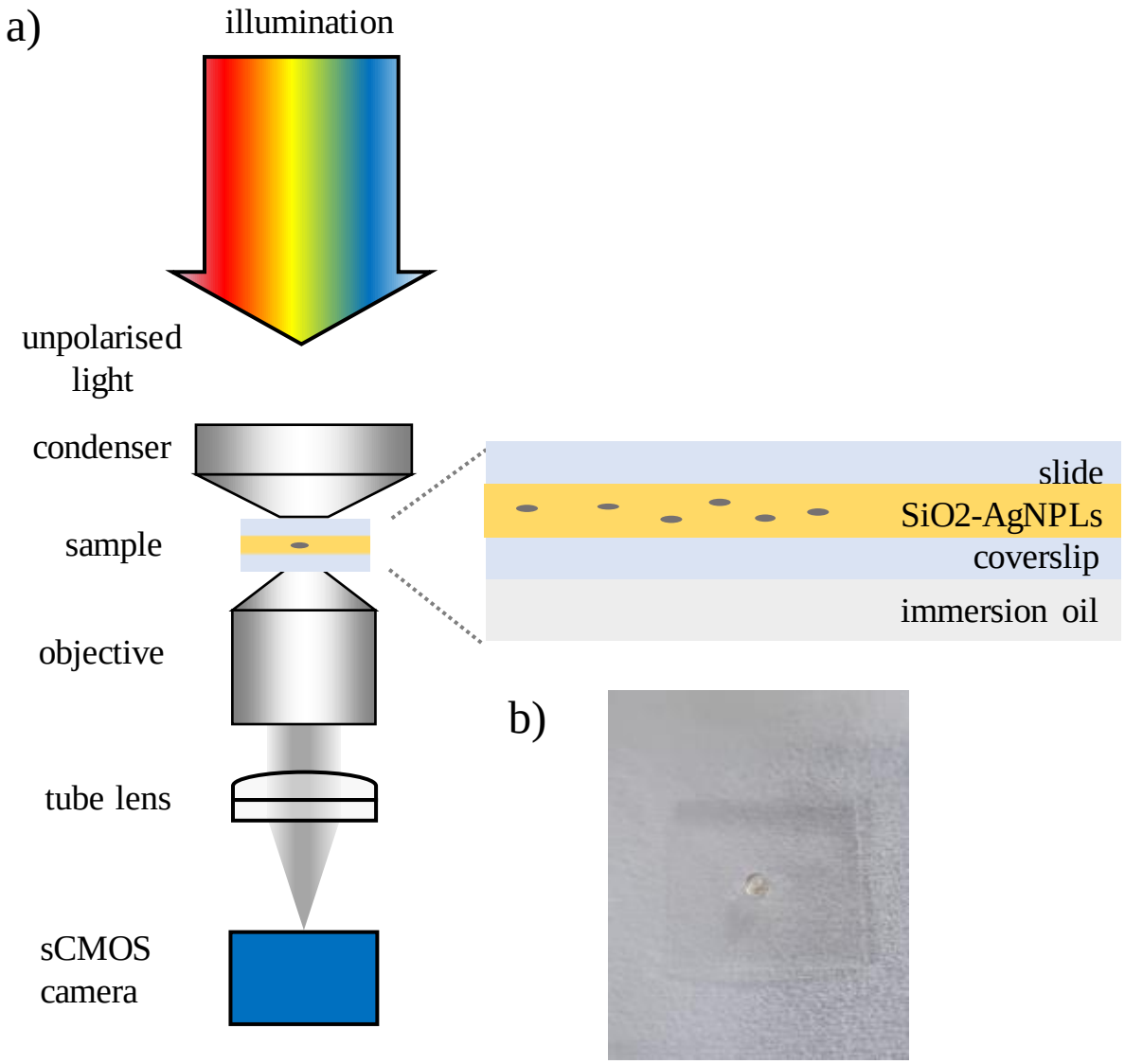

Figure 4.4: Sketch of microscopy setup with SiO_2-AgNPLs diffusing in viscous medium. a) The sample is illuminated with Köhler illumination, using a selection of different wavelengths. The image of the sample is then captured by a camera, employing a condenser with a numerical aperture (NA) of 1.34 and an immersion oil objective with a NA of 1.45. b) Picture of the coverslip with 10µL of a mixture of purified honey with SiO_2-AgNPLs.

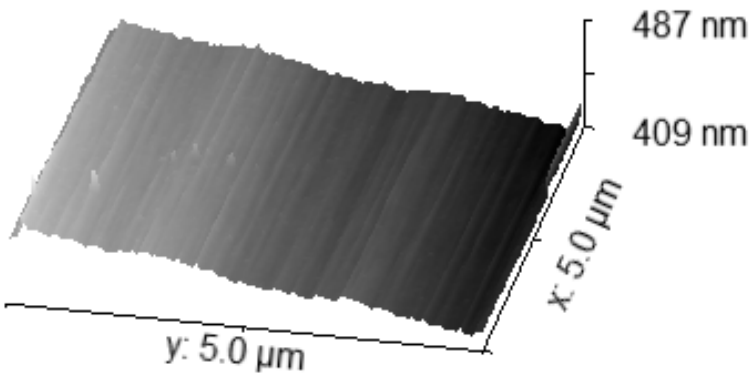

Figure 4.5: The AFM image displays a small area of the coverslip that has 40nm PVP-AgNPLs deposited on it. The image shows that the small area of the coverslip surface is tilted with a y scale, and the surface topography is shown as rough. The images are square, with square pixels of 128 pixels over 5 µm, as indicated.

4.3 Measuring $\sigma_{\mathbf{ext}}$ for SiO_2-AgNPLs in honey

As previously mentioned, a sample of 10 µm thickness was prepared. Measurements were made at a depth of 5 µm within the honey layer. Imaging at the middle of the sample thickness minimized interference arising from particles, debris, or structural anomalies in the surfaces above or below the sample. It was found that the sample's thickness varies across various areas. Therefore, precautions have been taken to select sections with a thickness of at least around 10 micrometers to prevent any two inner glass surfaces interference that may occur as a result. This type of sample was measured in the same steps as explained in the section 2.4.4. Unpolarised light was employed for this particular measurement. Table 4.1 provides the exposure times used to record images for each illumination wavelength. The exposure time was adjusted for each wavelength to account for the varying wavelength response for the camera and the emission spectrum of the lamp. In Chapter 3, polarisation-resolved measurements using both linear and radial polarisers were made on particles with fixed positions in the sample. Here, measurements were made on particles moving within a viscous medium. The experimental references were captured using the shifted-reference method as previously discussed in Section 2.4.5. In general, a sample under these conditions on the microscope can experience time-dependent drift on the order of a few micrometres per hour. Normally, this drift is detected by the in-house developed Extinction Suite data analysis software via a custom pattern recognition algorithm, which finds constellations of particles in the image and registers the position of the constellation over time. However, this becomes challenging when individual particles present size- and shape-dependent motion in their environment, since any pattern of particles changes over time. A further update to the software to allow for a more complicated individual particle tracking analysis in an automated way will be implemented in the future. In the short term, Dr. Lukas Payne updated the Extinction Suite software to provide a manual single particle selection procedure. One at a time, the user chooses single, well-isolated particles, where we define well-isolated such that for any ant two particles their centre PSF are at least $2r_i$ apart (as clarified in section 2.4.4).

Table 4.1: Exposure time in extinction microscopy for each wavelength for SiO_2-AgNPLs diffusing in honey.

λ (nm)	τ_e (ms)
500	2.5
550	2.05
600	1.64
650	1.62
700	1.74
750	2.5

For each selected particle, the measurement area is then manually chosen to be the smallest region that includes both the bright and dark PSF of the particle, as obtained using the shifted-reference method, over the entire time-series, including all illumination wavelengths. Notably, the area must be large enough to account for the increase in the effective area of the PSF in cases where Brownian motion occurs in the axial direction, resulting in a slight defocus. The different effects of Brownian motion can be seen in the same field of view in Fig. 4.6, where group A moved approximately 3 pixels laterally, group B moved axially resulting in a slight defocus, and group C exhibited no measurable motion on the same time scale (19 s). The manual selection procedure thus provides a basic way to make use of the automated analysis of Extinction Suite, while being free to account for multiple complexities arising from particle motion in a viscous medium. Fig. 4.7 shows the images of the PSF and the time-dependent σ_{ext} for a single SiO_2-AgNPL at each of the measurement wavelengths.

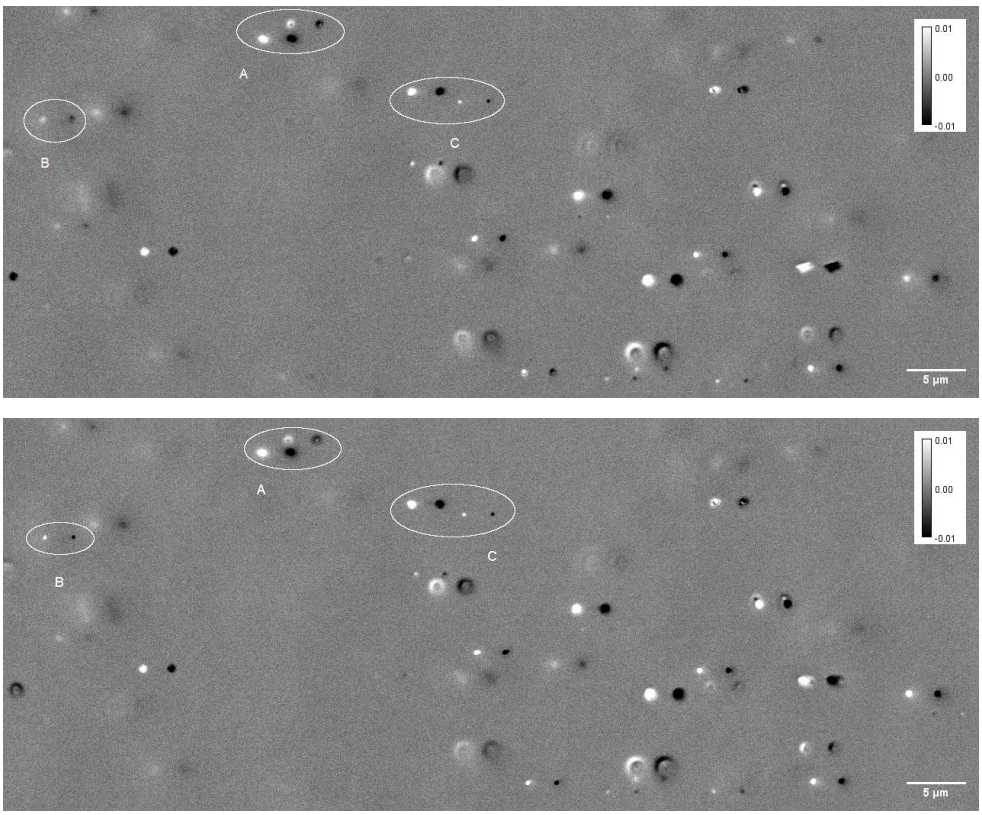

Figure 4.6: Extinction contrast image in the same FOV at two different measurement times (19 s) for SiO_2-AgNPLs in honey at 500 nm wavelength : The images show how SiO_2-AgNPLs particles behave differently when they are immersed in honey. These behaviours can be broken down into three groups: group (A) shows a lateral drift; group (B) shows a change in focus (longitudinal drift) over the measurement period; and group (c) shows no measurable change.

4.4 Cluster analysis

A cluster analysis of the cross-sections measured on SiO_2-AgNPLs moving in honey, as viscous medium, was carried out using the identical procedures described in section 3.2. Equation 4.12 shows the predictor used for this type of analysis.

$$\langle \sigma_i \rangle = \frac{1}{T} \sum_{j=1}^{T} \sigma_{i,j} \tag{4.11}$$

$$p = \frac{\langle \sigma_i \rangle}{\frac{1}{TW} \sum_{j=1}^{T} \sum_{i=1}^{W} \sigma_{i,j}} \tag{4.12}$$

i and j refer to the wavelength and time index, respectively. $<\sigma_i>$ is the average of the particle cross section over time, as defined in Eq.4.11. The predictor taken for this cluster analysis uses $<\sigma_i>$ normalised to the cross section averaged over the spectrum and time variables. The normalization factor (denominator in Eq.4.12) is particle dependent. It was found that eight groups gave the optimum particle separation for this analysis, producing meaningful predictor

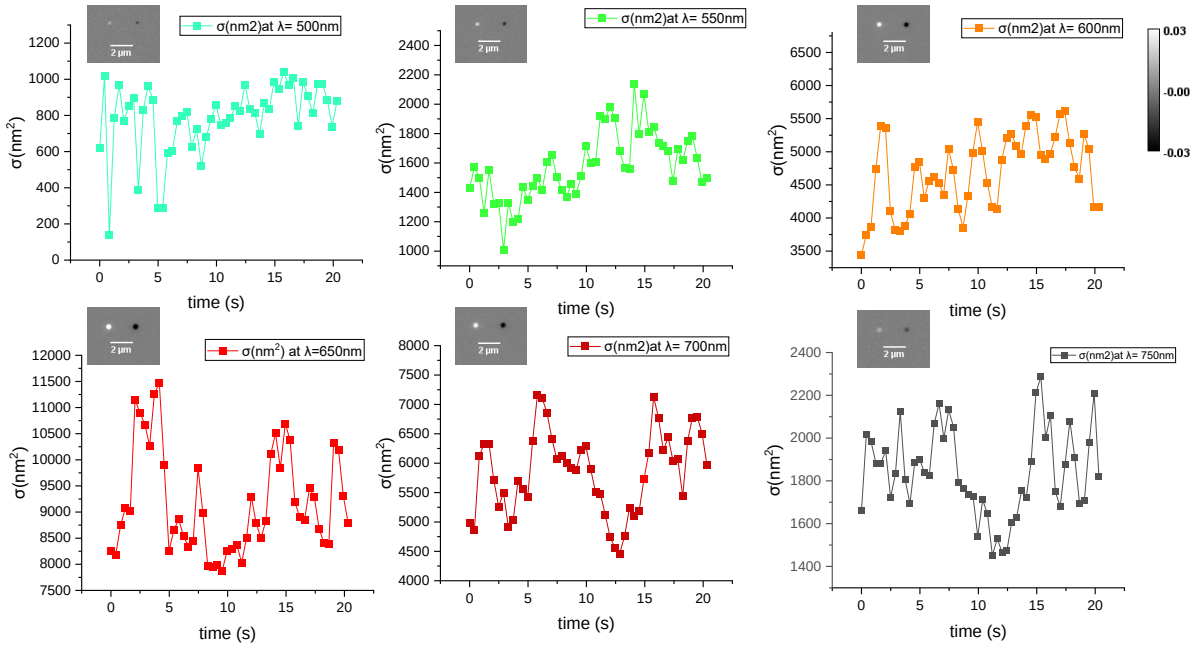

Figure 4.7: Extinction cross section versus time for a selected SiO_2-AgNPL at different wavelengths. The plots show how σ_{ext} changes with time, at different light wavelengths. The insets are extinction contrast images measured at the different time interval, the image at 500 nm refer to (3.318 s), 550 nm (3.732 s), 600 nm (1.659 s), 650 nm (0.415 s), 700nm (0.415 s) and 750nm (4.977 s). All images are greyscale, from -0.03 (black) to +0.03 (white), as indicated.

spectra, without over or under splitting the results. Fig. 4.8 displays the first and second principal components for the NP predictors, while the effect of changing the group number from 6 to 13 is shown in Fig. 4.9

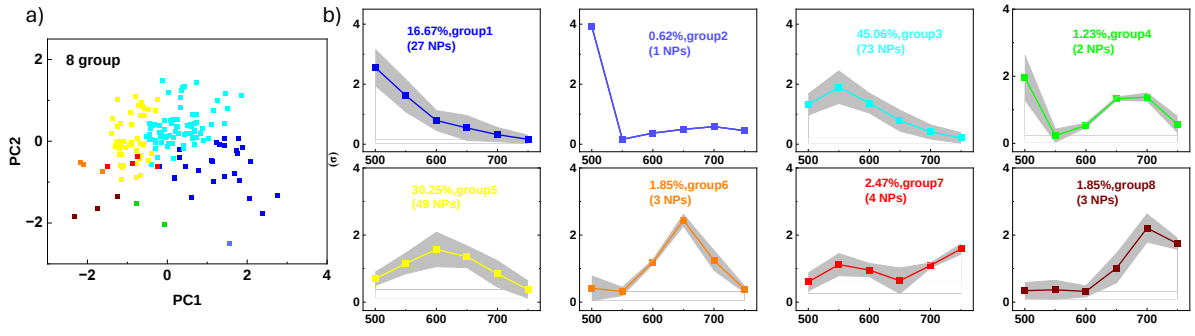

Figure 4.8: SiO_2-AgNPLs cluster analysis in viscous medium. a) First and second principal component values for the NP predictors in equation 4.12. The symbol colour represents 8 different groups. b) Predictor spectra for the 8 groups in (a). The symbols represent the mean, whereas the grey area represents the standard deviation over the SiO_2-AgNPLs in the group.The number of particles in each group is indicated in (b).

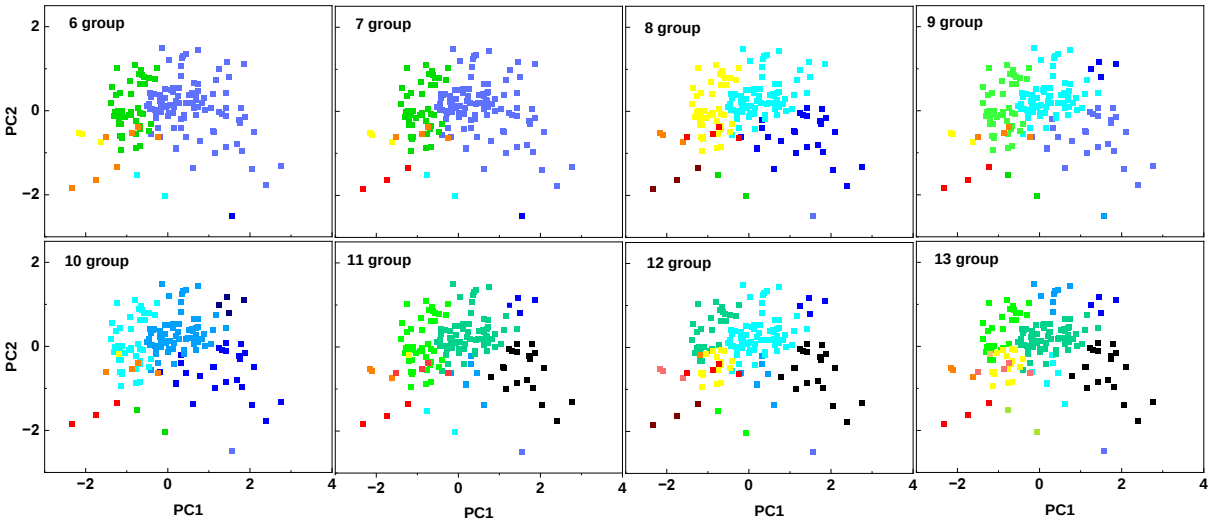

Figure 4.9: NP predictor first and second principal component for different number of groups for SiO_2-AgNPLs in viscous medium . Cluster analyses as in Fig. 4.8, using different number of groups from 6 to 13, as indicated. SiO_2-AgNPLs in different groups have differently coloured symbols.

When comparing the results in Fig. 4.8 with the analysis for nominally identical SiO_2-AgNPLs deposited on a surface and analysed using the method described in Chapter 3, namely averaging over the particle orientation "post-acquisition" (see Fig. 3.16 and Fig. 3.18), we can make the following considerations: Qualitatively, the spectra of the predictors are similar; however, the separation in Fig. 4.8 is less well defined compared to what shown in Fig. 3.16 and Fig. 3.18. In Fig. 4.8, we see that most particles cluster around groups 1, 3, and 6, with the other groups containing only a few particles. Conversely, the separation shown in (see Fig. 3.16 and Fig. 3.18 was more systematic, both in terms of spectral shapes and grouping of particles in the various clusters. A possible explanation for this difference could be an insufficient averaging over the particle orientation while particles are diffusing in honey over the measurement time in the experiment. Notably, the total observation time in these experiments had to be limited, to avoid particles diffusing too much out of focus in the volume. Indeed, this was the initial motivation for preparing samples with a thin (less than 1 mm) layer of honey, as discussed in Section 4.2.2.3, so that particles could be maintained within the depth of focus over long observation periods (eventually limited by set-up drifts). However, this approach resulted in most particles becoming attached to the glass surface, hence it could not be used. In the future, one could explore surface treatments to minimise this attachment so that a thin layer of honey can be used. Complementary to the cluster analysis shown in Fig. 4.8, the following quantities were examined:

$$C_i(\tau) = \frac{\langle (\sigma_{i,t} - \langle \sigma_i \rangle)(\sigma_{i,t+\tau} - \langle \sigma_i \rangle) \rangle}{\mathrm{var}(\sigma_i)} \quad ; \quad C_i(\tau_i) = \frac{1}{2} \tag{4.13}$$

$$\langle \sigma \rangle = \frac{1}{W} \sum_i \langle \sigma_i \rangle \tag{4.14}$$

where $C_i(\tau)$ is a time autocorrelation function, having a half-life τ_i, and $\langle\sigma\rangle$ is the cross-section averaged over all wavelengths. In equation 4.13, var is the variance of σ_i fluctuating in time. In Fig. 4.10 (a) shows the relation (on a logarithmic scale) between $\langle\sigma\rangle$ and the average of τ_i over all wavelengths $\langle\tau\rangle = \frac{1}{W}\sum_i \tau_i$. In Fig. 4.10, the solid line signifies a linear dependence, while the dashed line shows a quadratic dependence, namely $\langle\sigma\rangle \propto \langle\tau\rangle$ (solid line), and $\langle\sigma\rangle \propto \langle\tau\rangle^2$ (dashed line). These dependencies separate the cases of particles having a cross section dominated by light absorption, hence scaling with the particle volume, from those dominated by scattering, scaling with the square of the volume. In fact, the quantity $\langle\tau\rangle$ represents an average rotational diffusion time-constant which, according to the law of Brownian diffusion, is itself proportional to the inverse of the rotational diffusion constant, hence scaling with the particle volume (see Eq.4.1). Therefore, Fig. 4.10 offers a complementary way to separate individual particles, based on their size, with large particles following the quadratic scaling, and smaller particles following the linear scaling behaviour.

Another set of quantities were calculated as follows:

$$\langle\lambda\rangle = \frac{\sum_i \lambda_i \langle\sigma_i\rangle}{\sum_i \langle\sigma_i\rangle} \tag{4.15}$$

$$\Delta\sigma_1 = \frac{1}{\langle\sigma\rangle}\sqrt{\frac{1}{W}\sum_i \mathrm{var}(\sigma_i)} \tag{4.16}$$

$\Delta\sigma_1$ is a wavelength-averaged normalised standard deviation, and can be considered as a reporter of the particle asymmetry, related to the degree of cross-section temporal fluctuation while the particle rotates. It should be zero for spherical particles, while significantly different from zero for asymmetric particles such as plates and rods.
Fig. 4.10 (b) shows the relationship between $\Delta\sigma_1$ and $<\lambda>$. Interestingly, we see that particles correlating with groups 6,7 and 8, which are those having the most red-shifted cross-section resonance wavelength, have a non-zero $\Delta\sigma_1$ with a well-defined value, hence are likely to be nanoplates.

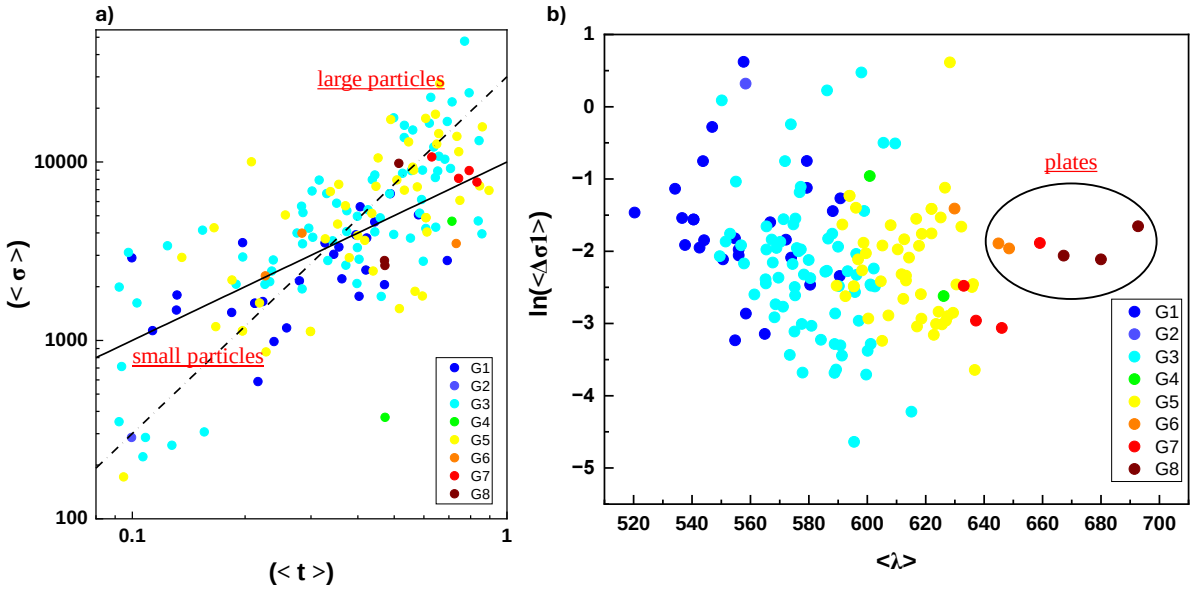

Figure 4.10: Complementary metrics of particle size and shape for SiO_2-AgNPL rotating in a viscous medium.a) Relation between the average cross section and the rotation time constant (see text and Eq.4.13 and 4.14) where the solid line shows a linear dependence and the dash line is a quadratic dependence. b) Relation between the mean standard deviation defined in Eq.4.16 and the mean wavelength defined in Eq.4.15.

Chapter 5

Correlating Optical Extinction with Atomic Force Microscopy (AFM) results

Atomic force microscopy (AFM) is a highly effective method for quantifying the size, shape, morphology, and thickness of NPs [147] [148]. AFM provides a topographic readout with height resolution in the nanometre range, and it is therefore particularly suited to characterise thin nanoplates such as the ones studied in this thesis. A correlative approach between AFM and optical extinction microscopy described in this Chapter. The goal was to develop an experimental pipeline whereby the same individual AgNPL is measured with both methods, to cross-validate the morphometric analysis of the optical extinction technique by direct comparison with AFM. For this study, we used the PVP-coated AgNPLs (see Materials and Methods). Two different sizes of PVP-AgNPLs were investigated, with nominal 40 nm and 70 nm edge length. The optical extinction microscopy of these nanoparticles is described in detail in Chapter 3. Here, we focus on the work carried out to correlate the same nanoparticle using AFM.

5.1 AFM sample preparation

Samples consisting of AgNPLs were deposited onto a glass surface using the procedures outlined in the section 2.3.2, except for the last two steps, namely applying silicon oil and pressing the cover slip with the glass slide. This is because, for AFM, nanoparticles need to be accessible to the AFM tip, and therefore were kept in air, without surrounding oil nor glass cover. Different preparation processes of the nanoparticle solution were investigated, as described below, with the aim to minimise particle aggregation and maximise the presence of well-defined triangular AgNPLs on the glass surface of mixture was treated in several ways because the AFM results for AFM inspection.

- (A) PVP-AgNPLs were diluted from the stock at the desired concentration and deposited using the wet-casting method (see Material and Methods, section 2.3.2) on the clean cover slips, without any additional processing.

- (B) To separate bigger from smaller particles, a centrifugation step was applied. A solution of 1mL of 40 nm PVP-AgNPLs (2.9×10^{11}Nps /mL see section 2.3.2) was centrifuged at 5000 rpm for 10 minutes and 0.99 ml supernatant was replacing with 5mM Borate buffer [149].

- (C) The same step (B) was used, however, the supernatant was substituted with a 5mM Borate buffer including Polyvinylpyrrolidone (PVP) at a concentration of 10^{-5} g/ml. PVP was added to the buffer to enhance steric stability and preventing PVP from coming out of the silver nanoparticle coating.
- (D) The same step (B) was used, however, the supernatant was substituted with a 5 mM Borate buffer including PVP at a concentration of 10^{-6} g/ml. This was tested to minimise surface deposits originating from PVP and causing an unwanted background in AFM and extinction analysis.
- (E) The same step (C) was used, but the mixture was sonicated for 30 min before and after centrifugation process, to help preventing/reducing aggregation. It is important to mention that, for all the aforementioned stages, the coverslips were thoroughly cleaned using hydrogen peroxide, as outlined in section 2.3.1.
- (F) here, the diluted the stock solution, as described in 2.3.2, was used, involving PVP at a concentration of 10^{-5} g/ml in a 5 mM Borate buffer, without any centrifugation or sonication process. During this stage, the coverslips were cleaned using the method described in section 2.3.1, however excluding the hydrogen peroxide step. This step of glass cleaning is known to increase the surface polarity / hydrophilicity. Since the nanoparticles of interest are PVP-coated, here we wanted to explore whether a less polar surface would facilitate the stable attachment of these particles, through the interaction with the PVP layer (which has a reduced polarity compared to water). Upon implementing this procedure, it became evident that hydrogen peroxide plays a crucial role in eliminating surface impurities, and removing it from the glass cleaning steps was not helpful, as shown in Fig. 5.1 (B) .

Examples of results for each of the above steps are shown in Fig. 5.2 and Fig. 5.1 where a collection of AFM pictures are displayed. The main outcomes of this investigation were that 1) nominal 40nm AgNPLs had a variety of in-plane shapes, often non-triangular, 2) on several occasions a feature was observed on the particle's edge (see e.g. Fig. 5.2A, and Fig. 5.1 #5, #6). This feature was initially attributed to small particles attached to bigger ones. However, this interpretation was not consistent with the dependence observed by changing the preparation steps (for example, step B was not leading to an improved outcome compared to A). Most likely, this feature is due to the gradual formation of Ag_2S tarnish from Ag, which occurs due to the presence of trace amounts of sulphur in the solvents, water, or the surrounding atmosphere [129][150]. Furthermore, the time factor may have influenced this contamination process, as the sample was used over the course of 1 year (reaching the limit of the manufacture recommended shelf life), while testing the various preparation steps. Generally, the variety of PVP-AgNPLs shapes observed in AFM align with our expectations from optical extinction microscopy (Chapter 3) and with the TEM results mentioned in section 2.4.7.

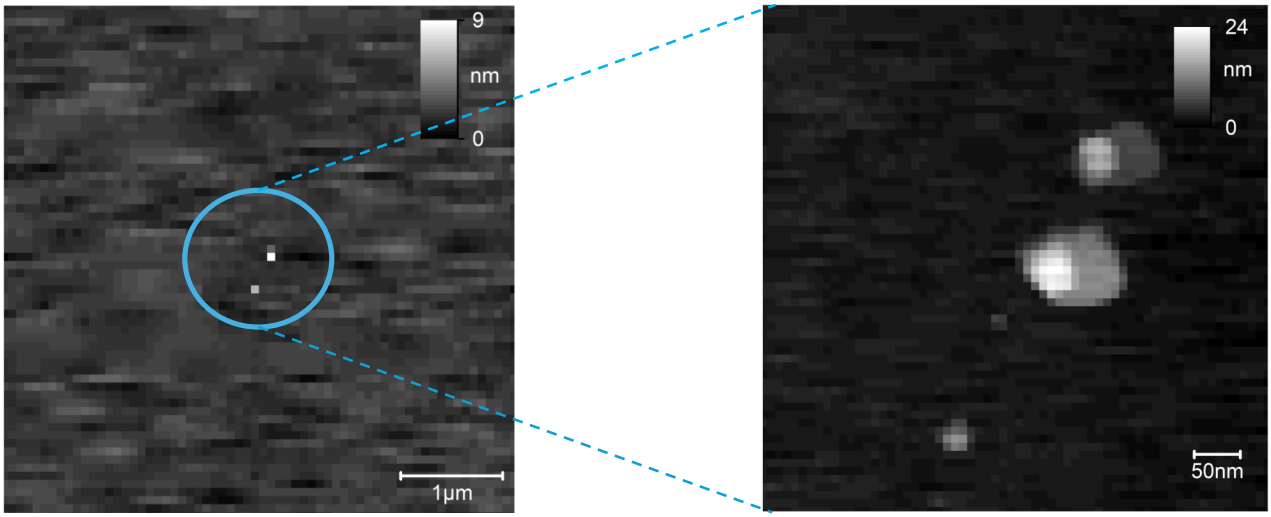

Figure 5.1: Atomic force microscopy images of selected 40 nm PVP-AgNPLs deposited on the coverslip. The samples topography is shown with scale bars and height in the gray scale as indicated. All images are square with square pixels. (A) shows examples of particles deposited using method A, where clean coverslips (using hydrogen peroxide) are used without any additional processing (centrifugation). The left panel consists of 128 pixels over 5µm, and the right one has 128 pixels over 548nm. (B) shows examples of particle deposited using method F. The left panel consists of 128 pixels over 350nm , the middle one has 128 pixels over 194nm, and the right one has 128 pixels over

.

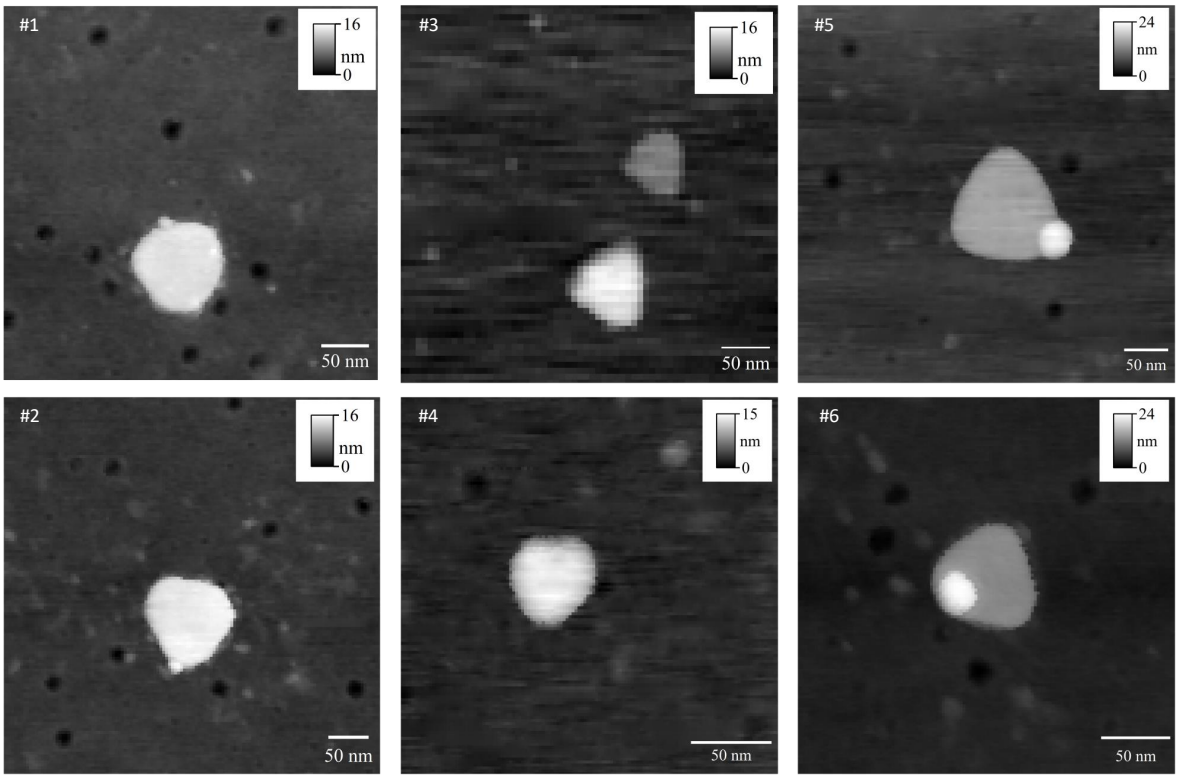

Figure 5.2: Atomic force microscopy images of selected 40nm PVP-AgNPLs deposited on the coverslip. The sample topography is shown with scale bars and height in the gray scale as indicated. All images are square with square pixels as follows: #1 128 pixels over 391 nm; #2 128 pixels over 469 nm; #3 64 pixels over 391 nm; #4 128 pixels over 234 nm; #5 128 pixels over 430 nm; #6 128 pixels over 273 nm. The samples were made using the following preparation steps (see text): #3 step A; #1,#2,#6 step B; #4,#5: Step C and D.

For further AFM studies, 70 nm-sized PVP-AgNPLs were subsequently utilised. These larger particles are better visible in both AFM (being well above the ~ 10 nm in-plane spatial resolution of the AFM tip) and optical extinction. After 30 minutes of sonication, 1 mL of 5 mM of borate buffer and 10^{-5} PVP-AgNPLs ($2.9 * 10^{11}$ NPs/mL see section 2.3.2) with a 70 nm size was subjected to centrifugation to remove smaller nanoparticles and facilitate the sedimentation of larger ones. After 15 minutes of centrifugation at 5000 rcf, 0.99 mL of the supernatant was replaced. The mixture was sonicated again for 30 min to separate the particle and avoid the aggregation of the particles. Then finally the sample was prepared with wet casting method. Fig. 5.3 illustrates a selection of AFM images of 70 nm-sized PVP-AgNPLs with clear background. A much smaller proportion of small features/NPs is present compared to when 40 nm PVP-AgNPLs were utilized, allowing for the measurement of a large number of PVP-AgNPLs with different sizes and shapes.

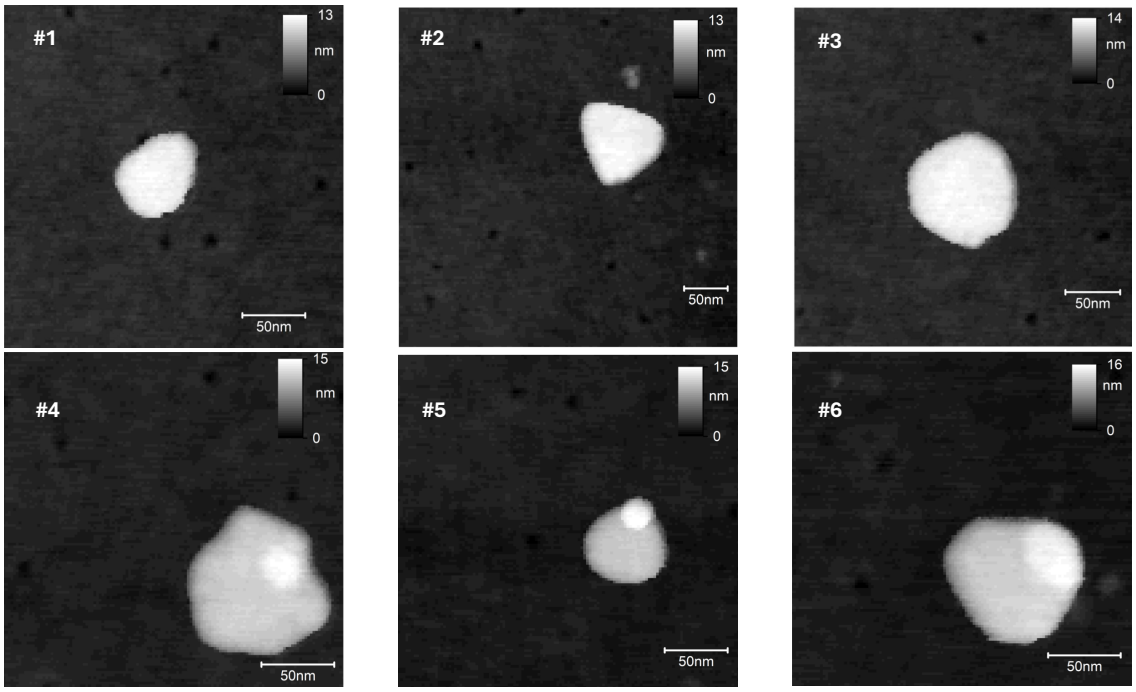

Figure 5.3: AFM images of selected 70nm PVP-AgNPLs deposited on the coverslip. The sample topography is shown with scale bars and height in the gray scale as indicated. All images are square with square pixels as follows: #1 128 pixels over 273 nm; #2 128 pixels over 391 nm; #3 128 pixels over 313 nm; #4 128 pixels over 234 nm; #5 128 pixels over 273 nm; #6 128 pixels over 234 nm.

5.2 Correlating Optical Extinction microscopy with AFM

After having measured individual PVP-AgNPLs using AFM, particles were covered with 25 µL of silicon oil, then a glass slide was placed on top and gently pushed to reduce the oil's thickness. Any extra oil on the coverslip's borders was removed using cleanroom tissue soaked in acetone. Finally, the coverslip edges were sealed with nail varnish to enclose the sample and imaged with optical extinction. The AFM microscopy technique and the optical extinction technique have different fields of view sizes, whereas the optical extinction microscopy captures a larger area than the AFM technique. Due to this distinction, correlating PVP-AgNPLs observed with both techniques is challenging. To overcome these challenges,a protocol was designed to establish fiducial markers to be imaged with both methods. An image transformation software was then employed. The software was designed by Dr.Francesco Masia. The software applies a linear transformation matrix to transform an image (A) into the coordinate system of a different image (B), and vice versa, by comparing the coordinates of objects in both images. The system utilizes coordinates provided by the user and applies transformations to them. To use this transformation software, it is essential to have three objects with known coordinates in both images. For this purpose, three features were made that can be easily identified using both optical extinction and the AFM technique. In the first experiment, the features consisted of three distinct crosses scratched on the coverslip surface using a glass cutter tool, as depicted in figure 5.4.

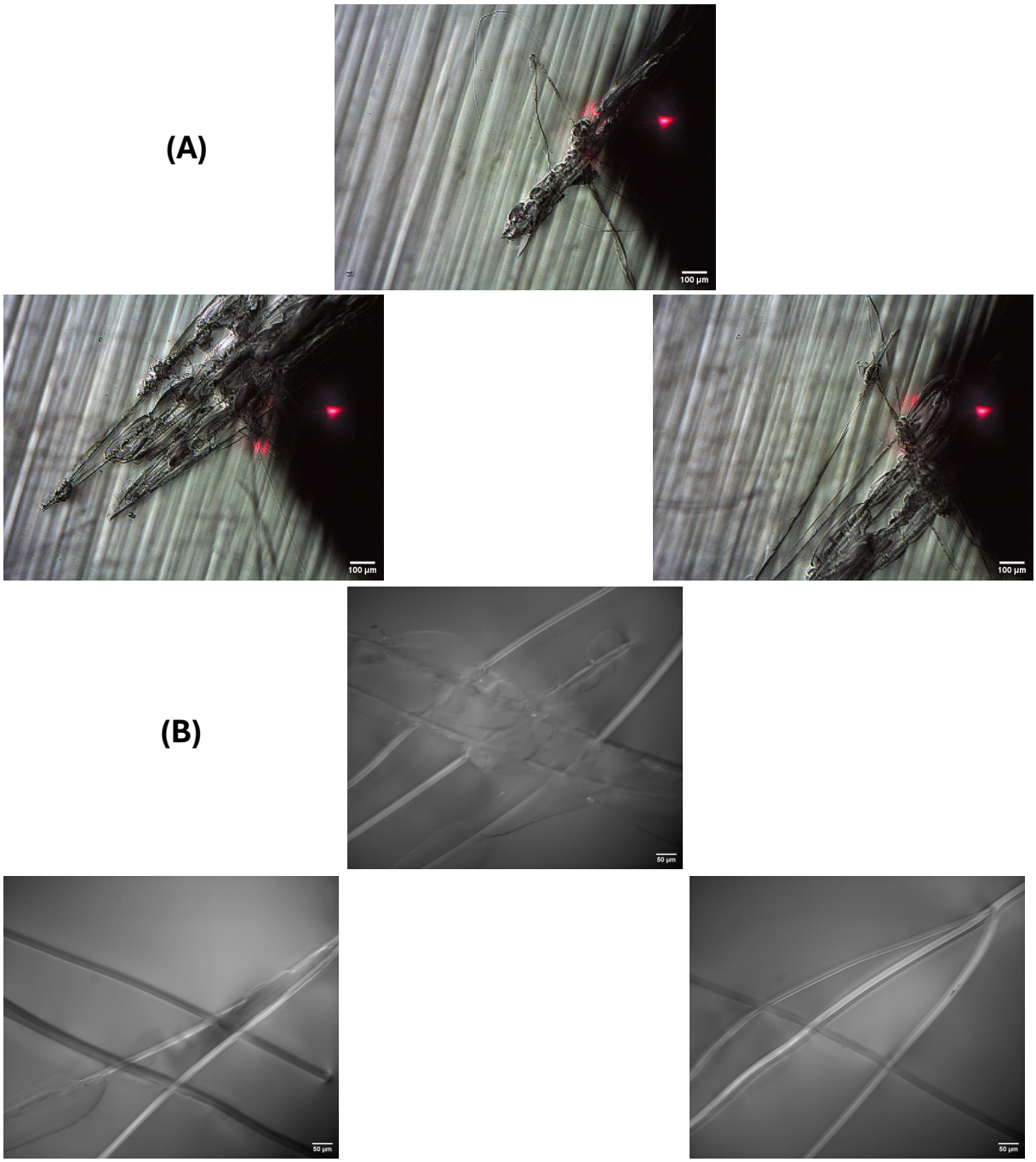

Figure 5.4: Three objectives (scratch crosses) identified in both AFM and optical extinction microscopy techniques. (A) Images showing the three cross shapes that were made by using a glass cutter tool with a distance of 2.5 mm between each other; each image has 640x480 pixel dimensions, and was acquired using a light reflection microscope available in the AFM instrument; A quad photodetector detects the beam emitted by the laser diode (1.0 mW max at 670 nm) as it reflects off the cantilever (B) transmission images show the same crosses in (A) acquired with the optical extinction microscope. These transformation images were captured by using a 20x 0.75 NA objective lens and a 1x tube lens.

Following the creation of these scratches and the subsequent measurement of the sample us-

ing AFM, silicon oil is introduced to facilitate optical extinction measurements, by minimising refractive index contrast with the glass surface. However, while beneficial to minimise background, this optical "clearing" also meant that the scratches on the glass surface became less visible. The scratches also exhibited a structural pattern that was significantly different when observed under the light reflection microscope available in the AFM instrument compared to the optical extinction microscope, see Fig. 5.4. Consequently, it was challenging to locate their exact position using the two microscopes. An alternative approach was then followed, which involved the application of a silver paint to create three distinct dots utilizing Leitsilber L100, a silver conductive coating. The silver paste was placed at three distinct locations, forming vertices of a triangle, with a separation of 2.5 mm between each point. This was achieved by utilizing a wooden cocktail stick. The comparison between images of these dots using the light microscope in the AFM instrument and the optical extinction microscope is illustrated in Fig. 5.5.

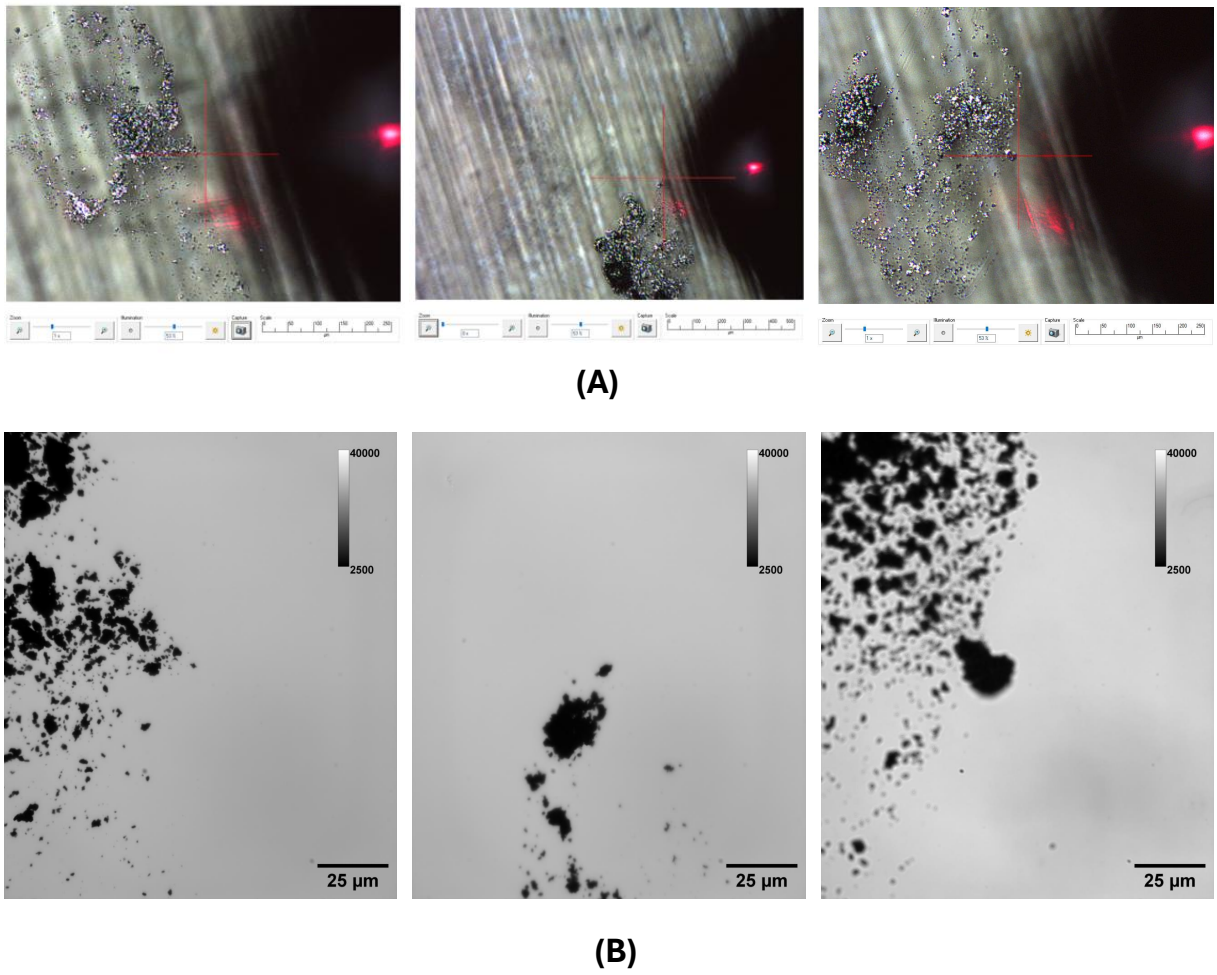

Figure 5.5: Three objects (silver paint "dots") were identified in both AFM and optical extinction microscopy techniques. (A) The three images represented the three "dots" that were made by using a silver conductive paint and a wooden cocktail stick, with a distance of 2.5 mm between each other. These images were acquired using a light reflection microscope available in the AFM instrument.(B) Three transmission images showing the same silver paint objects in (A) using the optical extinction microscopy technique. These transmission images were captured by using a 100x 1.45 NA objective lens and a 1x tube lens.

To calculate the matrix parameters that transform an AFM image into the coordinates of an optical extinction, we used the coordinates of the silver paint "dots" measured using both methods. The light reflection microscopy available in the AFM microscope was used to find the dots. The AFM-captured images indicated that the silver "dot" is an aggregate of spots with a different pattern. We used the AFM tips (An automated motorised stage, when linked with the advanced Automet software, enables precise nanoscale measurements to be conducted at specific user-defined positions) to specify the centre of a side-section reflection image of these "dots," keeping it away from the silver paint to prevent damage to the tip. For each "dot," a clear pattern was chosen in order to facilitate the process of finding this pattern in the optical extinction microscope. After finding the same pattern with the optical extinction microscope, which is placed in the centre of the images, the coordinates of these images were used as in the software.

Fig. 5.6(A) shows an example of coordinates measured with AFM and optical extinction for a selected feature identified at the edge of a silver paint "dot", while Fig. 5.6 (B) represents the screenshot of the two input files supplied by the user, containing the coordinates of the same objects in the respective AFM and optical extinction images. The order of the dots in the two files must be the same. The transformation parameters to overlap coordinates between the images include shear, scaling, rotation, and translation. The software allows the user to choose which parameters are being adjusted. For example, objects coming from different images might need a transformation that accounts for image rotation, translation, and scaling but not a change in shear. This was our case where the shear was excluded. The transformed coordinates of objects from image A into the reference system of image B are shown by the software, and can be checked by the user (Fig. 5.6(C)), to decide if the transformation found is appropriate or the procedure needs to be revised due to e.g. errors in the choice of input coordinates. Fig. 5.6(D) shows an example of saved output file with the coordinates situated within the field of view centre for the optical extinction microscopy image. extinction microscopy image. Fig. 5.6(E) is a picture of the sample stage control micrometer screws (in x and y direction) in the microscopes, used to find the coordinates for the area to be measured.

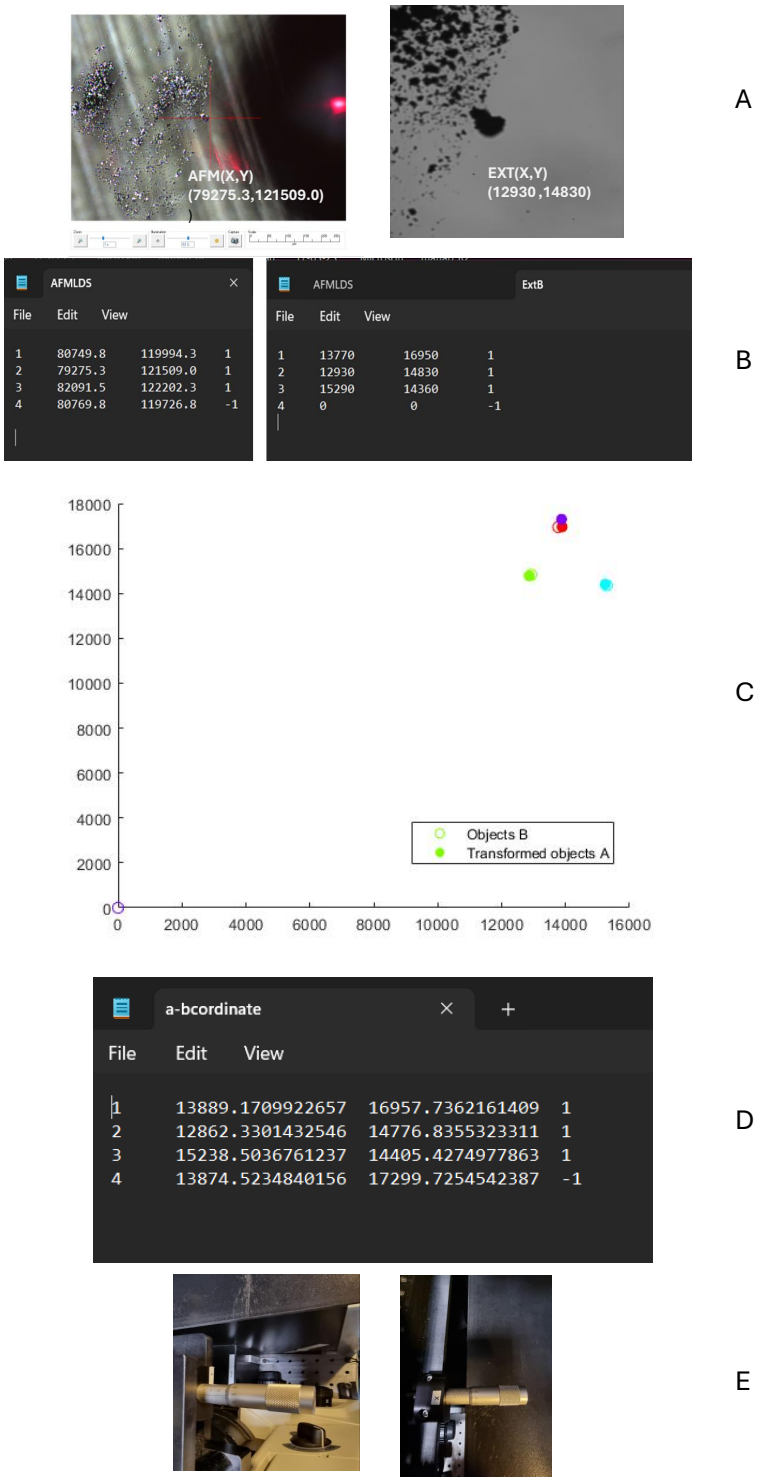

Figure 5.6: Workflow between AFM and optical extinction microscopy. (A) The coordinates of a feature in a silver paint "dot" used as fiducial marker are identified in both AFM and optical extinction microscopy techniques. (B) Screenshot of two input files with coordinates supplied. (C) Overlay of the transformed coordinates for the entered points. (D) Screenshot of the results (transformed coordinates). (E) The sample stage micrometre control screws were used to find the coordinates for an area be measured with optical extinction microscope.

In our study, we conducted AFM scans of multiple regions measuring 5 µm in length, which were then stitched together to create a large area overview. Fig. 5.7 shows an example of these tiles that formed the measured FOV. Each tile is square, with 128 pixels over 5 µm. For each tile, the z-scale is indicated, from zero as the minimum value to a maximum value shown on each image. The total FOV area is 45 µm wide and 20 µm high. The AFM measurements show the diversity in shapes and sizes of the 70 nm PVP-AgNPLs investigated, which include triangle and hexagonal shapes as shown in Fig. 5.3, consistent with the TEM images provided by the manufacturer company, see Fig. 2.2. The AFM measurements provide a thickness distribution of the PVP-AgNPLs, as illustrated in Fig. 5.7(B) .

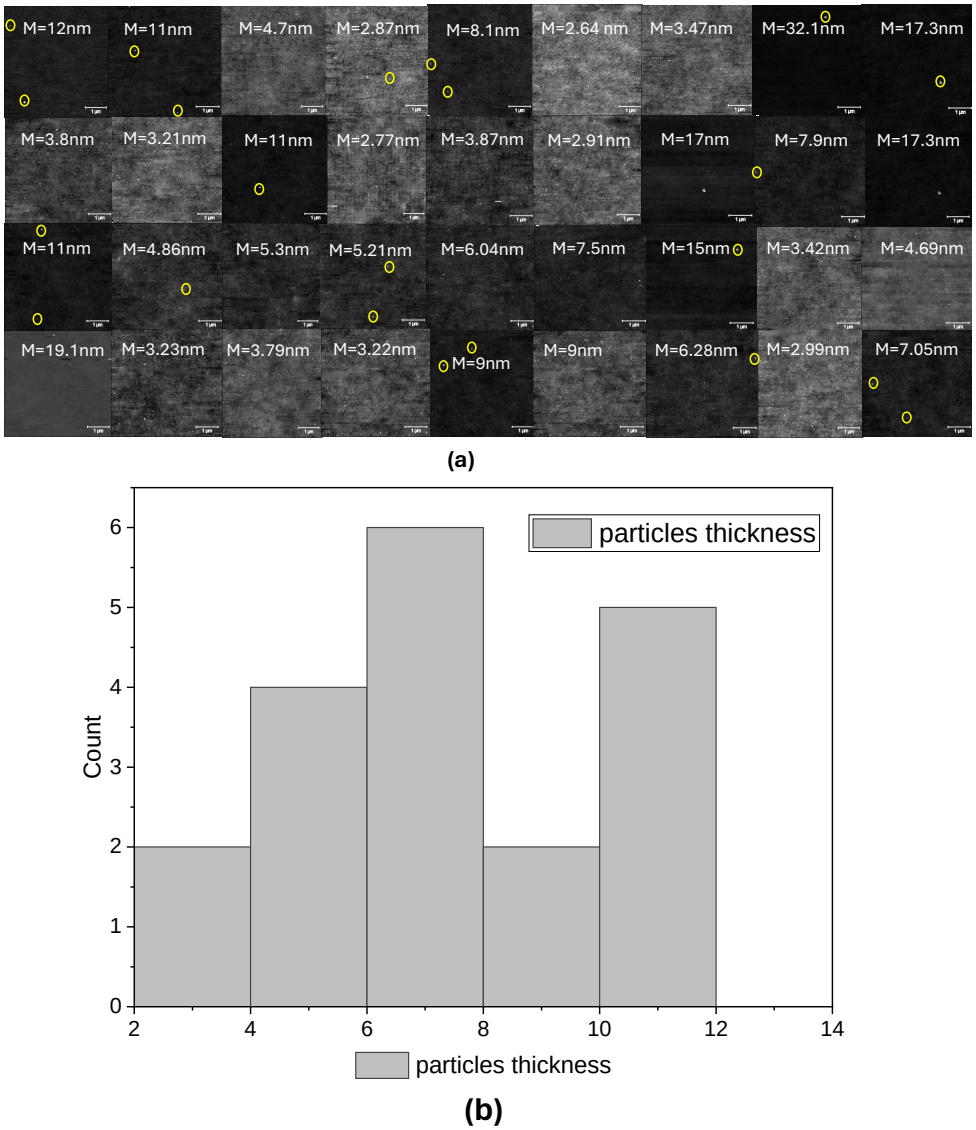

Figure 5.7: AFM overview for one field of view of 70nm PVP-AgNPLs. (a) The sample topography is shown with scale bars and height in the gray scale, as indicated. All images are square, with square 128 pixels over 5 µm. For all images, z-scales are indicates starting from zero as min value with the maximum value shown on each image. The particles are marked by yellow circles (b) Thickness statistics of 70nm PVP-AgNPLs nanoparticles, determined using AFM.

With a wider field of view, the extinction images were captured in the same location as the AFM images; the same area was found by applying the image transformation software, see Fig. 5.8.

Information regarding the optical extinction image acquisition settings are provided in the caption of Fig.5.8. The collection and analysis of the optical extinction data followed the same processes as described in Section 2.4.4. The exposure time was 15ms for all the used filters. The separation of the bright-dark spot pairs is 2 μm for this set of measurements. Despite having found the same area in both images, we could not recognise a common nanoparticle pattern, and thus unambiguously assign the same AgNPL in both measurements. A possible reason for this lack of correlation might be the addition of silicon oil onto the sample. This was applied after the AFM, in order to embed the particles in a medium which minimises optical background, important for optical extinction analysis. Adding silicon oil might have moved the AgNPLs from their original position observed under AFM, considering that the particle adhesion to the glass surface was achieved via the wet-casting method, and not through a strong covalent bond.

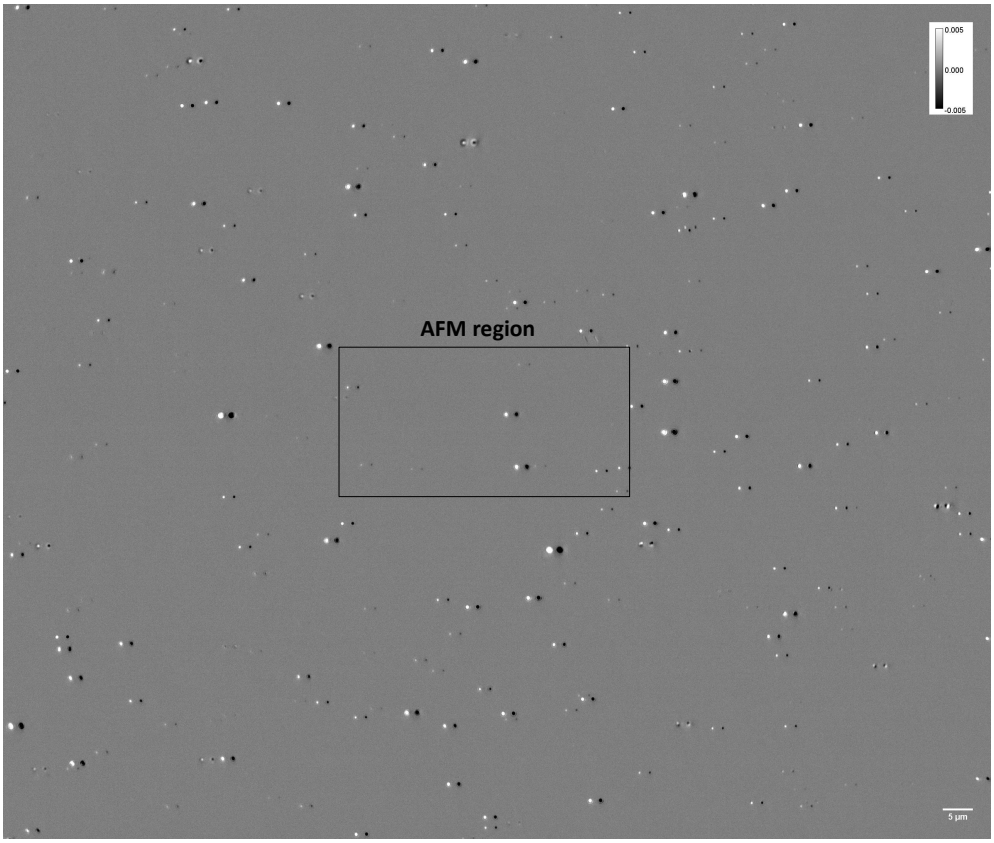

Figure 5.8: Extinction of 70nm PVP-AgNPLs field of view containing the small AFM area shown in Fig. 5.7 . Extinction contrast image (Δ_1) measured using the polariser angle $\gamma_P = 0°$ and $\lambda = 650\,nm$. The image consists of 2560 × 2160 pixels with a pixel size of 64.1 nm. Image greyscale ranges from -0.005 to 0.005, as indicated

.

Fig. 5.9 displays a summary of the optical extinction analysis carried out on these samples. The values of σ_L, σ_R, and α are shown, obtained at 500 nm and 700 nm wavelength. The outcomes are comparable to those seen for the PVP-AgNPLs of nominal 40 nm size in Fig. 3.3. In line with the AFM results and TEM results, which are displayed in Fig. 5.3 and Fig. 2.2, respectively, the measured cross-section distributions reveal a range of sizes and shapes. As

discussed previously, the ratio between σ_L and σ_R can be used to identify the axial to in-plane aspect ratio, with spherical particles having σ_R=σ_L and plates exhibiting σ_R< σ_L (see lines in Fig. 5.9 (a)). The values of α in Fig. 5.9 (b) indicate the in-plane particle asymmetry, with triangular or hexagonal plates having α= 0, and rods having α up to 1.

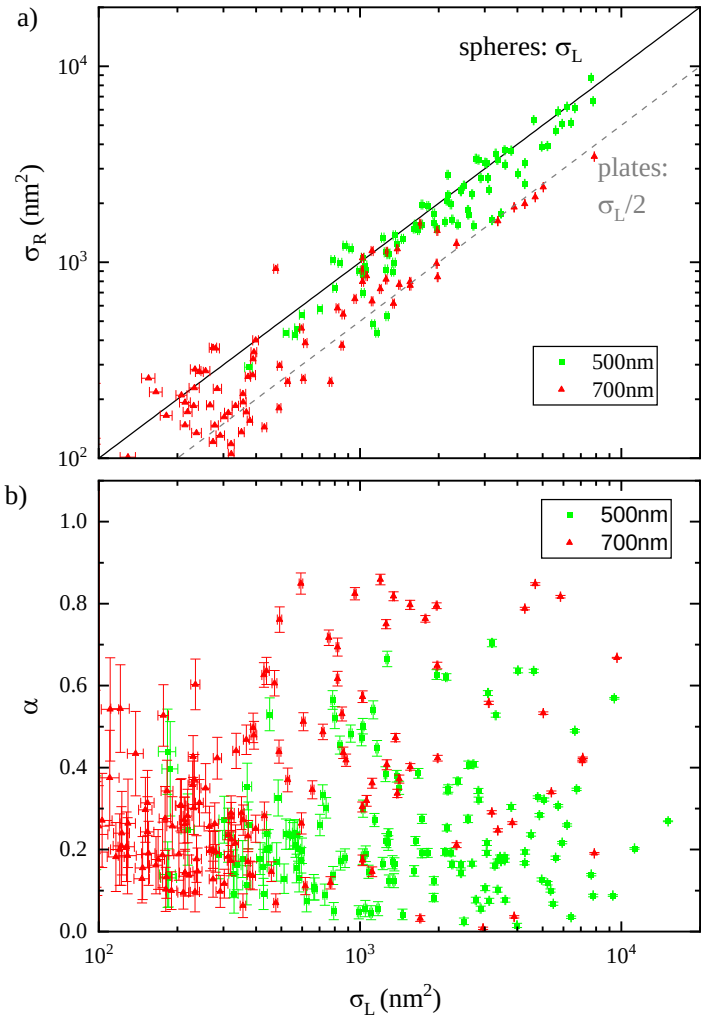

Figure 5.9: Summary of extinction cross-section values for 157 individual 70nm PVP-AgNPLs. The values obtained with the radial polariser are denoted as σ_R, whereas the values obtained with the linear polariser are represented by the fit parameters σ_L and α. a) The comparison between σ_R and σ_L for 82 individual 70 nm PVP-AgNPLs. The expected values of σ_L for spherical particles and 0.5 σ_L for plates are displayed for of comparison. b) The comparison between α and σ_L for 157 individual 70 nm PVP-AgNPLs. Green symbols correspond to a wavelength of 500 nm, whereas red symbols correspond to a wavelength of 700 nm. Error bars represent the level of uncertainty resulting from shot noise in the measurements.

By repeating the same procedures, another sample was prepared and measured using both AFM and extinction techniques. Fig. 5.10 presents the values of σ_L and α resulting from the analysis on this sample. In this particular set of data, the values of σ_R were found to be negative (hence not shown). A possible explanation for this unphysical value might be related to the significant light scattering exhibited by the AgNPLs of nominal 70nm size, compared to smaller plates. The interference between scattered and transmitted light gives rise to interference fringes, with a pattern that depends on the focal plane. When using the radial polariser, the light illumination has a high numerical aperture, which leads to a point-spread function shape especially sensitive to the focal plane. This in turn might cause artefacts in the measured areal integral, giving the value of σ_R, depending on the fringing pattern, if the sample is not at the optimum focal plane. Fig. 5.10 (b), shows examples of these fringes . To mitigate these outcomes, the integration area around the particles (Ri parameter) was expanded in order to average the effect of fringing. This improved the results for wavelengths of 600 nm, 650 nm, 700 nm, and 750 nm. However, the findings for wavelengths of 500 nm and 550 nm remained unfavourable. The AFM analysis demonstrated an indication of good correlation between observed patterns in the acquired images. However, recognizing a consistent nanoparticle arrangement was challenging, potentially due to particle displacement caused by the addition of silicon oil, as particle adhesion to the glass surface was achieved via wet-casting rather than covalent bonding. Future studies should aim to enhance particle fixation methods to minimize displacement and achieve better reproducibility in pattern correlation. Techniques such as chemical surface modification to promote stronger bonding or the use of adhesives less prone to particle movement could be explored to improve experimental outcomes.

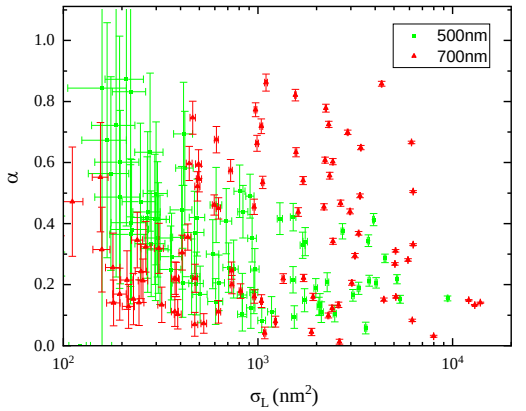

(A)

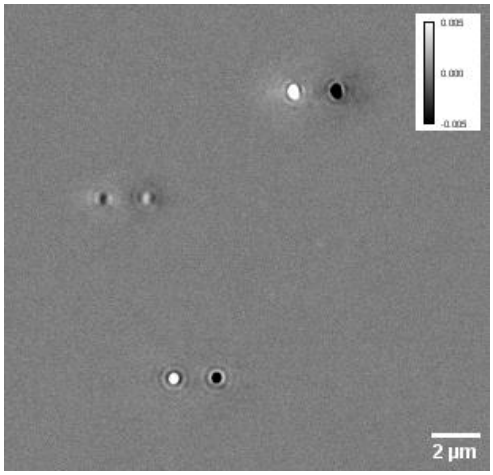

(B)

Figure 5.10: Summary of extinction cross-section values for 98 individual 70nm PVP-AgNPLs. (A) The values obtained with the linear polariser are represented by the fit parameters σ_L and α. The comparison between α and σ_L for 157 individual 70nm PVP-AgNPLs. Green symbols correspond to a wavelength of 500 nm, whereas red symbols correspond to a wavelength of 700 nm. Error bars represent the level of uncertainty resulting from shot noise in the measurements. (B) Extinction contrast image at 650 nm wavelength exemplifying the occurrence of fringes when using the radial polariser.

An example of measurements using the linear and radial polariser at different wavelengths on selected PVP-AgNPLs is shown in Fig. 5.11. The left column shows the dependence at four specific polarisation angles, offering insights about the shape of the nanoparticles. The right column displays the average σ_L cross-section, the fit parameter α and the radial cross-section σ_R. The particle in Fig. 5.11 (A)(B) shows the main peak absorption at around 580 nm, and a strong dependence on the linear polarisation angle ($\alpha > 0.5$ at the peak). The cross sections σ_R and σ_L have similar magnitudes. Hence this particle is not a thin plate, but likely a nanorod, with a small aspect ratio thus a longitudinal LSPR not too shifted in the red. Fig. 5.11(C)(D) shows a main peak absorption below 500 nm, a small dependence on the linear polariser angle (small α) and comparable values between σ_R and σ_L. Hence this particle is likely a spheroid. Fig. 5.11 (E) and (F) shows a particle characterised by two main plasmon modes that are orthogonally polarised relative to each other, one centred around 550 nm and the second around/above 750 nm. The particle exhibits a strong dependence on the linear polariser angle with $\alpha > 0.5$ at 750nm. The cross-section σ_R is smaller than σ_L at 750nm, suggesting that this is a thin plate,

however strongly elongated in-plane to support two LSPR modes. The particle in (G) and (H) shows a main LSPR at 650 nm, and an absorption tail increasing below 500nm. It has a strong polarisation dependence with $\alpha > 0.5$ at 650nm, and σ_R is slightly smaller than σ_L at this wavelength. These properties suggest that the particle is a plate, similar to (E) (F) but possibly thicker, hence with a blue shifted main LSPR and a larger σ_R. The particle in (I) and (J) shows two absorption tails indicating a resonance below 500nm and above 750nm. The value of α is large and the cross sections σ_R is significantly smaller than σ_L at 750nm. This particle is thus similar to (G)(H), and (E)(F) albeit having a more red-shifted longitudinal LSPR, hence is likely a thin plate which is even more elongated in-plane.

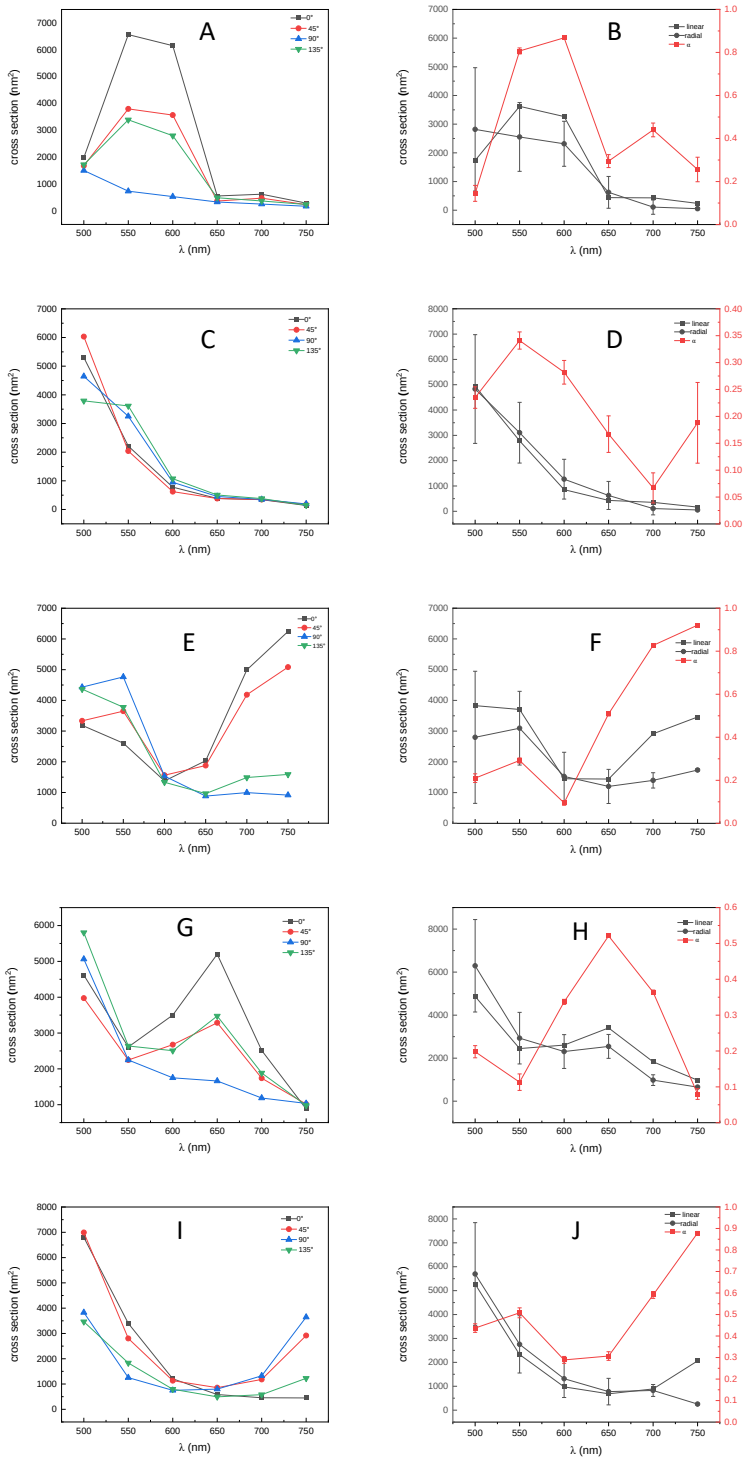

Figure 5.11: Optical extinction cross-sections measured on five selected individual 70nm PVP-AgNPLs: The left column shows σ_{ext} measured at (0, 45, 90, and 135)°linear polarisation angle for five selected PVP-AgNPLs of 70nm size and 10 nm thickness with six different wavelengths. The right column shows the relative amplitudes (α), the average linear σ_{ext} and the radial σ_{R} for the same PVP-AgNPLs in the left column.

Chapter 6

Correlative optical extinction and time-resolved pump-probe spectroscopy

The majority of the work in this thesis has focused on the linear optical properties of silver nanoplates. On the other hand, gold and silver nanoparticles exhibit significant nonlinear optical properties, that can be exploited for applications in bioimaging and biosensing. To that end, the Borri group has demonstrated transient resonant four-wave mixing (FWM) micro-spectroscopy on single gold nanoparticles, as a powerful method to detect these particles background-free inside cells and tissues [151][152][8][153]. In these experiments, FWM can be understood as a pump-probe approach where the absorption of a short pump pulse at the LSPR forms "hot" electrons, which cause a transient change in the dielectric function of the metal particle. This change affects the light scattering properties of the nanoparticle, due to a transient broadening and shift of the LSPR caused by the hot electrons. The change is then probed by a short pulse that follows the pump. Notably, beyond imaging, the temporal dynamics of these pump-induced changes in the LSPR characteristics can be studied by varying the time delay between pump and probe pulses [154]. In turn, these measurements provide insights into the thermal and mechanical coupling of the nanoparticle with its surrounding environment [154]. Hence, in collaboration with another PhD student in the Borri's lab, Martina Recchia, the application of transient FWM spectroscopy was explored on the PVP-coated silver nanoplates previously described in this thesis. Measurements were conducted on 20 individual PVP-AgNPLs with a nominal 70 nm size (see 2.1.1). This chapter presents exemplary data that illustrates the observed dynamics. The main outcome of this study was the observation of a nanoparticle shape change occurring during the measurements, likely due to movements of the Ag particles and particle reshaping induced by the pulsed laser excitation. Transient resonant FWM measurements were correlated with optical extinction microscopy on the same individual particles, before and after pulsed laser excitation. Overall, the results showcase the sensitivity of FWM technique to capture transient nanoscale shape changes as they occur in a single nanoparticle under pulsed laser excitation. For this work, it should be acknowledged that my contribution consisted in acquiring and analysing all the optical extinction cross-section data, before and after FWM, while transient FWM was acquired by Dr Iestyn Pope and analysed by Martina Recchia. Although not acquired by me, for the sake of completeness, a selection of FWM data are shown in this Chapter.

6.1 Sample preparation

Glass slides and coverslips (Menzel-Gläser) were cleaned by sequential sonication phases method as described in section 2.3.1. PVP-AgNPLs with nominal 70 nm size were deposited onto the coverslip via a wet casting method as explained before in section 2.3.2.

6.2 FWM set-up

Individual PVP-AgNPLs were investigated correlatively using wide-field extinction micro spectroscopy and transient resonant FWM. For both optical extinction and FWM microscopy, a Nikon Ti-U inverted microscope was used (see also section 2.4.1) which was setup with a 1.34 NA oil-immersion condenser (Nikon MEL41410) and a 1.45 NA 100X oil immersion objective (Nikon MRD00405) coupled with 1X tube-lens. Fig. 6.1 illustrates the additional component employed in FWM-spectroscopy.

FWM is a phenomenon of third-order nonlinear light-matter interaction. It occurs when three light fields interact within a medium, resulting in the generation of a fourth wave. In this technique, a configuration was employed where all waves shared a common centre frequency of 550nm. Additionally, two of the incident light fields are indistinguishable, resulting in a two-beam degenerate FWM process. The technique utilizes a combination of short optical pulses of 150 fs pulse duration, referred to as pump, probe, and reference, all produced by the same laser source. The observed FWM phenomenon can be explained as a modification of the dielectric function of the metal NPs caused by the pump beam. This modification results in a variation in the scattering of the probe beam after the pump pulse. The delay time between pump and probe pulses is adjusted using a delay line in the pump beam path. The sample is targeted with pump and probe pulses using a high numerical aperture microscope objective, and the FWM signal is gathered by the same objective in reflection (epi-geometry). In order to differentiate the FWM from the pump and probe beams, a heterodyne detection scheme is implemented. This involves modulating the amplitude of the pump beam at a frequency of $\nu_m = 400$ kHz, shifting the probe beam by a radiofrequency of $\nu_2 = 82$ MHz, and detecting the interference between the FWM and reference fields at the corresponding radiofrequency sidebands $\nu_2 \pm \nu_m - \nu_L$ (taking into account the laser repetition rate of $\nu_L = 80$ MHz). The interference is detected by utilizing balanced Si photodiodes (Hamamatsu S5973-02) and a multichannel lock-in amplifier (Zurich Instruments HF2LI). This setup allows for the simultaneous detection of the carrier signal (i.e., the reflected probe) at a frequency of $\nu_2 - \nu_L = 2$ MHz, as well as the sidebands at frequencies $\nu_2 \pm \nu_m - \nu_L = 2 \pm 0.4$ MHz. In order to capture images, the sample is manipulated by scanning a xyz sample stage with nanometric precision (MadCityLabs NanoLP200), which positions and moves the sample in relation to the focal volume of the objective. The FWM technique we employ incorporates a dual polarization detection scheme that offers valuable insights into the geometric properties of the particle being analysed. In this approach, the probe and pump beams, which are initially horizontally (H) and vertically (V) polarised in the laboratory system, , respectively, are converted into cross-circularly polarised beams at the sample using a combination of $\lambda/4$ and $\lambda/2$ waveplates. The reflected probe and FWM fields, which are collected by the microscope objective, propagate through the same waveplates. As a result of this geometry, a probe light field that is reflected by a flat sample surface returns with vertical (V) polarisation in the laboratory system. Reflected probe and FWM fields are combined and interfere with the reference beam outside the sample, via a beam splitter (BS_2 in Fig. 6.1). The reference beam is polarised at 45 degrees prior to recombining with the epi-detected signal. After the beam splitter, a Wollaston prism (not shown in Fig. 6.1) vertically separates H and V polarisations for each arm of the interferometer. Two pairs of balanced Si photodiodes provide

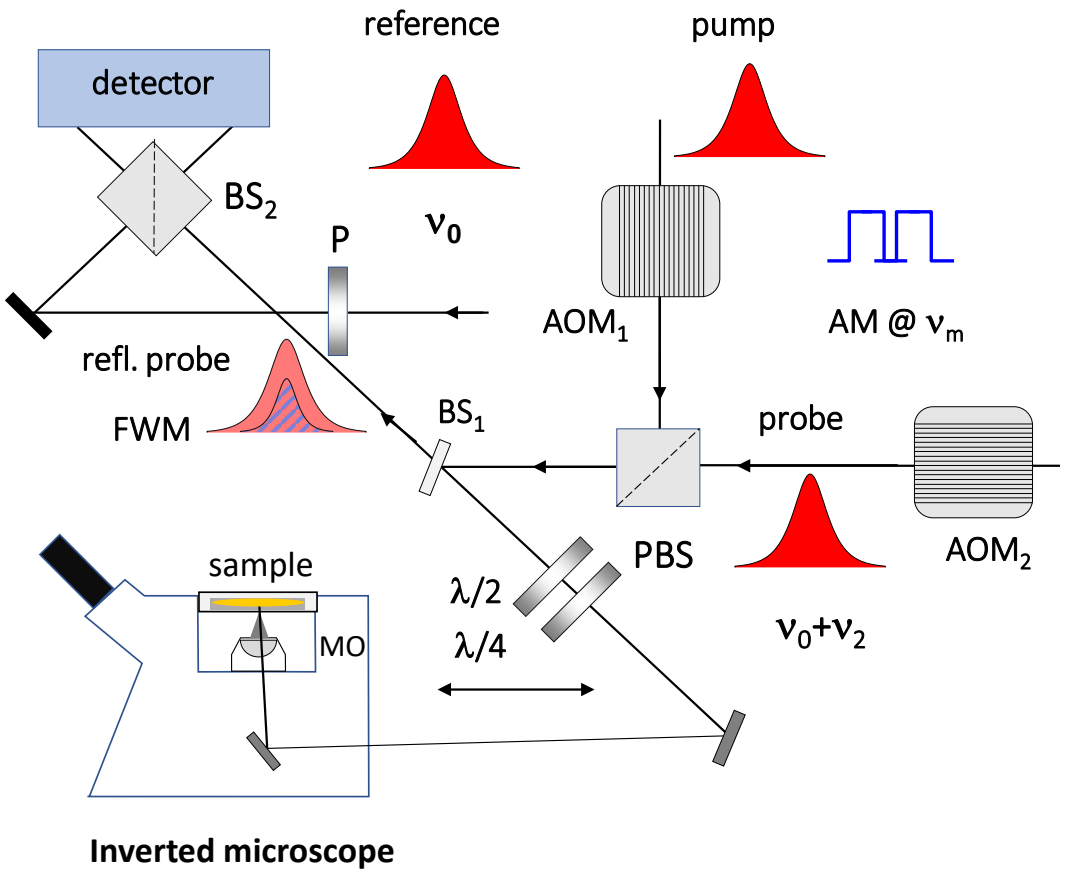

Figure 6.1: Diagram illustrating the configuration of the four-wave mixing (FWM) set up. The sample is exposed to short optical pulses (150fs duration) centred at 550nm wavelength, in resonance with the LSPR of PVP-AgNPLs. These pulses are focused onto the sample using an inverted microscope. The FWM field generated at the sample is collected in epi-geometry and detected using a heterodyne interferometric scheme. An AOM, or acousto-optic modulator, is a device used to control the intensity, frequency, or phase of a laser beam by modulating it with an acoustic wave. In this set-up, AOMs are used to shift the probe optical frequency by the radio-frequency amount ν_2 and to amplitude modulate the pump by ν_m. (P)BS stands for beam splitter (polarising). P: polariser. MO: Microscope Objective. $\lambda/2$ and $\lambda/4$ are waveplates used to control the light polarisation at the sample. Figure adapted from [151].

polarisation-resolved detection. The bottom (top) pair measures the difference in current (to block common-mode noise) between the V (H) polarised interferometer arms. The measured interference corresponds to the co- and cross-circularly polarised components of the reflected probe and FWM fields relative to the incident circularly polarised probe, having amplitudes (phases) indicated as $A_{r\pm}$ and $A_{\mathrm{FWM}\pm}$ ($\Phi_{r\pm}$ and $\Phi_{\mathrm{FWM}\pm}$) respectively, where $+(-)$ refers to the co(cross) polarised component. As demonstrated in [153], the spatial pattern of the cross-polarised reflected probe and FWM fields encode important information on the nanoparticle asymmetry. In particular, if an NP is perfectly round, we expect to observe the pattern of the

cross-polarised light field component in the focal plane, from the combination of a high numerical aperture (NA) objective and the vectorial nature of the light field. This pattern manifests as so-called optical vortex of topological charge $l = 2$, meaning it has an amplitude that is zero at the focus centre, a radially symmetric non-zero amplitude away from the centre, and a phase change with twice the in-plane polar angle. Conversely, a non-spherical particle even with a very small asymmetry (down to 0.5% ellipticity) was shown to generate a significant non-zero value of the cross-polarised field in the focus center. Using a particle ellipsoid model in [153], one can calculate the FWM amplitude ratio $A_{\mathrm{FWM}-}/A_{\mathrm{FWM}+}$ versus the in-plane elliptical aspect ratio of the NP. For the case of a gold NP, this dependence is shown in [151] for large ellipticities and reported in Fig. 6.2 below. It is interesting to observe that the ratio $A_{\mathrm{FWM}-}/A_{\mathrm{FWM}+}$ can be larger than 1.

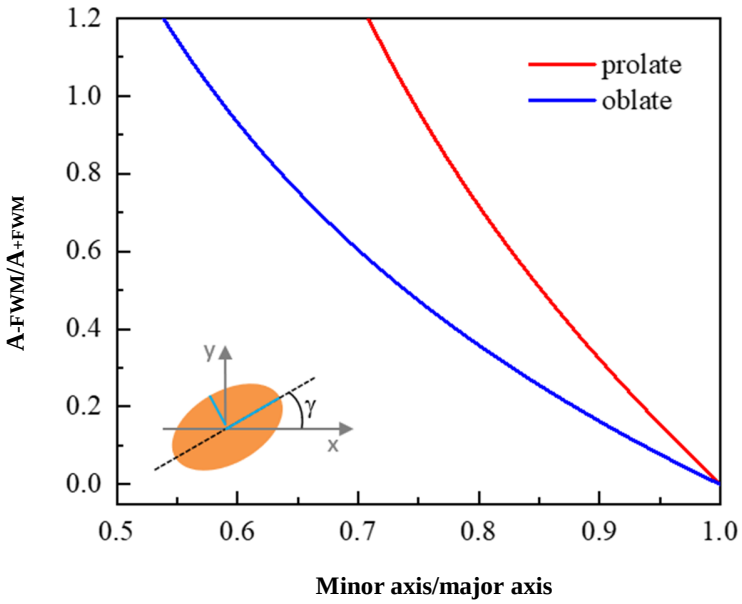

Figure 6.2: Calculated ratio of the cross- to co-circularly polarised FWM amplitude versus the in-plane elliptical aspect ratio, assuming a gold nanoparticle (NP) ellipsoid shape in-plane, as depicted in the sketch. The red (blue) line is calculated assuming a prolate (oblate) ellipsoid with axis $a > b = c$ ($a < b = c$) aligned along the x, y, and z directions, respectively. The calculations are performed using the ellipsoid model discussed in [153] and [151].

An intuitive understanding of this behaviour can be provided as follows. An elongated NP ellipsoid exhibits two orthogonally polarised LSPRs, called longitudinal and transverse modes. The longitudinal mode is red-shifted compared to the transverse mode by an amount that depends on the NP ellipticity. Each plasmon mode will contribute to the reflected probe field and the FWM field with a phase shift that depends on the frequency position of each LSPR relative to the wavelength (or frequency) of the probing light field. The polarisability contribution of each LSPR mode can be described as a complex Lorentz oscillator function, with a phase lag ranging from 0 to π going from frequencies below to above the LSPR resonance. Therefore, if the frequency of the incident light is well above or below both LSPR frequencies, each LSPR will contribute with the same phase lag, i.e., there is no phase difference introduced by the two LSPRs and hence no significant modification of the probe field polarisation introduced by the interaction with the particle. Conversely, if the frequency of the incident light is close to that of the LSPRs, such that each mode contributes with a different phase lag, there will be a significant change in the polarisation of the reflected probe field. Since the phase difference can reach up to π, this can lead to a complete reversal of the circular polarisation handedness of the reflected probe, explaining how a cross-polarised contribution can indeed be larger than the co-polarised component.

6.3 Correlative optical extinction and FWM microscopy

Fig. 6.3 shows the extinction spectrum measured on three different individual AgNPLs, which exhibit different polarisation dependences and thus must have different shapes. For comparison, Fig. 6.4 shows simulations performed in house using the numerical modelling soft-ware COMSO Multiphysics (simulations performed by Prof. Wolfgang Langbein), assuming different geometries of silver nanoplates, consistent with the hypothetical shapes discussed for Fig. 6.3, which support the proposed attributions. In the first case (Fig. 6.3 a), the extinction cross-section is almost independent of the polarisation direction. A spherical silver NP has an LSPR in the blue (around 450 nm when surrounded by a medium with n=1.52 index). Since the observed extinction cross-section has a band around 650 nm and an LSPR peak >750 nm, this AgNP is likely a triangle with blunt tips, i.e., a hexagon with non-equilateral sides, as expected from the manufacture specification (see also COMSOL simulations of cross-section spectra in Chapter 3).

Instead, the second spectrum (Fig. 6.3b) is clearly associated with an anisotropic particle. It appears to show two main modes, one peaked at 700 nm, which exhibits its maximum cross-section for 45° and 90° polarization directions, and the other further red-shifted, which is maximum for polarizations at 0° and 135° directions. The NP shape could therefore be an elongated, almost rod-shaped, hexagon.

The third spectrum (Fig. 6.3c) is again associated with an anisotropic particle. In this case, two main modes appear within the spectral range probed in the experiment. The polarization-dependent behaviour and spectral position of the two modes suggest that the particle is characterized by two main axes orthogonal to each other and is generally of smaller size than the particles in Fig. 6.3a, b.

Figure 6.5 shows the single xy-plane FWM amplitude images (acquired at the NPs focus in z) for the same AgNP (a), (b), and (c) introduced in Fig. 6.3. The figure shows, from left to right, the spatial pattern of the cross- the circularly polarised reflection amplitude A_{r-}, the cross-circularly polarised FWM amplitude A_{FWM-}, the co-circularly polarised reflection amplitude A_{r+}, and the co-circularly polarised FWM amplitude A_{FWM+}. Albeit nearly index matched, the reflection from the silicon oil-glass interface is visible as a background in the co-circularly polarised reflection image. The following comments about the three cases can be made:

(a) The cross-polarised FWM amplitude is undetectable, and the cross-polarised reflection

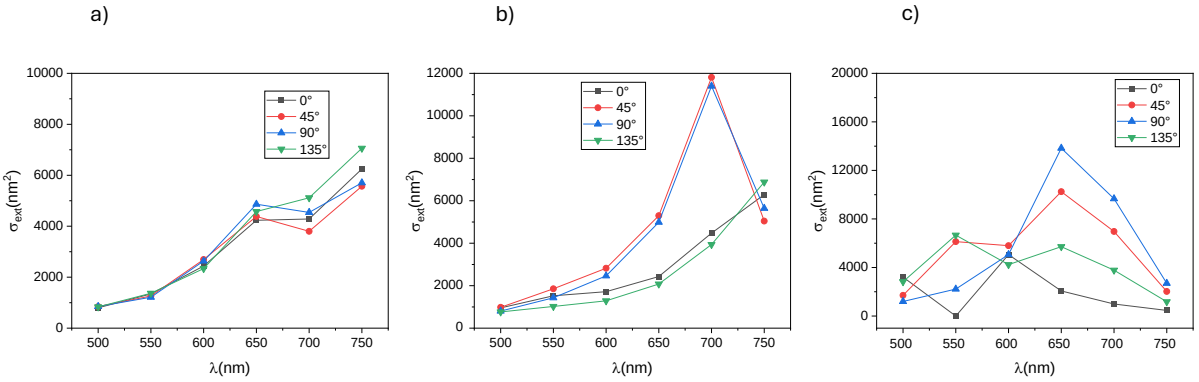

Figure 6.3: Polarisation resolved extinction cross-section spectra extracted from wide-field extinction microscopy measurements on three individual silver nanoplates with different sizes and shapes. The measurements were performed using a white-light halogen lamp with sequentially applied color bandpass filters at the reported center wavelengths. Different in-plane linear polarisation directions of the illumination (0°, 45°, 90°, 135°) were used. See also Chapters 2 for more details of the measurement set-up and acquisition parameters.

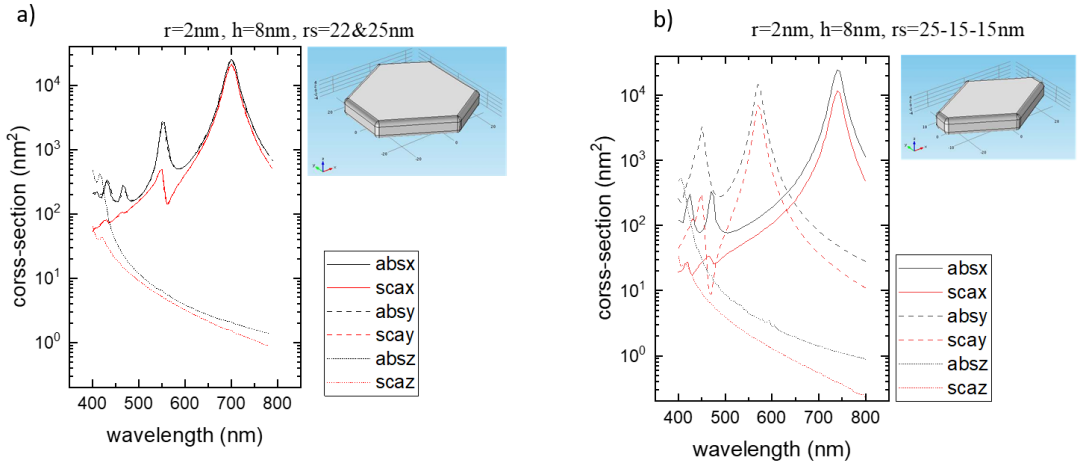

Figure 6.4: COMSOL simulation of extinction (absorption and scattering) cross-section spectra for individual silver nanoplates with different size and shape, as schematically shown in the pictures. a) Non-equilateral hexagon retaining 3-fold rotation symmetry; b) elongated hexagon. In the simulations, h is the plate height, r is the radius of curvature of the edges, and rs are the distances of the edges to the centre. The illumination polarisation direction is given as x, y (in plane, with z-propagation direction) and z (vertical, with x propagation direction). Simulations assume n=1.52 as surrounding medium refractive index.

component is much smaller ($\sim$ 15-fold) than the co-polarised component. This is consistent with the measured extinction spectrum attributed to a AgNP largely symmetric, not elongated, and with LSPRs wavelengths all above the 550 nm wavelength of the probe

fields.

(b) In this case, a non-zero value is found for A_{FWM-}, but the co-polarised component is significantly larger, and a similar behaviour is found for the reflection, i.e. $A_{FWM,r+} > A_{FWM,r-}$. This is consistent with the measured extinction suggesting an elongated particle with two LSPRs. One LSPR peak is observed at around 700 nm and the other is at a longer wavelength $>$ 750 nm. Hence, relative to the 550 nm wavelength of the probe field, these two LSPRs are introducing only a slightly different phase lag and thus a small cross-polarised component.

(c) In this case, it is found that $A_{FWM,r-} > A_{FWM,r+}$. This is again consistent with the measured extinction spectrum suggesting an elongated particle with two LSPR modes at around 550 nm and 650 nm respectively, hence contributing with a significantly different phase lag relative to the incident probe wavelength, and thus resulting in a larger cross-polarised component.

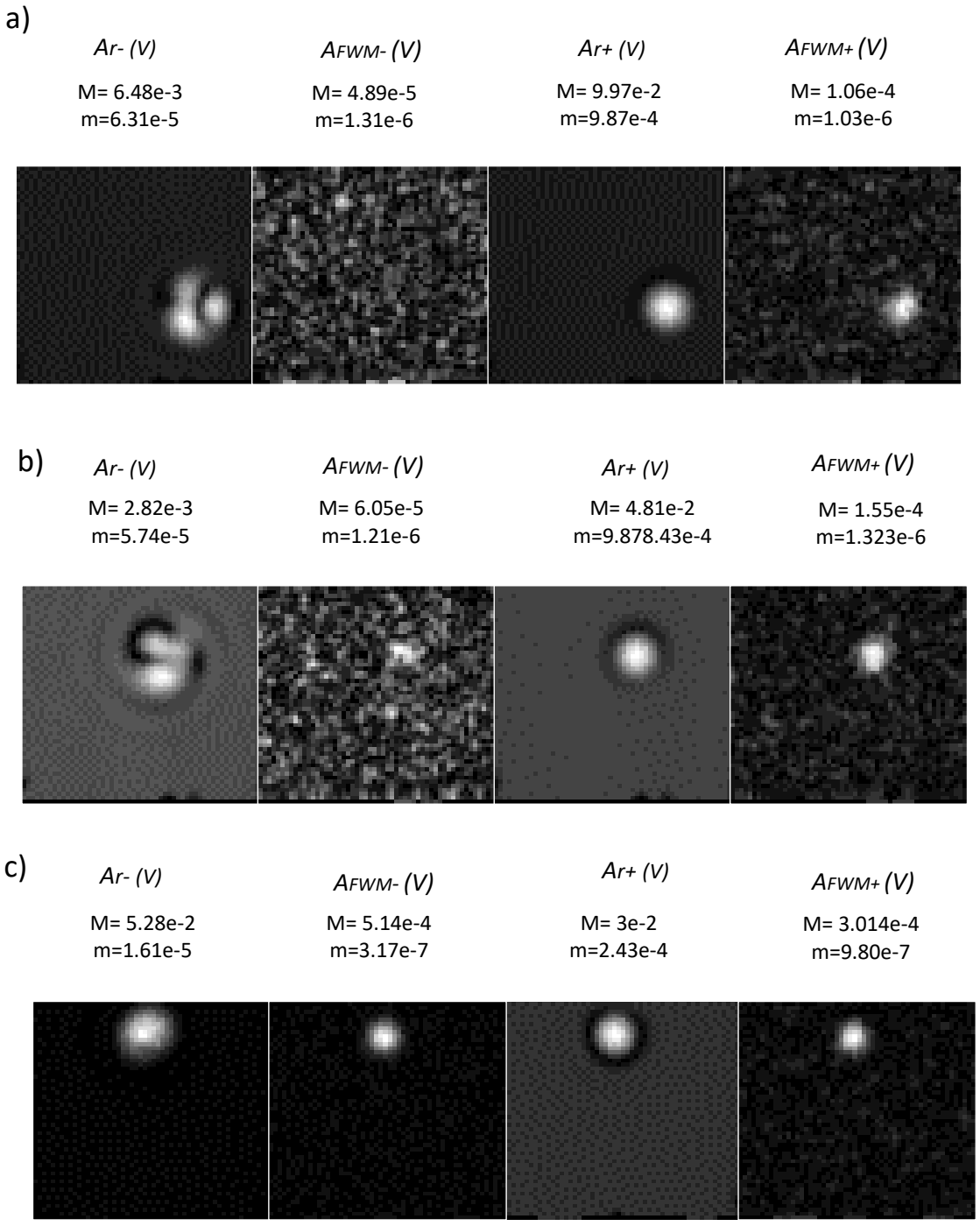

Figure 6.5: Single xy-plane images (2 μm $\times$ 2 μm, 54 $\times$ 54 steps) for the nominal 70 nm PVP-AgNPLs presented in Fig. 6.3 (a), (b) and (c). From left to right: cross-circularly polarized reflection amplitude A_{r-}, cross-circularly polarized FWM amplitude A_{FWM-}, co-circularly polarized reflection amplitude A_{r+}, and co-circularly polarized FWM amplitude A_{FWM+}. Powers measured at the entrance of the microscope are (a) $P_{\text{pump}} = 20$ μW, $P_{\text{probe}} = 10$ μW, (b) $P_{\text{pump}} = 30$ μW, $P_{\text{probe}} = 15$ μW, (c) $P_{\text{pump}} = 10$ μW, $P_{\text{probe}} = 5$ μW. FWM acquired with a pump-probe delay time of 0.5ps. Amplitudes are on a grey linear scale from m (black) to M (white), as indicated. Values are in units of Volts.

6.3.1 Time-resolved FWM dynamics

As briefly introduced previously, the detected FWM in our experiment can be understood as a pump-induced change in the metal NP dielectric function, which manifests as a change in the light scattering of the probe beam following the pump pulse with an adjustable delay time. In Ref [155] this technique has been applied to nominally spherical gold nanoparticles exhibiting a localized surface plasmon resonance in resonance with the wavelength of the pump and probe beams. By changing the delay time between pump and probe pulses, this study provided important information on the characteristic time scales associated with:i) the formation of a hot electron gas in the metal following the pump absorption ($\sim$ 100 fs),ii) the cooling of the hot electrons with the lattice ($\sim$ 10 ps), and iii) the cooling of the lattice with the environment ($\sim$ 100 ps) depending on the local thermal conductivity. It also showed that the impulsive excitation of the NP excited mechanical breathing modes, which appeared as coherent oscillations in the pump-probe delay time dependence, due to the change of the NP volume and, in turn, the plasma frequency. In this section, the results obtained by applying such a time-resolved FWM technique on the PVP-AgNPLs introduced in the previous sections are shown. In the experiment, the pump-probe delay range and temporal resolution can be chosen. Here, the analysis is shown for data acquired on a 505 ps delay range (from -5 ps to 500 ps) with a temporal resolution of 0.5 ps. Notably, for each particle, multiple sequential repeats of the pump-probe delay scan were performed to monitor the stability and reproducibility of the measured dynamics. As previously explained, in our set-up, both co- and cross-circular polarised components of the reflected probe field E_r and FWM field E_{FWM} are detected. To correct the FWM signals for possible mechanical drifts and laser fluctuations, the complex $E^{\mp}_{FWM}$ was normalized to the corresponding complex E^{+}_{r} as:

$$E^{N}_{FWM,\mp} = \frac{ReE_{FWM,\mp} + iImE_{FWM,\mp}}{ReE_{r,+} + iImE_{r,+}} \tag{6.1}$$

The delay dependence of the amplitude, as well as the real and imaginary components of the detected normalized complex field $E^{N}_{FWM,\mp}$, can then be examined. The experiments were carried out using the following sequential procedures:

- Spectra of extinction were obtained before any laser exposure.
- Images of FWM and reflected probe in the xy-plane were obtained with a delay of 0.5 ps.
- FWM signals in the centre of the NP were measured as a function of the delay between the pump and probe pulses, with 4 repetitions.
- Images of FWM and reflected probe in the xy-plane were obtained again with a delay of 0.5 ps.
- Spectra of extinction were acquired after all laser exposures.

Fig. 6.6 shows a comparison of the extinction cross section for a particle under study, before and after the laser exposure (left panels). It also shows the xy-plane FWM images before and after the FWM pump-probe delay dependence (right panels), obtained using 10 µW time-average power for the pump beam and 5µW for the probe (as measured on the beam prior to entering the microscope).

Before the laser exposure, this PVP-AgNP is characterized by two main plasmon modes orthogonally polarised relative to each other, one centered around 600nm and the second around 700nm. Considering the position of these two modes relative to the probe wavelength of 550nm, as discussed in the previous section, a significant AFWM$_-$ component, similar to AFWM$_+$, is expected to be detected. This is indeed observed in the corresponding FWM image. During the time-resolved FWM experiments, a change in the particle response (see Fig. 6.7) is observed, which is attributed to a pump-induced reshaping. Indeed, after these experiments the extinction spectrum is substantially different, representing a more isotropic NP shape with LSPR resonances closer to 550 nm.The ratio of the cross- to co-polarised component is thus expected to be smaller due to the relative phase difference from these shifted resonances, and it is found that this ratio has decreased, both in FWM and in the reflected probe.

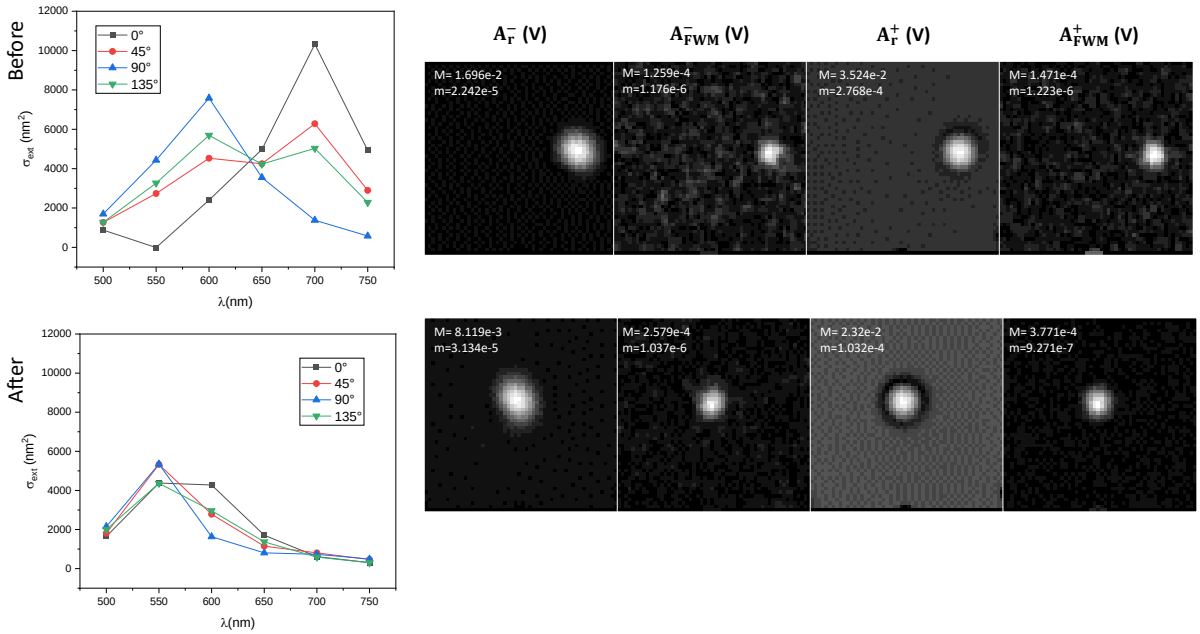

Figure 6.6: **Top:** Data acquired before the FWM pump-probe delay scan measurement. **Bottom:** Data acquired after the FWM pump-probe delay scan measurement. **Left:** Polarisation resolved extinction cross-section spectrum obtained from wide field extinction microscopy measurements. **Right:** Single xy-plane images (2µm x 2µm, 54 x 54 steps) of the NP showing (from left to right) the cross-circularly polarized reflection amplitude $\mathbf{A_{r-}}$, the cross-circularly polarised FWM amplitude $\mathbf{A_{FWM-}}$, the co-circularly polarized reflection amplitude $\mathbf{A_{r+}}$, and the co-circularly polarised FWM amplitude $\mathbf{A_{FWM+}}$. Powers measured on the beam prior to entering the microscope: $P_{\text{pump}} = 10\mu W$, $P_{\text{probe}} = 5\mu W$. FWM acquired with a pump-probe delay time of 0.5 ps. Gray scales from m (black) to M (white), in volts, as indicated.

.

The results for the time-resolved FWM experiment on the AgNP are shown in Fig. 6.7. The FWM amplitude (top), as well as the real (middle) and imaginary part (bottom), are plotted for the normalized FWM field $E_{\text{FWM,N}}$ for both co- (left) and cross- (right) polarized components. Data are shown for each performed scan repetition (indicated as "1st rep", "2nd rep", etc.). The subscript "N" is dropped in the figure labels for simplicity. There is a clear change in the observed dynamics between different repetitions. The main features are: i) an ultrafast initial rise in the amplitude and real part components at pump-probe time overlap, ii) damped oscillations on

top of an amplitude decay dynamics visible in the first 100 ps range, and an improved signal to noise ratio after the first repetition, and iii) some long-lived dynamics such as a constant FWM amplitude still visible after 500 ps. In line with the observed change in the extinction spectrum, these data suggest that the particle is reshaping during the experiment, gaining a plasmon resonance closer to the pump and probe wavelengths after the first repetition, and in turn more resonantly absorbing the pump pulse and scattering the probe, with a resulting increased signal-to-noise ratio. The oscillation behaviour is expected to relate to mechanical modes which have been impulsively excited, and in turn correlate with the AgNP shape and size. In analogy with our previous study with gold NPs in Ref [155], we expect the oscillation damping to be linked to the mechanical coupling with the environment, while the overall signal decay in the 100 ps range is due to the NP thermalisation with its surroundings, which depends on the local thermal conductivity. The long-lived dynamics is most likely a manifestation of photo-thermal effects, namely a change in the refractive index surrounding the NP, and in turn of the light scattering experienced by the probe field, due to the temperature increase of the medium in the focal volume once the NP has thematised with its surroundings, which typically has a slow (0.1–1 μs) relaxation time.

6.3.2 More optical extinction results

This section provides an overview of various PVP-AgNPLs, each of which underwent a similar measurement process as previously discussed. It illustrates the appearance of the extinction cross section before and after laser application, highlighting various instances of reshaping, consistent with the experiment described in the previous section. Fig. 6.8 shows four different PVP-AgNPLs that exhibit different behaviours before and after applying the laser in the FWM experiment. The left column in Fig. 6.8, which contains graphs (A, C, E, and D), displays different peaks at specific wavelengths before laser irradiation, while the right column (graphs (B, D, F, and H)) shows the change in spectra after applying the laser. Starting with the first particle in the graphs (A, B), the data demonstrate a change in shape, transitioning from a symmetric particles with LSPR in the blue (hence likely a silver spheroid) to an asymmetric particle exhibiting and LSPR at around 560 nm for a given polarisation configuration (suggesting the formation on an elongated ellipsoid). Conversely, both the PVP-AgNPLs in (C, D) and (E, F) do not significantly change their optical cross-section after using the laser. These particles have a LSPR at or below 500 nm. Particle (C, D) has a small cross-section and a weak polarisation dependence. Its broad spectrum suggests that it could be a silver tarnish Ag_2S particle, as discussed in Chapter 3. Particle (E) shows a significant cross-section magnitude and a LSPR spectrum with a polarisation dependence similar to B, suggesting an ellipsoid. Upon laser excitation, the particle does no longer show an LSPR band around 550 nm, but a blue-shifted resonance, suggesting that it is rounding up into a spheroid upon laser excitation. Particle (G) is a silver plate with a red LSPR. Upon laser excitation the LSPR is blue-shifted and the cross-section magnitude increases, suggesting that the plates becomes thicker. Overall, the variety of observed shape changes upon pulsed laser excitation are intriguing. Notably, it is well known (as also reported by the manufacturer nanoComposix) that silver nanoplates are relatively unstable. Small particles are particularly sensitive to reshaping effects because of their high surface to volume ratio. While capping with a PVP polymer is meant to protect these particles, the exposure to ultrafast pulsed laser light has a significant perturbing effect. A detailed explanation of this behaviour is, however, beyond the scope of this thesis. In summary, in this chapter we investigated the thermal and mechanical coupling of individual 70 nm PVP-AgNPLs with their environment using FWM, a pump-probe spectroscopy technique. The results showed changes in the nanoparticles during measurements, likely due to particle reshaping caused by the pulsed laser excitation in the FWM experiments. These changes were confirmed through correlative

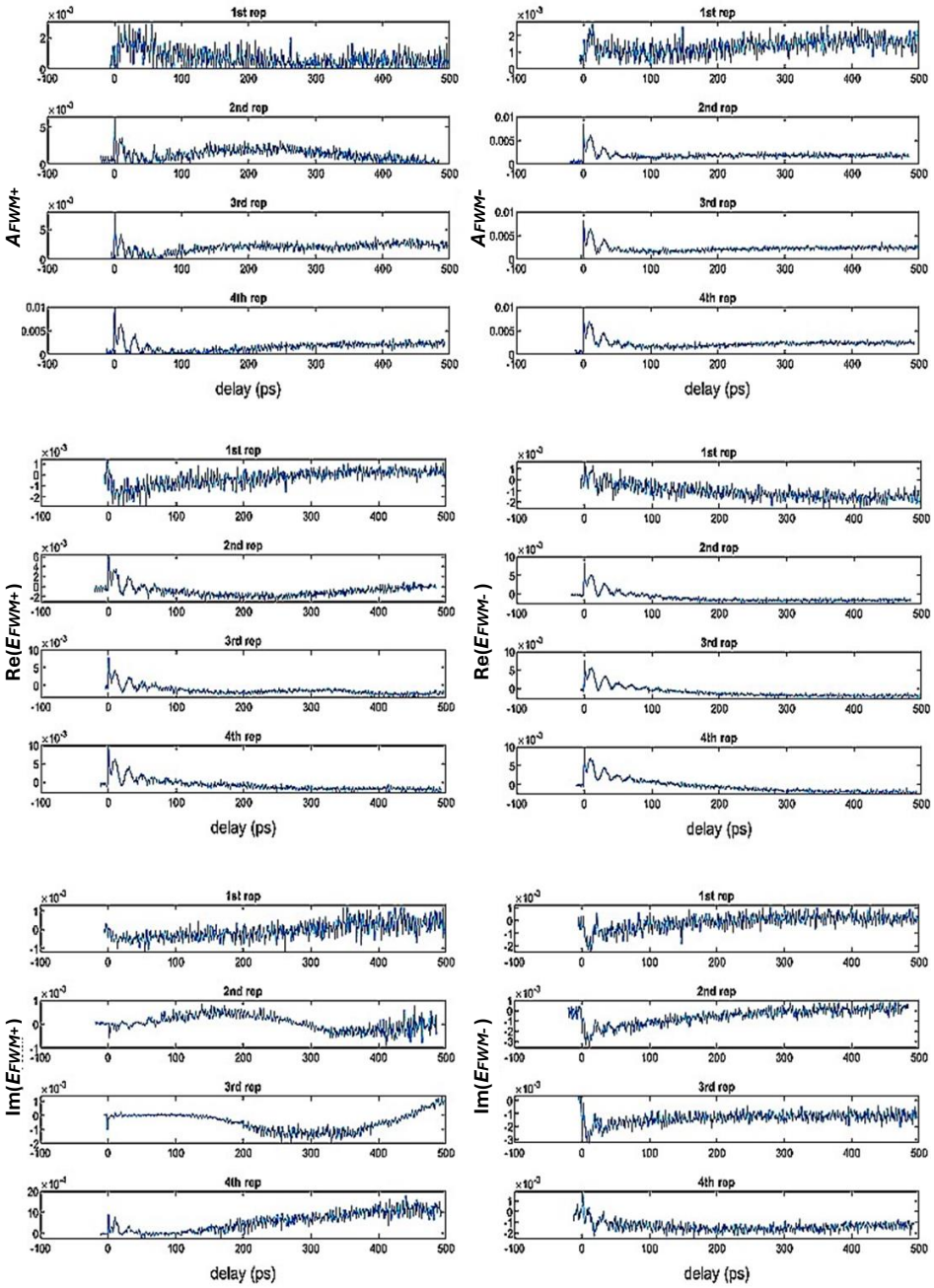

Figure 6.7: Co- ($E_{\mathbf{FWM+}}$) and cross-circularly ($E_{\mathbf{FWM-}}$) polarised FWM field (normalized to the co-polarised reflected field) versus pump-probe delay time. Top: amplitude $A_{\mathrm{FWM-}}$ (right), $A_{\mathrm{FWM+}}$ (left). **Middle:** real part $\mathrm{Re}\{E_{\mathrm{FWM-}}\}$ (right), $\mathrm{Re}\{E_{\mathrm{FWM+}}\}$ (left). **Bottom:** imaginary part $\mathrm{Im}\{E_{\mathrm{FWM-}}\}$ (right), $\mathrm{Im}\{E_{\mathrm{FWM+}}\}$ (left). The delay was scanned over 505 ps, with a resolution of 0.5 ps. Powers used, as measured on the beam prior to entering the microscope: $P_{\mathrm{pump}} = 5\mu\mathrm{W}$, $P_{\mathrm{probe}} = 2.5\mu\mathrm{W}$.

extinction microscopy performed before and after FWM exposure. While the findings provided new insights into the reshaping behaviour, further analysis is required to fully understand the electron cooling dynamics and photothermal effects from the time-resolved FWM data. Preliminary FWM measurements at different time ranges and resolutions have been completed, which will aid in distinguishing various contributions. A comprehensive analysis of the full dataset

from 20 individual nanoparticles is expected to offer a deeper understanding of the transient reshaping behaviour at the nanoscale.

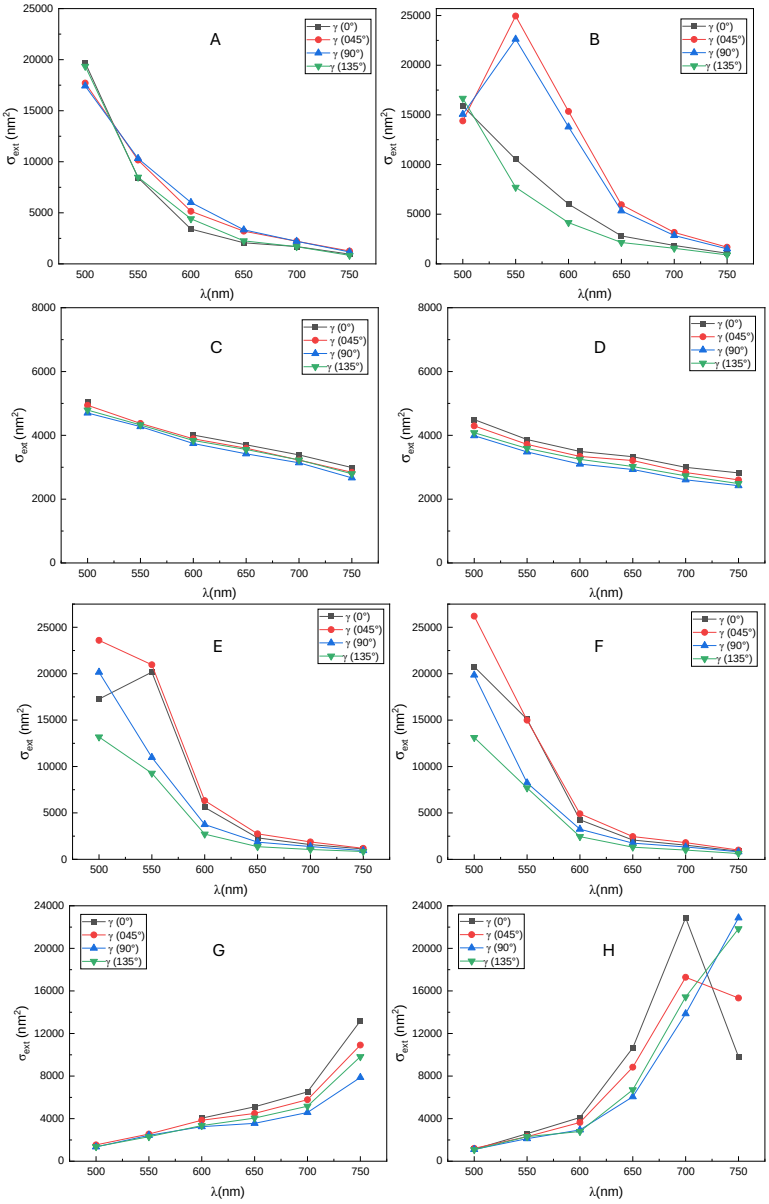

Figure 6.8: Optical extinction cross-sections measured on four different individual nominal 70nm PVP-AgNPLs: The left column represents linear σ_{ext} at (0, 45, 90, and 135)°polarisation angle for four different PVP-AgNPLs with six different wavelengths before using laser. Right column represents linear σ_{ext} for the same PVP-AgNPLs in left column after using the laser exposure for FWM microscopy.

Chapter 7

Conclusion

To conclude, this work further demonstrates the applicability of optical extinction microscopy for individual nanoparticle size and shape analysis, in a quantitative and high-throughput way, for nanoparticles (NPs) of non-trivial shapes. The integration of a radial polarizer in the optical path, as developed in Chapter 3, presents a significant advancement, increasing sensitivity to the z-component of the polarization. This improvement enables more robust characterization of complex nanoparticle morphologies, such as thin nanoplates like those studied in this thesis. The cluster analysis developed and applied to PVP-AgNPLs and SiO_2-AgNPLs was also a novel contribution, providing a method to categorize heterogeneous nanoparticle populations effectively, using predictors derived from their quantitative extinction cross-sectional properties. The investigation of SiO_2-AgNPLs in Chapters 3 and 4 demonstrated the importance of averaging over particle orientations. This was especially important for these particles because the silica shell coating prevented SiO_2-AgNPLs from lying flat onto the glass substrate surface. For these particles, the cluster analysis was modified by introducing new predictors, in order to remove the variability from orientation differences. Complementary to applying a"post-acquisition" rotational averaging, as shown in Chapter 3, a physical rotational averaging was introduced in Chapter 4 by utilizing a medium of controlled viscosity in which nanoparticles are free to rotate. This study is a significant advancement in our ability to accurately categorize particle shapes in different environments.

The correlation attempted in Chapter 5 between optical extinction and atomic force microscopy sheds light on the challenges associated with the spatial registration of microscopy measurements acquired with different methods. Specifically, the work provided important insights into the inconsistencies and potential sources of error during sample preparation and measurement, particularly involving the potential movement of nanoparticles.

The investigation of individual PVP-AgNPLs using four-wave mixing (FWM) spectroscopy in Chapter 6 adds a new dimension to our understanding of nanoparticle behavior under laser excitation. The observation of nanoparticle reshaping, likely due to Ag atom mobility induced by pulsed laser exposure, highlights the dynamic nature of silver nanoplates and opens new avenues for understanding their mechanical and thermal properties under external stimuli.

The significance of these findings lies in the advancements made in both nanoparticle characterization techniques and our understanding of nanoparticle material properties. The use of optical extinction microscopy coupled with advanced cluster analysis tools provides a powerful framework for evaluating the morphometric and optical properties of large populations of nanoparticles. Moreover, the integration of FWM as a complementary technique to extinction microscopy demonstrates the capability to study transient properties and structural changes at the single-particle level.

7.1 Outlook and future directions

To fully realize the potential impact of the methods discussed in this thesis, further work is needed to address several limitations. In Chapter 4, the rotational averaging of nanoparticles diffusing in a viscous medium was sub-optimal, leading to a noisier and less conclusive cluster analysis compared to results in Chapter 3, where particles were fixed on a surface. The approach utilised to average over particle orientations was limited by the trad-off between rotation and translation dynamics. Particles needed to remain in focus during the measurement acquisition, while rotating sufficiently to average over their orientation. In practice, the observation times did not ensure full rotational averaging, prior to particle drifting out of focus. Improvements can be made by increasing the measurement duration, controlling the viscosity of the medium, and reducing the sample thickness to prevent nanoparticles from diffusing out of focus. In Chapter 5, while a protocol was developed to identify the same region of interest using both AFM and optical extinction microscopy, the inability to consistently correlate individual nanoparticles between the two techniques highlighted the need for better sample preparation methods. Future work could focus on using patterned surfaces or covalent binding of nanoparticles to ensure they remain fixed during measurements. In Chapter 6, while FWM revealed dynamic shape changes in individual nanoparticles, further in-depth analysis is needed to disentangle the various contributions to these changes, such as electron cooling dynamics and photothermal effects. A more detailed, quantitative analysis of FWM measurements acquired utilizing different time ranges and resolutions, will provide a clearer understanding of nanoparticle reshaping behavior under laser excitation. Future work may include computational modelling of the FWM response of silver nanoparticles, in order to extract quantitative information on the observed transient morphometric changes, potentially driving predictions for future studies.

With these improvements, optical extinction micro-spectroscopy has the potential to become a disruptive technology for nanoparticle morphometric analysis, potentially replacing expensive and time consuming techniques such as electron microscopy.

Bibliography

[1] Alexander L Efros and Louis E Brus. Nanocrystal quantum dots: from discovery to modern development. *ACS nano*, 15(4):6192–6210, 2021.

[2] J Dobson. Gene therapy progress and prospects: magnetic nanoparticle-based gene delivery. 13(4):283–287.

[3] S. Rudge, C. Peterson, C. Vessely, J. Koda, S. Stevens, and L. Catterall. Adsorption and desorption of chemotherapeutic drugs from a magnetically targeted carrier (mtc). *Journal of Controlled Release*, 74(1):335–340, 2001. Proceeding of the International Symposium on Tumor Targeted Delivery Systems.

[4] Manikandan Dhayalan, Priadharsini Karikalan, Mohammed Riyaz Savaas Umar, and Nalini Srinivasan. Biomedical applications of silver nanoparticles. In Samir Kumar, Prabhat Kumar, and Chandra Shakher Pathak, editors, *Silver Micro-Nanoparticles - Properties, Synthesis, Characterization, and Applications*. IntechOpen.

[5] Yaron M Sigal, Ruobo Zhou, and Xiaowei Zhuang. Visualizing and discovering cellular structures with super-resolution microscopy. *Science*, 361(6405):880–887, 2018.

[6] Michael Shribak and Shinya Inoué. Orientation-independent differential interference contrast microscopy. *Applied Optics*, 45(3):460–469, 2006.

[7] Douglas B Murphy and Michael W Davidson. *Fundamentals of light microscopy and electronic imaging*. John Wiley & Sons, 2012.

[8] Naya Giannakopoulou, Joseph B Williams, Paul R Moody, Edward J Sayers, Johannes P Magnusson, Iestyn Pope, Lukas Payne, Cameron Alexander, Arwyn T Jones, Wolfgang Langbein, et al. Four-wave-mixing microscopy reveals non-colocalisation between gold nanoparticles and fluorophore conjugates inside cells. *Nanoscale*, 12(7):4622–4635, 2020.

[9] Lukas M Payne, Wiebke Albrecht, Wolfgang Langbein, and Paola Borri. The optical nanosizer–quantitative size and shape analysis of individual nanoparticles by high-throughput widefield extinction microscopy. *Nanoscale*, 12(30):16215–16228, 2020.

[10] Lukas M Payne, Francesco Masia, Attilio Zilli, Wiebke Albrecht, Paola Borri, and Wolfgang Langbein. Quantitative morphometric analysis of single gold nanoparticles by optical extinction microscopy: Material permittivity and surface damping effects. *The Journal of Chemical Physics*, 154(4), 2021.

[11] Alexander G Shard, Katia Sparnacci, Aneta Sikora, Louise Wright, Dorota Bartczak, Heidi Goenaga-Infante, and Caterina Minelli. Measuring the relative concentration of particle populations using differential centrifugal sedimentation. *Analytical Methods*, 10(22):2647–2657, 2018.

[12] Frank Babick. Dynamic light scattering (dls). In *Characterization of nanoparticles*, pages 137–172. Elsevier, 2020.

[13] Patrick Hole, Katherine Sillence, Claire Hannell, Ciaran Manus Maguire, Matthias Roesslein, Guillaume Suarez, Sonja Capracotta, Zuzana Magdolenova, Limor Horev-Azaria, Agnieszka Dybowska, et al. Interlaboratory comparison of size measurements on nanoparticles using nanoparticle tracking analysis (nta). *Journal of Nanoparticle Research*, 15:1–12, 2013.

[14] Eva Weatherall and Geoff R Willmott. Applications of tunable resistive pulse sensing. *Analyst*, 140(10):3318–3334, 2015.

[15] Joseph I Goldstein, Dale E Newbury, Patrick Echlin, David C Joy, Charles Fiori, Eric Lifshin, Joseph I Goldstein, Dale E Newbury, Patrick Echlin, David C Joy, et al. Image formation in the scanning electron microscope. *Scanning Electron Microscopy and X-Ray Microanalysis: A Text for Biologist, Materials Scientist, and Geologists*, pages 123–204, 1981.

[16] Yi-Hong Hsin, Chun-Feng Chen, Shing Huang, Tung-Sheng Shih, Ping-Shan Lai, and Pin Ju Chueh. The apoptotic effect of nanosilver is mediated by a ros-and jnk-dependent mechanism involving the mitochondrial pathway in nih3t3 cells. *Toxicology letters*, 179(3):130–139, 2008.

[17] Rasmus Foldbjerg, Ping Olesen, Mads Hougaard, Duy Anh Dang, Hans Jürgen Hoffmann, and Herman Autrup. Pvp-coated silver nanoparticles and silver ions induce reactive oxygen species, apoptosis and necrosis in thp-1 monocytes. *Toxicology letters*, 190(2):156–162, 2009.

[18] Gerd Binnig, Calvin F Quate, and Ch Gerber. Atomic force microscope. *Physical review letters*, 56(9):930, 1986.

[19] Craig F Bohren and Donald R Huffman. *Absorption and scattering of light by small particles*. John Wiley & Sons, 2008.

[20] Meindert A van Dijk, Anna L Tchebotareva, Michel Orrit, Markus Lippitz, Stéphane Berciaud, David Lasne, Laurent Cognet, and Brahim Lounis. Absorption and scattering microscopy of single metal nanoparticles. *Physical Chemistry Chemical Physics*, 8(30):3486–3495, 2006.

[21] Aurélien Crut, Paolo Maioli, Natalia Del Fatti, and Fabrice Vallée. Optical absorption and scattering spectroscopies of single nano-objects. *Chemical Society Reviews*, 43(11):3921–3956, 2014.

[22] Tapan K Sau and Andrey L Rogach. Nonspherical noble metal nanoparticles: colloid-chemical synthesis and morphology control. *Advanced Materials*, 22(16):1781–1804, 2010.

[23] Sukdeb Pal, Yu Kyung Tak, and Joon Myong Song. Does the antibacterial activity of silver nanoparticles depend on the shape of the nanoparticle? a study of the gram-negative bacterium escherichia coli. *Applied and environmental microbiology*, 73(6):1712–1720, 2007.

[24] Nikhil R Jana, Latha Gearheart, and Catherine J Murphy. Seeding growth for size control of 5- 40 nm diameter gold nanoparticles. *Langmuir*, 17(22):6782–6786, 2001.

[25] Mahvash Haroon, Almas Zaidi, Bilal Ahmed, Asfa Rizvi, Mohammad Saghir Khan, and Javed Musarrat. Effective inhibition of phytopathogenic microbes by eco-friendly leaf extract mediated silver nanoparticles (agnps). *Indian journal of microbiology*, 59:273–287, 2019.

[26] Virender K Sharma, Ria A Yngard, and Yekaterina Lin. Silver nanoparticles: green synthesis and their antimicrobial activities. *Advances in colloid and interface science*, 145(1-2):83–96, 2009.

[27] Yu A Krutyakov, Alexei Aleksandrovich Kudrinskiy, A Yu Olenin, and Georgii Vasilevich Lisichkin. Synthesis and properties of silver nanoparticles: advances and prospects. *Russian Chemical Reviews*, 77(3):233, 2008.

[28] Julia Fabrega, Samuel N Luoma, Charles R Tyler, Tamara S Galloway, and Jamie R Lead. Silver nanoparticles: behaviour and effects in the aquatic environment. *Environment international*, 37(2):517–531, 2011.

[29] Quang Huy Tran, Anh-Tuan Le, et al. Silver nanoparticles: synthesis, properties, toxicology, applications and perspectives. *Advances in natural sciences: nanoscience and nanotechnology*, 4(3):033001, 2013.

[30] Alexandra-Cristina Burdușel, Oana Gherasim, Alexandru Mihai Grumezescu, Laurențiu Mogoantă, Anton Ficai, and Ecaterina Andronescu. Biomedical Applications of Silver Nanoparticles: An Up-to-Date Overview. *Nanomaterials*, 8(9):681, August 2018.

[31] Jyotsna Thayath, Keechilat Pavithran, Shantikumar V Nair, and Manzoor Koyakutty. Cancer nanomedicine developed from total human serum: a novel approach for making personalized nanomedicine. *Nanomedicine*, 16(12):997–1015, 2021.

[32] F Benyettou, R Rezgui, F Ravaux, T Jaber, K Blumer, M Jouiad, L Motte, J-C Olsen, C Platas-Iglesias, M Magzoub, et al. Synthesis of silver nanoparticles for the dual delivery of doxorubicin and alendronate to cancer cells. *Journal of Materials Chemistry B*, 3(36):7237–7245, 2015.

[33] ME Barbinta-Patrascu, N Badea, C Pirvu, M Bacalum, C Ungureanu, PL Nadejde, C Ion, and I Rau. Multifunctional soft hybrid bio-platforms based on nano-silver and natural compounds. *Materials Science and Engineering: C*, 69:922–932, 2016.

[34] Bijay Kumar Poudel, Zar Chi Soe, Hima Bindu Ruttala, Biki Gupta, Thiruganesh Ramasamy, Raj Kumar Thapa, Milan Gautam, Wenquan Ou, Hanh Thuy Nguyen, Jee-Heon Jeong, et al. In situ fabrication of mesoporous silica-coated silver-gold hollow nanoshell for remotely controllable chemo-photothermal therapy via phase-change molecule as gatekeepers. *International journal of pharmaceutics*, 548(1):92–103, 2018.

[35] Mahendra Rai, Avinash P Ingle, Indarchand Gupta, and Adriano Brandelli. Bioactivity of noble metal nanoparticles decorated with biopolymers and their application in drug delivery. *International journal of pharmaceutics*, 496(2):159–172, 2015.

[36] Sumit Sarkar and Ratan Das. Shape effect on the optical properties of anisotropic silver nanocrystals. *Journal of Luminescence*, 198:464–470, 2018.

[37] Y Delgado-Beleño, CE Martinez-Nuñez, M Cortez-Valadez, NS Flores-López, and M Flores-Acosta. Optical properties of silver, silver sulfide and silver selenide nanoparticles and antibacterial applications. *Materials Research Bulletin*, 99:385–392, 2018.

[38] Manikandan Dhayalan, Priadharsini Karikalan, Mohammed Riyaz Savaas Umar, and Nalini Srinivasan. Biomedical applications of silver nanoparticles. In *Silver Micro-Nanoparticles-Properties, Synthesis, Characterization, and Applications*. IntechOpen, 2021.

[39] Paige K Brown, Ammar T Qureshi, Alyson N Moll, Daniel J Hayes, and W Todd Monroe. Silver nanoscale antisense drug delivery system for photoactivated gene silencing. *ACS nano*, 7(4):2948–2959, 2013.

[40] Sunita Patil and Rajkuberan Chandrasekaran. Biogenic nanoparticles: A comprehensive perspective in synthesis, characterization, application and its challenges. *Journal of Genetic Engineering and Biotechnology*, 18:1–23, 2020.

[41] Seerengaraj Vijayaram, Hary Razafindralambo, Yun-Zhang Sun, Seerangaraj Vasantharaj, Hamed Ghafarifarsani, Seyed Hossein Hoseinifar, and Mahdieh Raeeszadeh. Applications of green synthesized metal nanoparticles-a review. *Biological Trace Element Research*, 202(1):360–386, 2024.

[42] Her Shuang Toh, Christopher Batchelor-McAuley, Kristina Tschulik, and Richard G Compton. Chemical interactions between silver nanoparticles and thiols: a comparison of mercaptohexanol against cysteine. *Science China Chemistry*, 57:1199–1210, 2014.

[43] Bahram Bahrami-Teimoori, Yaser Nikparast, Mostafa Hojatianfar, Mahdi Akhlaghi, Reza Ghorbani, and Hamid Reza Pourianfar. Characterisation and antifungal activity of silver nanoparticles biologically synthesised by amaranthus retroflexus leaf extract. *Journal of Experimental Nanoscience*, 12(1):129–139, 2017.

[44] Sang Woo Kim, Jin Hee Jung, Kabir Lamsal, Yun Seok Kim, Ji Seon Min, and Youn Su Lee. Antifungal effects of silver nanoparticles (agnps) against various plant pathogenic fungi. *Mycobiology*, 40(1):53–58, 2012.

[45] Wafa I Abdel-Fattah and Ghareib W Ali. On the anti-cancer activities of silver nanoparticles. *J Appl Biotechnol Bioeng*, 5(1):43–46, 2018.

[46] Yan Zhou, Ying Kong, Subrata Kundu, Jeffrey D Cirillo, and Hong Liang. Antibacterial activities of gold and silver nanoparticles against escherichia coli and bacillus calmette-guérin. *Journal of nanobiotechnology*, 10:1–9, 2012.

[47] Ardhendu Kumar Mandal. Silver nanoparticles as drug delivery vehicle against infections. *Global Journal of Nanomedicine*, 3(2):1–4, 2017.

[48] Krishna Suresh Babu Naidu, Patrick Govender, and Jamila K Adam. Nano silver particles in biomedical and clinical applications. *J Pure Appl Microbiol*, 9:103–112, 2015.

[49] Lingzhou Zhao, Paul K Chu, Yumei Zhang, and Zhifen Wu. Antibacterial coatings on titanium implants. *Journal of Biomedical Materials Research Part B: Applied Biomaterials*, 91(1):470–480, 2009.

[50] Fang Li, Michael D Weir, Jihua Chen, and Hockin HK Xu. Comparison of quaternary ammonium-containing with nano-silver-containing adhesive in antibacterial properties and cytotoxicity. *Dental Materials*, 29(4):450–461, 2013.

[51] Christina Lindholm and Richard Searle. Wound management for the 21st century: combining effectiveness and efficiency. *International wound journal*, 13:5–15, 2016.

[52] Jasper S Möhler, Wilson Sim, Mark AT Blaskovich, Matthew A Cooper, and Zyta M Ziora. Silver bullets: A new lustre on an old antimicrobial agent. *Biotechnology advances*, 36(5):1391–1411, 2018.

[53] Veena Vijayakumar, Sushanta K. Samal, Smita Mohanty, and Sanjay K. Nayak. Recent advancements in biopolymer and metal nanoparticle-based materials in diabetic wound healing management. *International Journal of Biological Macromolecules*, 122:137–148, 2019.

[54] Anna Lucia Gallo, Mauro Pollini, and Federica Paladini. A combined approach for the development of novel sutures with antibacterial and regenerative properties: The role of silver and silk sericin functionalization. *Journal of Materials Science: Materials in Medicine*, 29:1–13, 2018.

[55] Amardeep Bharti, Suman Singh, Vijay Kumar Meena, and Navdeep Goyal. Structural characterization of silver-hydroxyapatite nanocomposite: a bone repair biomaterial. *Materials Today: Proceedings*, 3(6):2113–2120, 2016.

[56] Aruna Jyothi Kora and RB Sashidhar. Biogenic silver nanoparticles synthesized with rhamnogalacturonan gum: Antibacterial activity, cytotoxicity and its mode of action. *Arabian Journal of Chemistry*, 11(3):313–323, 2018.

[57] Xiao Chen and Hermann J Schluesener. Nanosilver: a nanoproduct in medical application. *Toxicology letters*, 176(1):1–12, 2008.

[58] John C Reed. Mechanisms of apoptosis. *The American journal of pathology*, 157(5):1415–1430, 2000.

[59] Xinyu Yang, Andreas P Gondikas, Stella M Marinakos, Melanie Auffan, Jie Liu, Heileen Hsu-Kim, and Joel N Meyer. Mechanism of silver nanoparticle toxicity is dependent on dissolved silver and surface coating in caenorhabditis elegans. *Environmental science & technology*, 46(2):1119–1127, 2012.

[60] Hung-Jen Yen, Shan-hui Hsu, and Ching-Lin Tsai. Cytotoxicity and immunological response of gold and silver nanoparticles of different sizes. *Small*, 5(13):1553–1561, 2009.

[61] Christina M Powers, Appala R Badireddy, Ian T Ryde, Frederic J Seidler, and Theodore A Slotkin. Silver nanoparticles compromise neurodevelopment in pc12 cells: critical contributions of silver ion, particle size, coating, and composition. *Environmental health perspectives*, 119(1):37–44, 2011.

[62] PV AshaRani, Grace Low Kah Mun, Manoor Prakash Hande, and Suresh Valiyaveettil. Cytotoxicity and genotoxicity of silver nanoparticles in human cells. *ACS nano*, 3(2):279–290, 2009.

[63] Min Jung Kim and Sehyun Shin. Toxic effects of silver nanoparticles and nanowires on erythrocyte rheology. *Food and chemical toxicology*, 67:80–86, 2014.

[64] Prashant K Jain, Xiaohua Huang, Ivan H El-Sayed, and Mostafa A El-Sayed. Review of some interesting surface plasmon resonance-enhanced properties of noble metal nanoparticles and their applications to biosystems. *Plasmonics*, 2:107–118, 2007.

[65] Chulhong Kim, Eun Chul Cho, Jingyi Chen, Kwang Hyun Song, Leslie Au, Christopher Favazza, Qiang Zhang, Claire M Cobley, Feng Gao, Younan Xia, et al. In vivo molecular

photoacoustic tomography of melanomas targeted by bioconjugated gold nanocages. *ACS nano*, 4(8):4559–4564, 2010.

[66] Giulio F Paciotti, Lonnie Myer, David Weinreich, Dan Goia, Nicolae Pavel, Richard E McLaughlin, and Lawrence Tamarkin. Colloidal gold: a novel nanoparticle vector for tumor directed drug delivery. *Drug delivery*, 11(3):169–183, 2004.

[67] University of Chicago Medicine. Theranostics, 2024. Accessed: 2024-06-28.

[68] Jesse V Jokerst, Mridhula Thangaraj, Paul J Kempen, Robert Sinclair, and Sanjiv S Gambhir. Photoacoustic imaging of mesenchymal stem cells in living mice via silica-coated gold nanorods. *ACS nano*, 6(7):5920–5930, 2012.

[69] Tohru Ishitani, Yuichi Madokoro, Mine Nakagawa, and Kaoru Ohya. Origins of material contrast in scanning ion microscope images. *Journal of electron microscopy*, 51(4):207–213, 2002.

[70] Ludwig Reimer. *Transmission electron microscopy: physics of image formation and microanalysis*, volume 36. Springer, 2013.

[71] SJ Pennycook and DE Jesson. High-resolution incoherent imaging of crystals. *Physical review letters*, 64(8):938, 1990.

[72] Joseph I Goldstein, Dale E Newbury, Joseph R Michael, Nicholas WM Ritchie, John Henry J Scott, and David C Joy. *Scanning electron microscopy and X-ray microanalysis*. springer, 2017.

[73] Debbie Stokes. *Principles and practice of variable pressure/environmental scanning electron microscopy (VP-ESEM)*. John Wiley & Sons, 2008.

[74] Carol J Cogswell and CJR2037817 Sheppard. Confocal differential interference contrast (dic) microscopy: including a theoretical analysis of conventional and confocal dic imaging. *Journal of Microscopy*, 165(1):81–101, 1992.

[75] Krisztián Koos, Begüm Peksel, and Lóránd Kelemen. Phase measurement using dic microscopy. *Acta Cybernetica*, 23(2):629–643, 2017.

[76] Farhana Kagalwala and Takeo Kanade. Reconstructing specimens using dic microscope images. *IEEE Transactions on Systems, Man, and Cybernetics, Part B (Cybernetics)*, 33(5):728–737, 2003.

[77] Samuel Hamilton, David Regan, Lukas Payne, Wolfgang Langbein, and Paola Borri. Sizing individual dielectric nanoparticles with quantitative differential interference contrast microscopy. *Analyst*, 147(8):1567–1580, 2022.

[78] Nikolaj Gadegaard. Atomic force microscopy in biology: technology and techniques. *Biotechnic & Histochemistry*, 81(2-3):87–97, 2006.

[79] Gary M McClelland, Ragnar Erlandsson, and Shirley Chiang. Atomic force microscopy: General principles and a new implementation. In *Review of progress in quantitative nondestructive evaluation*, pages 1307–1314. Springer, 1987.

[80] Pablo Cubillas and Michael W Anderson. Atomic force microscopy. *Multi Length-Scale Characterisation*, pages 121–193, 2014.

[81] Ke Wang, Kevin G Taylor, and Lin Ma. Advancing the application of atomic force microscopy (afm) to the characterization and quantification of geological material properties. *International Journal of Coal Geology*, 247:103852, 2021.

[82] Jeffrey D Clogston and Anil K Patri. Importance of physicochemical characterization prior to immunological studies. In *Handbook of Immunological properties of engineered nanomaterials*, pages 25–52. World Scientific, 2013.

[83] Peter Schuck, Huaying Zhao, Chad A Brautigam, and Rodolfo Ghirlando. *Basic principles of analytical ultracentrifugation*. CRC Press, 2016.

[84] Analytik Ltd. Particle size characterisation by dcs, Year of the content, if available.

[85] Luigi Calzolai, Douglas Gilliland, and Francois Rossi. Measuring nanoparticles size distribution in food and consumer products: a review. *Food Additives & Contaminants: Part A*, 29(8):1183–1193, 2012.

[86] Dora Mehn, Iria Maria Rio-Echevarria, Douglas Gilliland, Michael Kaiser, Klaus Vilsmeier, Peter Schuck, and Wendel Wohlleben. Identification of nanomaterials: A validation report of two laboratories using analytical ultracentrifugation with fixed and ramped speed options. *NanoImpact*, 10:87–96, 2018.

[87] Robin Capomaccio, Isaac Ojea Jimenez, Pascal Colpo, Douglas Gilliland, Giacomo Ceccone, François Rossi, and Luigi Calzolai. Determination of the structure and morphology of gold nanoparticle–hsa protein complexes. *Nanoscale*, 7(42):17653–17657, 2015.

[88] Dora Mehn, Patrizia Iavicoli, Noelia Cabaleiro, Sven Even Borgos, Fanny Caputo, Otmar Geiss, Luigi Calzolai, François Rossi, and Douglas Gilliland. Analytical ultracentrifugation for analysis of doxorubicin loaded liposomes. *International journal of pharmaceutics*, 523(1):320–326, 2017.

[89] Sabrina Gioria, Fanny Caputo, Patricia Urbán, Ciarán Manus Maguire, Susanne Bremer-Hoffmann, Adriele Prina-Mello, Luigi Calzolai, and Dora Mehn. Are existing standard methods suitable for the evaluation of nanomedicines: some case studies. *Nanomedicine*, 13(5):539–554, 2018.

[90] Fanny Varenne, Ali Makky, Mireille Gaucher-Delmas, Frédéric Violleau, and Christine Vauthier. Multimodal dispersion of nanoparticles: a comprehensive evaluation of size distribution with 9 size measurement methods. *Pharmaceutical research*, 33:1220–1234, 2016.

[91] Ciarán Manus Maguire, Matthias Rösslein, Peter Wick, and Adriele Prina-Mello. Characterisation of particles in solution–a perspective on light scattering and comparative technologies. *Science and technology of advanced materials*, 19(1):732–745, 2018.

[92] Vuk Uskoković. Dynamic light scattering based microelectrophoresis: main prospects and limitations. *Journal of dispersion science and technology*, 33(12):1762–1786, 2012.

[93] Rita Sandhu, Nishi Singh, Jyotika Dhankhar, G Kama, and Rajan Sharma. Dynamic light scattering (dls) technique, principle, theoretical considerations and applications. *Nanotechnol. Biochem. Tech. Assess. Qual. Saf. Milk Milk Prod*, pages 135–137, 2018.

[94] Jörg Stetefeld, Sean A McKenna, and Trushar R Patel. Dynamic light scattering: a practical guide and applications in biomedical sciences. *Biophysical reviews*, 8:409–427, 2016.

[95] Julian A Gallego-Urrea, Jani Tuoriniemi, and Martin Hassellöv. Applications of particle-tracking analysis to the determination of size distributions and concentrations of nanoparticles in environmental, biological and food samples. *TrAC Trends in Analytical Chemistry*, 30(3):473–483, 2011.

[96] Fanny Caputo, Jeffrey Clogston, Luigi Calzolai, M Rösslein, and Adriele Prina-Mello. Measuring particle size distribution of nanoparticle enabled medicinal products, the joint view of euncl and nci-ncl. a step by step approach combining orthogonal measurements with increasing complexity. *Journal of Controlled Release*, 299:31–43, 2019.

[97] Feiran Huang, Christopher Dempsey, Daniela Chona, and Junghae Suh. Quantitative nanoparticle tracking: applications to nanomedicine. *Nanomedicine*, 6(4):693–700, 2011.

[98] Vasco Filipe, Andrea Hawe, and Wim Jiskoot. Critical evaluation of nanoparticle tracking analysis (nta) by nanosight for the measurement of nanoparticles and protein aggregates. *Pharmaceutical research*, 27:796–810, 2010.

[99] Yiwen Pei, Robert Vogel, and Caterina Minelli. Tunable resistive pulse sensing (trps). In *Characterization of nanoparticles*, pages 117–136. Elsevier, 2020.

[100] Emma LCJ Blundell, Laura J Mayne, Emily R Billinge, and Mark Platt. Emergence of tunable resistive pulse sensing as a biosensor. *Analytical Methods*, 7(17):7055–7066, 2015.

[101] Lukas M Payne. *Optical extinction and coherent multiphoton micro-spectroscopy of single nanoparticles*. PhD thesis, Cardiff University, 2015.

[102] Mark Cronin-Golomb, Baruch Fischer, J White, and Amnon Yariv. Theory and applications of four-wave mixing in photorefractive media. *IEEE Journal of Quantum Electronics*, 20(1):12–30, 1984.

[103] Johannes Kiefer and Paul Ewart. Laser diagnostics and minor species detection in combustion using resonant four-wave mixing. *Progress in Energy and Combustion Science*, 37(5):525–564, 2011.

[104] Onur Danaci, Christian Rios, and Ryan T Glasser. All-optical mode conversion via spatially multimode four-wave mixing. *New Journal of Physics*, 18(7):073032, 2016.

[105] Florian Ströhl, Deanna L Wolfson, Ida S Opstad, Daniel H Hansen, Hong Mao, and Balpreet S Ahluwalia. Label-free superior contrast with c-band ultra-violet extinction microscopy. *Light: Science & Applications*, 12(1):56, 2023.

[106] Behnaz Ostovar, Man-Nung Su, David Renard, Benjamin D Clark, Pratiksha D Dongare, Chayan Dutta, Niklas Gross, John E Sader, Christy F Landes, Wei-Shun Chang, et al. Acoustic vibrations of al nanocrystals: size, shape, and crystallinity revealed by single-particle transient extinction spectroscopy. *The Journal of Physical Chemistry A*, 124(19):3924–3934, 2020.

[107] Lukas M. Payne, Wolfgang Langbein, and Paola Borri. Erratum: Polarization-resolved extinction and scattering cross-sections of individual gold nanoparticles measured by wide-field microscopy on a large ensemble [appl. phys. lett. 102, 131107 (2013)]. *Appl. Phys. Lett.*, 110(22):229901, 2017.

[108] Lukas M. Payne, Wolfgang Langbein, and Paola Borri. Polarization-resolved extinction and scattering cross-sections of individual gold nanoparticles measured by wide-field microscopy on a large ensemble. 102(13):131107.

[109] Lukas M. Payne, Wolfgang Langbein, and Paola Borri. Wide-field imaging of single-nanoparticle extinction with sub- nm 2 sensitivity. 9(3):034006.

[110] Olavi Siiman, Andrei Jitianu, Marjan Bele, Patricia Grom, and Egon Matijević. Amplified light scattering and emission of silver and silver core–silica shell particles. *Journal of colloid and interface science*, 309(1):8–20, 2007.

[111] Kallum M Koczkur, Stefanos Mourdikoudis, Lakshminarayana Polavarapu, and Sara E Skrabalak. Polyvinylpyrrolidone (pvp) in nanoparticle synthesis. *Dalton transactions*, 44(41):17883–17905, 2015.

[112] Elena Ureña-Horno, Maria-Eleni Kyriazi, and Antonios G Kanaras. A method for the growth of uniform silica shells on different size and morphology upconversion nanoparticles. *Nanoscale Advances*, 3(12):3522–3529, 2021.

[113] S Yanniotis, S Skaltsi, and S Karaburnioti. Effect of moisture content on the viscosity of honey at different temperatures. *Journal of Food Engineering*, 72(4):372–377, 2006.

[114] Shan Zhou, Zhenlei Liu, Zixu Wang, Cora J Young, Trevor C VandenBoer, B Beverly Guo, Jianshun Zhang, Nicola Carslaw, and Tara F Kahan. Hydrogen peroxide emission and fate indoors during non-bleach cleaning: a chamber and modeling study. *Environmental Science & Technology*, 54(24):15643–15651, 2020.

[115] Frank B Knight. *Essentials of Brownian motion and diffusion*. Number 18. American Mathematical Soc., 1981.

[116] Shingo Ishizawa. The unsteady laminar flow between two parallel discs with arbitrarily varying gap width. 9(35):533–550.

[117] Shucheng Li, Lirong Qiu, Yun Wang, Han Cui, and Weiqian Zhao. Super-resolution radially polarized pupil-filtering confocal raman spectroscopy technology. 31(3):035903.

[118] Marcus Dyba and Stefan W. Hell. Focal spots of size Î˘/23 open up far-field florescence microscopy at 33 nm axial resolution. 88(16):163901.

[119] Marinella Farre and Damia Barcelo. Introduction to the analysis and risk of nanomaterials in environmental and food samples. In *Comprehensive Analytical Chemistry*, volume 59, pages 1–32. Elsevier.

[120] William L. Barnes, Alain Dereux, and Thomas W. Ebbesen. Surface plasmon subwavelength optics. 424(6950):824–830.

[121] Alexis Loiseau, Victoire Asila, Gabriel Boitel-Aullen, Mylan Lam, Michèle Salmain, and Souhir Boujday. Silver-based plasmonic nanoparticles for and their use in biosensing. *Biosensors*, 9(2):78, 2019.

[122] Shaista Babar and J. H. Weaver. Optical constants of cu, ag, and au revisited. 54(3):477.

[123] Furqan Alabdullah, Vikramdeep Singh, Lukas Payne, David Regan, Francesco Masia, Victoria G Rocha, Wolfgang Langbein, and Paola Borri. Radially polarized light in single particle optical extinction microscopy identifies silver nanoplates. *Applied Physics Letters*, 124(18), 2024.

[124] K Lance Kelly, Eduardo Coronado, Lin Lin Zhao, and George C Schatz. The optical properties of metal nanoparticles: the influence of size, shape, and dielectric environment, 2003.

[125] Francois K Guedje, Mircea Giloan, Monica Potara, MN Hounkonnou, and Simion Astilean. Optical properties of single silver triangular nanoprism. *Physica Scripta*, 86(5):055702, 2012.

[126] Martin G Blaber, Anne-Isabelle Henry, Julia M Bingham, George C Schatz, and Richard P Van Duyne. Lspr imaging of silver triangular nanoprisms: correlating scattering with structure using electrodynamics for plasmon lifetime analysis. *The Journal of Physical Chemistry C*, 116(1):393–403, 2012.

[127] Lukas M Payne, Attilio Zilli, Yisu Wang, Wolfgang Langbein, and Paola Borri. Quantitative high-throughput optical sizing of individual colloidal nanoparticles by wide-field imaging extinction microscopy. In *Colloidal Nanoparticles for Biomedical Applications XIV*, volume 10892, pages 50–60. SPIE, 2019.

[128] Prashant K Jain, Kyeong Seok Lee, Ivan H El-Sayed, and Mostafa A El-Sayed. Calculated absorption and scattering properties of gold nanoparticles of different size, shape, and composition: applications in biological imaging and biomedicine. *The journal of physical chemistry B*, 110(14):7238–7248, 2006.

[129] Yisu Wang, Attilio Zilli, Zoltan Sztranyovszky, Wolfgang Langbein, and Paola Borri. Quantitative optical microspectroscopy, electron microscopy, and modelling of individual silver nanocubes reveal surface compositional changes at the nanoscale. *Nanoscale Advances*, 2(6):2485–2496, 2020.

[130] MD McMahon, R Lopez, HM Meyer, LC Feldman, and RF Haglund. Rapid tarnishing of silver nanoparticles in ambient laboratory air. *Applied Physics B*, 80:915–921, 2005.

[131] Jose Luis Elechiguerra, Leticia Larios-Lopez, Cui Liu, Domingo Garcia-Gutierrez, Alejandra Camacho-Bragado, and Miguel Jose Yacaman. Corrosion at the nanoscale: the case of silver nanowires and nanoparticles. *Chemistry of Materials*, 17(24):6042–6052, 2005.

[132] Wei Cao and Hani E Elsayed-Ali. Stability of ag nanoparticles fabricated by electron beam lithography. *Materials Letters*, 63(26):2263–2266, 2009.

[133] Aurélie Le Beulze, Etienne Duguet, Stéphane Mornet, Jérôme Majimel, Mona Tréguer-Delapierre, Serge Ravaine, Ileana Florea, and Ovidiu Ersen. New insights into the side-face structure, growth aspects, and reactivity of ag n nanoprisms. *Langmuir*, 30(5):1424–1434, 2014.

[134] Jean M Bennett, JL Stanford, and EJ Ashley. Optical constants of silver sulfide tarnish films. *JOSA*, 60(2):224–232, 1970.

[135] ME O'Neill. Small particles in viscous media. *Science Progress (1933-)*, pages 149–184, 1981.

[136] Alfred G Emslie, Francis T Bonner, and Leslie G Peck. Flow of a viscous liquid on a rotating disk. *Journal of Applied Physics*, 29(5):858–862, 1958.

[137] Gijsberta H Koenderink and Albert P Philipse. Rotational and translational self-diffusion in colloidal sphere suspensions and the applicability of generalized stokes- einstein relations. *Langmuir*, 16(13):5631–5638, 2000.

[138] Vanessa M French, Rose A Cooper, and Peter C Molan. The antibacterial activity of honey against coagulase-negative staphylococci. *Journal of Antimicrobial Chemotherapy*, 56(1):228–231, 2005.

[139] Eranga Roshan Balasooriya, Chanika Dilumi Jayasinghe, Uthpala Apekshani Jayawardena, Ranasinghe Weerakkodige Dulashani Ruwanthika, Rohini Mendis de Silva, Preethi Vidya Udagama, et al. Honey mediated green synthesis of nanoparticles: new era of safe nanotechnology. *Journal of Nanomaterials*, 2017, 2017.

[140] ML Khalil and Siti Amrah Sulaiman. The potential role of honey and its polyphenols in preventing heart disease: a review. *African Journal of Traditional, Complementary and Alternative Medicines*, 7(4), 2010.

[141] Ahmad Oryan, Esmat Alemzadeh, and Ali Moshiri. Biological properties and therapeutic activities of honey in wound healing: A narrative review and meta-analysis. *Journal of tissue viability*, 25(2):98–118, 2016.

[142] Lee Suan Chua, Norul-Liza Abdul-Rahaman, Mohamad Roji Sarmidi, and Ramlan Aziz. Multi-elemental composition and physical properties of honey samples from malaysia. *Food Chemistry*, 135(3):880–887, 2012.

[143] M Rahardjo, M Sihombing, and MK Anggraeni. Color development and antioxidant activity in honey caramel. In *IOP Conference Series: Earth and Environmental Science*, volume 443, page 012041. IOP Publishing, 2020.

[144] Md Khairul Islam, Tomislav Sostaric, Lee Yong Lim, Katherine Hammer, and Cornelia Locher. A comprehensive hptlc-based analysis of the impacts of temperature on the chemical properties and antioxidant activity of honey. *Molecules*, 27(23):8491, 2022.

[145] Alini Mari Kuroishi, Marise Bonifácio Queiroz, Mareci Mendes de Almeida, and Leda Battestin Quast. Avaliação da cristalização de mel utilizando parâmetros de cor e atividade de água. *Brazilian Journal of Food Technology*, 15:84–91, 2012.

[146] Denis Fitzgerald. Technical assessment of the anton paar dma5000 density meter. *H&D Fitzgerald Ltd, Saint Asaph, UK*, 2000.

[147] Torsten Machleidt, Erik Sparrer, Nataliya Dorozhovets, Eberhard Manske, Karl-Heinz Franke, and Daniel Kapusi. Navigation in a large measurement volume by using afm technology as a sensor system in the npmm navigation in einem großen messvolumen in der nanopositionier-und mess-maschine (npmm) mittels afm-technologie. *TM-Technisches Messen*, 76(5):274–277, 2009.

[148] Ádám Mechler, Judit Kopniczky, János Kokavecz, Anders Hoel, Claes-Göran Granqvist, and Peter Heszler. Anomalies in nanostructure size measurements by afm. *Physical Review B*, 72(12):125407, 2005.

[149] Francesco Bonaccorso, Mirco Zerbetto, Andrea C Ferrari, and Vincenzo Amendola. Sorting nanoparticles by centrifugal fields in clean media. *The Journal of Physical Chemistry C*, 117(25):13217–13229, 2013.

[150] Yisu Wang, Zoltan Sztranyovszky, Attilio Zilli, Wiebke Albrecht, Sara Bals, Paola Borri, and Wolfgang Langbein. Quantitatively linking morphology and optical response of individual silver nanohedra. *Nanoscale*, 14(30):11028–11037, 2022.

[151] Iestyn Pope, Hugh Tanner, Francesco Masia, Lukas Payne, Kenton Paul Arkill, Judith Mantell, Wolfgang Langbein, Paola Borri, and Paul Verkade. Correlative light-electron microscopy using small gold nanoparticles as single probes. *Light: Science & Applications*, 12(1):80, 2023.

[152] Iestyn Pope, Nuno GC Ferreira, Peter Kille, Wolfgang Langbein, and Paola Borri. Background-free four-wave mixing microscopy of small gold nanoparticles inside a multicellular organ. *Applied Physics Letters*, 122(15), 2023.

[153] George Zoriniants, Francesco Masia, Naya Giannakopoulou, Wolfgang Langbein, and Paola Borri. Background-free 3d nanometric localization and sub-nm asymmetry detection of single plasmonic nanoparticles by four-wave mixing interferometry with optical vortices. *Physical Review X*, 7(4):041022, 2017.

[154] Francesco Masia, Wolfgang Langbein, and Paola Borri. Femtosecond phase-resolved microscopy of plasmon dynamics in individual gold nanospheres. *arXiv preprint arXiv:1202.4178*, 2012.

[155] Francesco Masia, Wolfgang Langbein, and Paola Borri. Measurement of the dynamics of plasmons inside individual gold nanoparticles using a femtosecond phase-resolved microscope. *Physical Review B*, 85(23):235403, 2012.